CONSTRAINED LENS ARRAYS FOR COMMUNICATION SYSTEMS WITH POLARIZATION AND ANGLE DIVERSITY

by

DARKO RADISAV POPOVIĆ

B.S., University of Belgrade, 1995

M.S., University of Colorado, 2000

A thesis submitted to the
Faculty of the Graduate School of the
University of Colorado in partial fulfillment
of the requirements for the degree of
Doctor of Philosophy
Department of Electrical and Computer Engineering
2002

This thesis entitled:
Constrained Lens Arrays for Communication Systems
with Polarization and Angle Diversity
written by Darko Radisav Popović
has been approved for the
Department of Electrical and Computer Engineering

Zoya Popović

K. C. Gupta

Date

The final copy of this thesis has been examined by the signatories;
and we find that both the content and the form meet acceptable
presentation standards of scholarly work in the above mentioned discipline

Popović, Darko Radisav (Ph.D., Electrical Engineering)

Constrained Lens Arrays for Communication Systems with Polarization and Angle Diversity

Thesis directed by Professor Zoya Popović

Abstract.

Constrained lens arrays are a special group of multibeam antenna arrays. They can be designed with up to four degrees of freedom. A two-degree-of-freedom lens array with planar front and back faces allows for a simple, lightweight, and cost effective construction.

The emphasis of this research is to design and analyze constrained lens arrays with polarization and angle diversity and for wide scan range. Several arrays are fully characterized in terms of their radiation characteristics and polarization isolation. Simulated results are confirmed with measurements. Loss mechanisms in spatial combining networks are investigated and analyzed. Results are used in the final design leading to a significant reduction in the total loss. When the lens array and the feeds are designed as a system, losses and radiation characteristics can be optimized for a wide scan range.

Application of the constrained lens arrays in several communication systems is discussed. The lens array is used in a controlled multipath environment resulting in a significant reduction in fading at the point of reception. A full duplex Ka-band lens is used for fixed-formation satellites with amplitude controlled small-angle scanning. A system that performs optical processing of RF signals with a lens array at the RF front end is presented. To put the work in this thesis in perspective, lens arrays are compared with other multibeam systems: dielectric lenses and phased arrays.

This thesis demonstrates on several practical examples that constrained lens arrays can be efficiently used as RF front ends in various communication systems.

Dedication

This thesis is dedicated to my parents Zorka and Radisav Popović, my brother Žarko Popović, my uncle Nikola Vukčević and my wife Tatjana Popović. Their unconditional love and support give me strength and motivation in all of my endeavors.

…Prekaljena iskušenjem duša
rani t'jelo ognjem elektrizma,
a nadežda veže dušu s nebom
kako luča sa suncem kapljicu…

…Tempered in trials and suffering, the soul
feeds the body with electric fire,
through hope the soul is bonded with Heaven
as the sun's ray binds droplet with the sun…

- Petar II Petrović Njegoš

Acknowledgments

I would like to express deepest gratitude to my adviser Professor Zoya Popović for her support, encouragement, and guidance during my studies. It is her effort and dedication that allowed me to work in a state-of-the-art laboratory and to broaden my knowledge and experience by attending various scientific conferences throughout the years.

I would also like to thank the past and present members of Zoya Popović's research group. I was fortunate to meet and work with: Eric Bryerton, Pete Kirkpatrick, Slavko Djukić, Joe Tustin, Branislav Notaroš, Jim Vian, Todd Marshall, Michael Forman, Jan Peeters Weem, Manoja Weiss, Stefania Römisch, Jason Breitbarth and Naoyuki Shino. They provided me with guidance in the operation of the laboratory equipment, measurement techniques, and manufacturing and design of antennas and circuits.

The present members of the group: Joe Hagerty, Paul Smith, Srdjan Pajić, Patrick Bell, Jacques Hung Loui, Matt Osmus, Alan Brannon, Narisi Wang, Christi Walsh and Sébastien Rondineau have all made my final years of studies a wonderful experience. Their enthusiasm and intelligence are the best guarantee that the quality of work in the group and the results will be even better in the future.

I would also like to thank the committee members Professor K. C. Gupta, Professor Dana Anderson, Professor Timothy Brown, and Professor Dejan Filipović.

Special thanks go to my OSEP adviser Professor Dana Anderson for his tireless effort in developing the teaching methods that reveal the magic of photorefractive nonlinear optics in the most efficient way. I thank the members of Dana Anderson's research group Edeline Fotheringham, Valeria Damião and Leslie Czaia for their guidance and help in the optics lab.

I want to acknowledge the help of our administrative assistants Helen Frey and Rachel Tearle for making sure that that our day-to-day operations run smoothly. I thank graduate student advisers Pam Wheeler and Adam Sadoff and foreign student advisers Marjory Gooding and Tina Tan for providing me with numerous explanations on different kinds of graduate school regulations and making sure that my paperwork is always in order.

I would like to acknowledge the National Science Foundation for the financial support of this research.

Most of all, I want to thank my dear parents and my loving wife for their contributions to my success, for their love and understanding.

Contents

Tables

Figures

Chapter 1

Introduction and Background

1.1 Introduction

This thesis addresses the topic of multibeam antenna arrays. Instead of more standard corporate feed networks, each array developed in this project has a spatial feed. This enables simultaneous multiple beams with the same feed network by simply adding a low-cost feed antenna for each beam. The goal of the thesis is to enable a lower-cost architecture for multibeam arrays with added functionality, and the experimental results indicate that this goal has been achieved.

Some of the applications for multibeam antennas that can make use of the developed arrays are: satellite communications, adaptive antenna arrays, and diversity communications for improved capacity. In order to accommodate for the rapid growth in capacity of wireless communications, which has caused an increase in the use of the microwave and millimeter-wave frequency spectrum, different diversity techniques have been developed [1, 2, 3, 4]. The diversity method requires more than one transmission path between the transmitter and the receiver, carrying the same message but having independent fading statistics. Depending on the nature of the transmission path, several diversity techniques can be identified.

Space diversity uses multiple antennas at either receiving, transmitting or both sides. Antennas are spatially separated in a way which provides reception of uncorrelated signals. Proper combination of signals results in a significant reduction of fading and an increase in channel capacity.

Signals transmitted at two orthogonal polarizations have uncorrelated fading statistics, which is used in *polarization diversity* systems.

Scattered signals come at the point of reception from different directions. *Angle diversity* systems have multiple beams pointed at different angles which receive these uncorrelated signals.

Frequency diversity uses transmission at different frequencies to assure uncorrelation between the signals.

Time diversity systems transmit the same signal samples with a certain time separation.

Multibeam antennas have attracted increasing interest in wireless communication systems. Lightweight and low-cost design capable of wide scan range with good radiation properties is presented in this work. Angle diversity is already included in these types of systems. Polarization and frequency diversity can also be efficiently applied.

1.2 Constrained Lens Arrays Background

Constrained lens arrays are a special group of beam forming networks [5]. They share some similarities with dielectric lenses and reflector antennas on one hand and with antenna arrays on the other. Their function is to form beams in multiple directions which correspond to the position of the feed antennas at the focal surface. The name *constrained* comes from the fact that a wave incident on one face of the array does not necessarily obey Snell's law when passing through the lens array. It is instead *constrained* to follow the transmission line paths. Unlike dielectric lenses or reflector antennas, lens arrays do their collimation (transmission) and focusing (reception) discretely, using antenna arrays.

1.2.1 Metal Plate Lenses

The earliest example of constrained lenses is the metal plate lens which is made up of a stack of parallel-plate waveguides. Since the original motivation for designing metal plate lenses was to imitate a dielectric, they were even referred to as *metal plate dielectrics* [6]. A stack of thin metal plates spaced distance a apart has an index of refraction of [7]:

$$\eta = \sqrt{1 - \left(\frac{\lambda_0}{2a}\right)^2} \tag{1.1}$$

for a wave polarized parallel to the plates. The incident wave polarized in that direction will excite the TE_{10} mode in the waveguides. The metal plate lens and its dielectric lens counterpart are shown in Figure 1.1 The index of refraction given by Equation 1.1 is less than one, which means that the phase velocity in the waveguide is faster than that in free space. In order to design a convex lens like the one presented in Figure 1.1(b) the metal plate lens has to be thinnest in the center and to grow progressively toward the edges (Figure 1.1(b)). This lens can focus only in one plane (elevation) and requires a line source feed. The focusing in azimuthal plane can be achieved by shaping the plates in their horizontal dimension. Many variations of the metal plate lenses are possible: both faces of the lens can be curved, and the

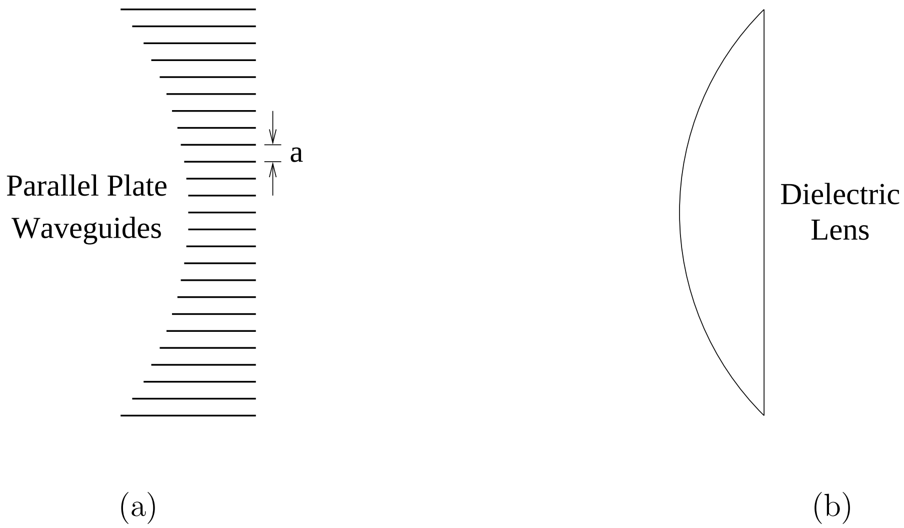

Figure 1.1: Cross-sectional views of a metal plate lens (a) and an equivalent dielectric lens (b).

height of the waveguide can vary thereby changing the index of refraction across the lens. A design called the *egg crate* lens is made up of a lattice of square, rectangular, or round waveguides. One of the advantages of the egg crate lenses over the parallel plate lenses is their ability to focus both polarizations. Disadvantages are dispersion in the waveguides which limits the bandwidth and causes chromatic aberrations, and increased weight. The latter can be reduced by *zoning* or *stepping*, i.e. cutting the thickness down whenever it exceeds one guided wavelength. However, that comes at the expense of higher sidelobes due to *shadowing* effect.

1.2.2 Bootlace Aerial

In 1957 Gent introduced the *Bootlace Aerial* [8] and made a significant step in the fundamental understanding of the constrained lens arrays. In this approach, CLAs are treated as antenna arrays, which opened up a wide range of design possibilities. Different types of low-dispersive transmission lines can be used to connect two faces of the CLA instead of waveguides. That allows for higher bandwidth and use of broadband antennas as radiating elements. Gent's Bootlace Aerial was made of folded dipole radiators connected by parallel wire cables with a ground plane between the two sides of the CLA. The length of the transmission lines is varied across the CLA. It is the longest at the center of the lens and gets progressively shorter toward the edges. This design uses only one degree of freedom, the length of the transmission lines. Gent, however suggested a general design with four degrees of freedom

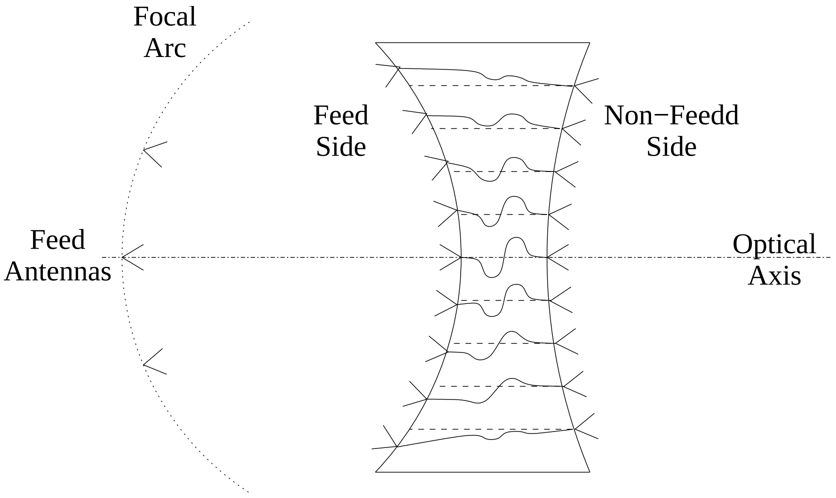

Figure 1.2: Constrained lens array with four degrees of freedom: the shape of the feed side, the shape of the non-feed side, relative position between the corresponding elements and the length of the delay lines.

(Figure 1.2):

1) the shape of the feed side (the side that is nearest to the feed)

2) the shape of the non-feed side

3) the relative position of corresponding antenna elements in the two sides of the lens array

4) the length of the transmission line which interconnects corresponding elements in the two sides of the lens array.

Several Bootlace Structures proposed by Gent, Jones, and Browne [9] are presented in Figure 1.3. A reflectarray is presented in Figure 1.3(a). This configuration has only one face and serves as a *parasitic array mirror*. Phase shifters can be used to provide collimation and beam steering as shown in Figure 1.3(b). This is known as a *space fed phased array.* Variable attenuators can be used in order to controll the aperture amplitude distribution for low sidelobes and beam shaping. Insertion of amplifiers as shown in Figure 1.3(c) results in an active amplifier array. It is a very popular configuration used in spatial power combining schemes [10, 11, 12, 13, 14]. Polarizations of the antenna elements at the feed and the non-feed side can be orthogonal resulting in a polarization isolation between the two sides of the CLA. This concept can also be used for polarization transformation. These basic configurations can be used a wide range of applications as reported in [15, 16, 17].

One of the most popular constrained lenses is a Rotman lens [18]. It has three focal points, one located at the optical axis and the other two positioned at two symmetrical points off axis. The shape of the feed side, relative position of the antenna elements and the length of the transmission lines are used as design parameters.

Three-dimensional lens arrays are used for two-axis scanning. The feeds are distributed at the *optimal focal surface* which is calculated numerically or analytically. The lens array can be designed for a maximum of four focal points or it can be symmetric in φ in which case there are no perfect focal points. Rao [19] reported a three-dimensional CLA with four focal points placed at the straight line, while Rappaport and Zaghloul [20] oriented them on a circle. In both cases all four foci are located in the same φ plane. Cornbleet [21] reported a symmetrical three-dimensional CLA in which the focal surface is φ-symetric.

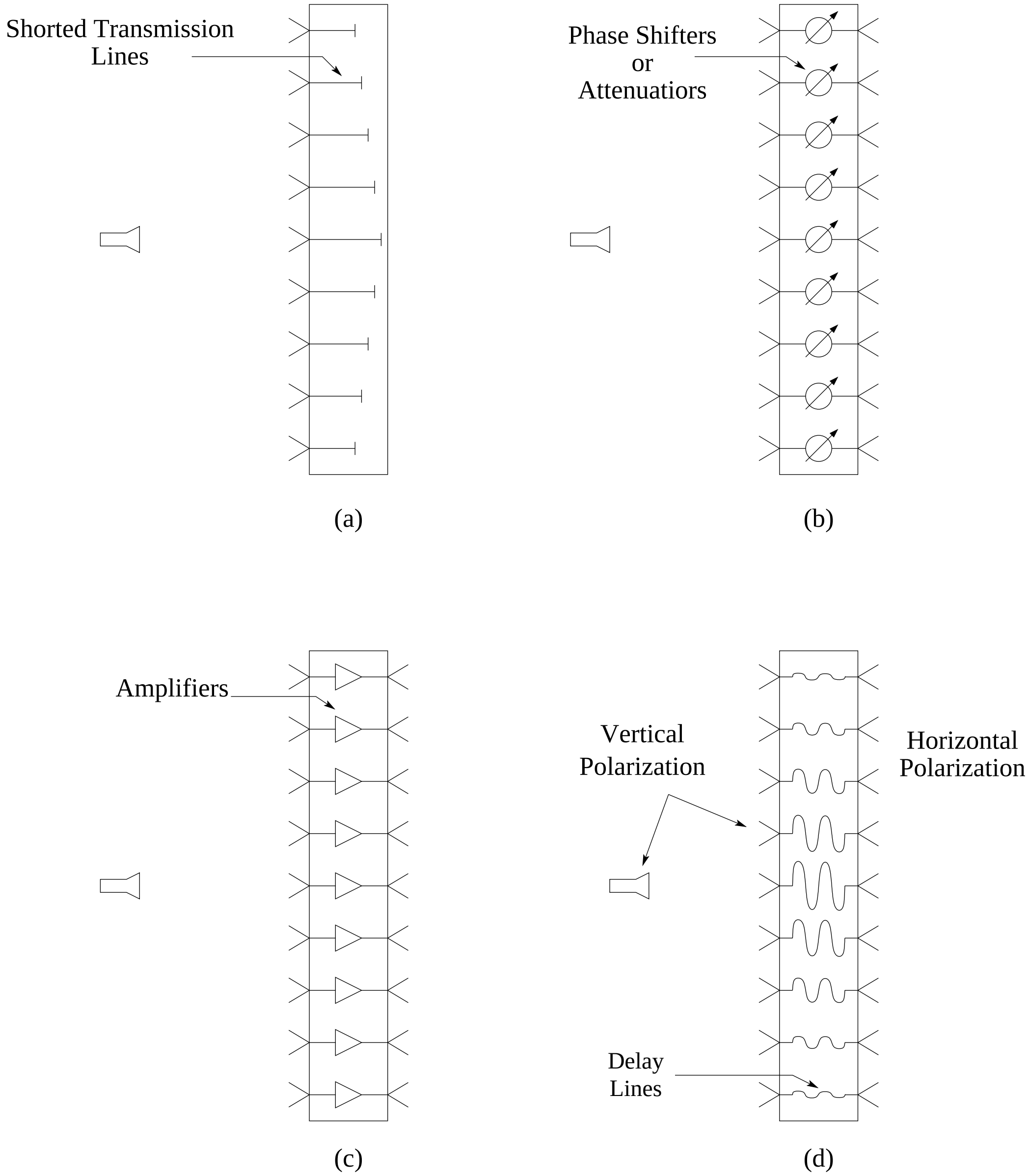

Figure 1.3: Bootlace Lenses: (a) parasitic array mirror (reflect array), (b) amplitude or phase taper lens (c) active amplifier array and (d) polarization changing aerial

1.2.3 Microstrip Constrained Lens (McGrath Lens)

A CLA with planar front and back faces, which uses only two degrees of freedom was first proposed by McGrath [22, 23, 24]. He suggested arrays of microstrip patch antennas with a common ground plane, and delay lines made with microstrip transmission lines. Connection between the elements on two sides of the array can be either a feed-through pin or a slot coupler in the ground plane. This design has one important advantage over the quadrufocal three-dimensional CLAs: due to its planar faces it is easy to manufacture and therefore less expensive and suitable for a wide range of different applications. Monolithic microwave integrated circuits (MMICs) can easily be incorporated at either one or both sides of the lens array.

The derivation of the lens design equations follows. A linear lens is considered first as shown in Figure 1.4. In order to design a lens with two focal points located at $(y, z) = (-F\,cos\,\theta_0, \pm F\,sin\,\theta_0)$, two equations have to be satisfied:

$$\sqrt{F^2 + \rho^2 - 2\,\rho\,F\,sin\,\theta_0} + W + r\,sin\,\theta_0 = F + W_0 \tag{1.2}$$

$$\sqrt{F^2 + \rho^2 + 2\,\rho\,F\,sin\,\theta_0} + W - r\,sin\,\theta_0 = F + W_0 \tag{1.3}$$

where F is the focal length, W is the electrical length of the delay lines, W_0 is an arbitrary constant, and r and ρ are the coordinates of the antenna elements at the non-feed side and the feed side of the lens array. Solving

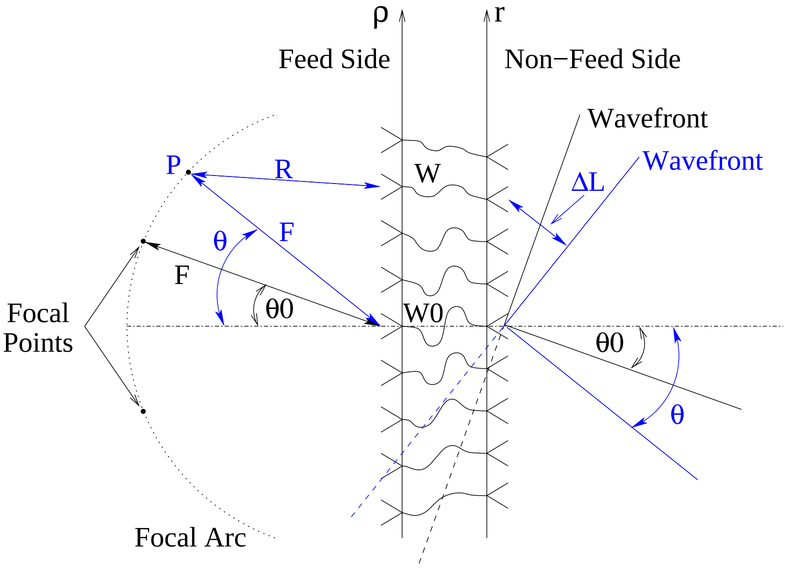

Figure 1.4: Linear constrained lens array with two degrees of freedom.

these two equations for ρ and W gives:

$$\rho = r\sqrt{\frac{F^2 - r^2\, sin^2\, \theta_0}{F^2 - r^2}} \tag{1.4}$$

$$\begin{aligned} W = F + W_0 - \frac{1}{2}&\sqrt{F^2 + \rho^2 - 2\,\rho\, F\, sin\, \theta_0} \\ -\frac{1}{2}&\sqrt{F^2 + \rho^2 + 2\,\rho\, F\, sin\, \theta_0} \end{aligned} \tag{1.5}$$

There are only two perfect focal points for which the path length error (PLE) is zero. It is important to characterize the focusing properties of the lens in the entire scan range. In order to do that the PLE has to be calculated. An arbitrary point P at the distance F from the center of the lens and at an angle θ off axis is considered (Figure 1.4). The path length calculated through an antenna element at a distance ρ will be different from the path length through the center of the lens. The PLE is given as:

$$\epsilon = R + W + \Delta\, L - F - W_0 \tag{1.6}$$

$$\epsilon = \sqrt{F^2 + \rho^2 - 2\,\rho\, F\, sin\,\theta} + W + r\, sin\,\theta - F - W_0 \tag{1.7}$$

When Equation 1.5 is substituted in Equation 1.7 it gives:

$$\begin{aligned}\epsilon = \sqrt{F^2 + \rho^2 - 2\,\rho\, F\, sin\,\theta} + r\, sin\,\theta \\ -\frac{1}{2}\sqrt{F^2 + \rho^2 - 2\,\rho\, F\, sin\,\theta_0} \\ -\frac{1}{2}\sqrt{F^2 + \rho^2 + 2\,\rho\, F\, sin\,\theta_0}\end{aligned} \tag{1.8}$$

Feed antennas can be positioned at an *optimal focal arc* $G(\theta)$ where the root mean square (rms) path length errors are minimized over the entire lens array [22]. For $\theta_0 = 0$

$$G\,(\theta) = F\,\left[1 + \frac{sin^2\,\alpha\, sin^2\,\theta}{2\,\left(1 - sec\,\alpha\right)\left(1 + sin\,\alpha\, sin\,\theta\right)}\right] \tag{1.9}$$

where $\alpha = sin^{-1}\,(r_{max}/F)$. For $\theta_0 \neq 0$ optimal focal arc is approximately given as

$$G\,(\theta, \theta_0) = sec\,\theta_0\, G\,(\theta, 0) \tag{1.10}$$

Design equations for a planar lens (also called a three-dimensional lens due to the full 3D scanning capability) are the same as those for a linear lens

(Equations 1.2 and 1.3) where r and ρ are radial instead of lateral coordinates of the non-feed side and the feed side side antenna elements (Figure 1.5). This is a symmetrical design and therefore no perfect focal points can exist.

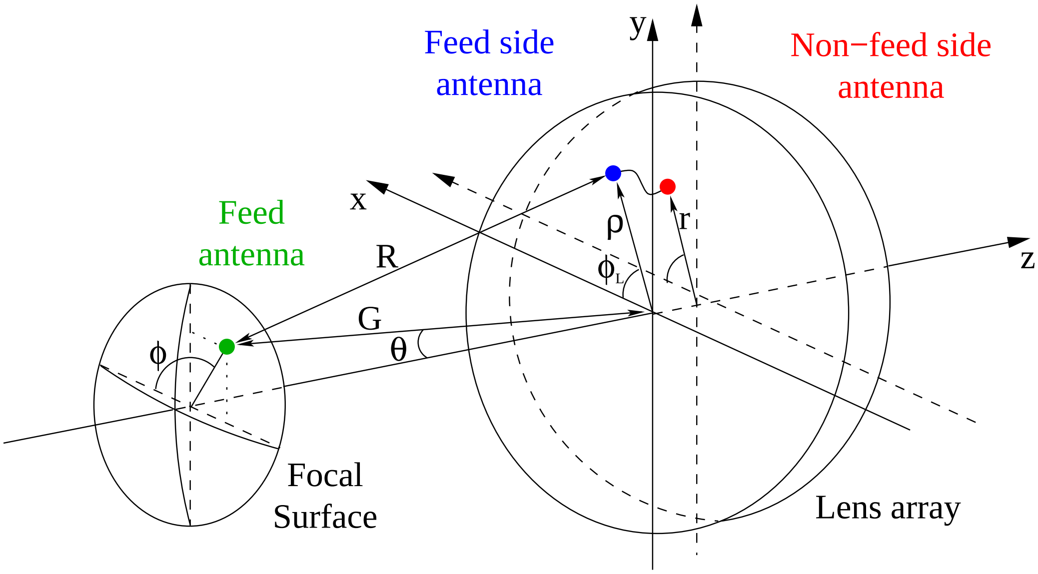

Figure 1.5: Planar constrained lens array with two degrees of freedom.

Instead there is a cone of best focus as mentioned before. A bifocal three-dimensional lens is also possible. The path length equality conditions for that case are

$$\sqrt{F^2 + \rho^2 \mp 2\,\rho\,F\,sin\,\theta_0\,cos\,\phi_l} + W \pm r\,sin\,\theta_0\,cos\,\phi_l = F + W_0 \qquad (1.11)$$

where ϕ_l is the polar coordinate of a lens array element. The design equations for the bifocal lens are

$$\rho = r\sqrt{\frac{F^2 - r^2\,sin^2\,\theta_0\,cos^2\,\phi_l}{F^2 - r^2}} \qquad (1.12)$$

$$
\begin{aligned}
W = F + W_0 - \frac{1}{2}\sqrt{F^2 + \rho^2 - 2\,\rho\,F\,sin\,\theta_0\,cos\,\phi_l} \\
-\frac{1}{2}\sqrt{F^2 + \rho^2 + 2\,\rho\,F\,sin\,\theta_0\,cos\,\phi_l}
\end{aligned}
\tag{1.13}
$$

This lens has two focal points located at $(r, \theta, \phi) = (F, \theta_0, 0^\circ); (F, \theta_0, 180^\circ)$.

Losses in the CLA can be divided in two groups. In the first group are the ones that are independent on the scan angle θ. Losses in the:

- transmission lines ε_t,
- via connections ε_v,
- feed-side antennas ε_{fs},
- non-feed side antennas ε_{nfs}, and
- and receiver (detector) antennas ε_d.

Their sum is denoted as ε_l. Since all signals on their paths from the transmitter to the receiver pass only ones through these elements ε_l is independent on the size of the lens array.

In the second group are:

- spill-over loss ε_{so},
- taper loss ε_{tl},
- scan loss ε_{sc}, and
- achievement loss ε_a.

They are functions of the scan angle θ. The spill-over loss takes into account the power radiated from the receiver antenna (also called feed or detector antenna) which is not collected by the feed-side array. Nonuniform illumination of the feed-side array results in a decrease in directivity which is accounted for in the taper loss. Projected area of the non-feed side of the lens array decreases with the increase of the scan angle resulting in the scan loss. All other losses such as cross-polarization loss and loss due to the phase errors are included in the achievement loss [25]. Unlike some reflector antennas the CLAs do not suffer from the feed blockage. The spill-over loss is the dominant loss mechanism. It increases as the ratio between the focal length F and the diameter D (F/D or $F - number$) of the lens increases. When F/D gets smaller than 0.5, taper loss becomes the dominant loss. The total loss will be minimized for F/D around 0.5. Such a small F/D will in some cases (large arrays with two-degrees of freedom) result in an extensive offset between the corresponding antenna elements close to the lens edge and the delay lines that are too long, rendering the design impractical.

1.3 Organization of the Thesis

This thesis presents design, fabrication and characterization of two constrained lens arrays, as well as application of these systems in various communication systems.

- Design and fabrication of a 45-element bifocal cylindrical lens array and its unit cell is given in Chapter 2. Theoretical and experimental characterization is presented in Chapter 3.

- Motivations for the second lens design are discussed In Chapter 4. A symmetrical 165-element element CLA is presented. Design, measurement and simulation of the unit cell and the lens array are given.

- Comparison between the CLAs and the dielectric lenses and phased arrays is discussed in Chapter 5.

- Application of the CLAs in several communication systems is presented in Chapterch 6: (1) The CLA is used for fading reduction in a multipath environment; (2) A full duplex Ka-band lens with amplitude controlled small-angle scanning is applied in fixed-formation satellites; (3) System integration with an adaptive optical processor is also presented.

- Finally, Chapter 7 gives a summary of the thesis and provides suggestions for future work on constrained lens arrays.

Chapter 2

Dual-Polarized Lens Array Design and Fabrication

2.1 Design Parameters

The lens array is designed to work in X-band with the central frequency at 10 GHz [26]. Scanning in only the horizontal plane is of interest in this project, which leads to a cylindrical lens design. Two different two-degree of freedom lens designs, as described in Chapter 1, are available: bifocal design and symmetrical design. For scanning in one dimension a bifocal design is selected. The system is designed for a wide scanning range (from -45° to $+45^\circ$). The radiation pattern degradation occurs when the beam is scanned at large angles. To partially compensate for that, two perfect focal points are set to be at $\theta_0 = \pm 45^\circ$. The lens array is designed as a dual-polarized system with two linear orthogonal polarizations.

2.2 Unit Cell Design

Several antenna types were taken into consideration as candidates for the unit cell of the dual-polarized lens array. Three of them are presented in Figure 2.1, Figure 2.2, and Figure 2.3.

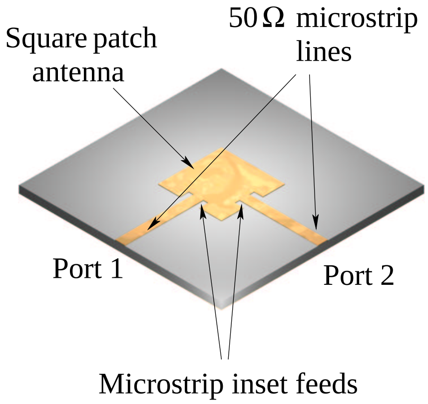

Figure 2.1: Dual-polarized square patch with microstrip edge feed with inset.

The antenna presented in Figure 2.1 uses an inset feed for the impedance match. The input resistance is multiplied by a factor of $cos^2(\pi\,\Delta\,x_i/L)$, where $\Delta\,x_i$ is the length of the inset and L is the length of the patch. The input impedance at the edge of a resonant rectangular patch ranges from $100\,\Omega$ to $400\,\Omega$ [27]. In order to lower that impedance to $50\,\Omega$, which is the

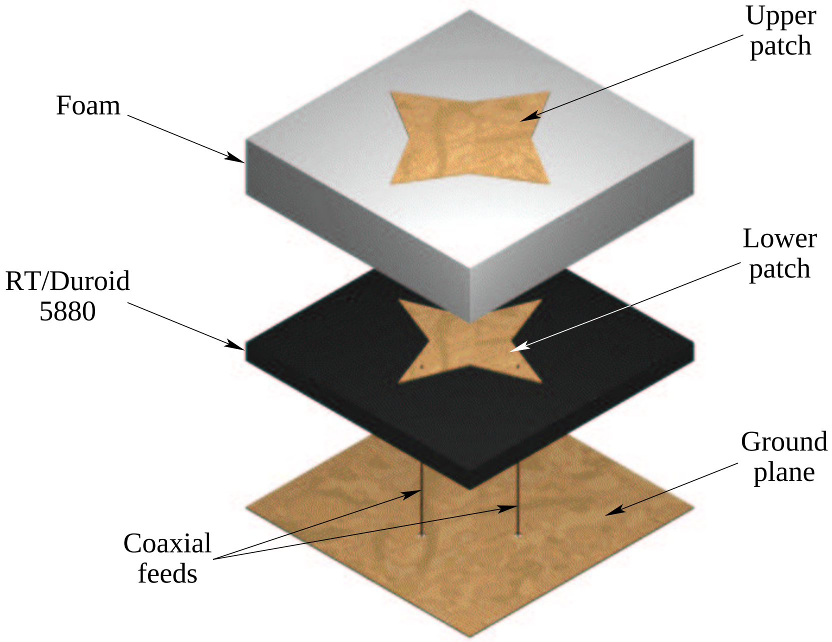

Figure 2.2: Dual-polarized star microstrip antenna.

standard impedance used by most MMIC (Microwave Monolithic Integrated Circuit) amplifiers, significant inset depths are required. This in turn degrades the cross-polarization characteristics and the radiation pattern of the antenna. The input impedance can also be controlled by changing the width of the patch antenna. However, when the dual polarization is of interest that technique is not applicable.

The star shaped antenna presented in Figure 2.2 [28] is designed using a fast MoM integral-equation solver with large-domain basis functions [29]. Results show a good performance when the coaxial probe feed is used. Additional work is needed to optimize this antenna with a microstrip feed.

A dual-polarized square patch with microstrip edge feed and quarter-wave impedance transformers is shown in Figure 2.3.

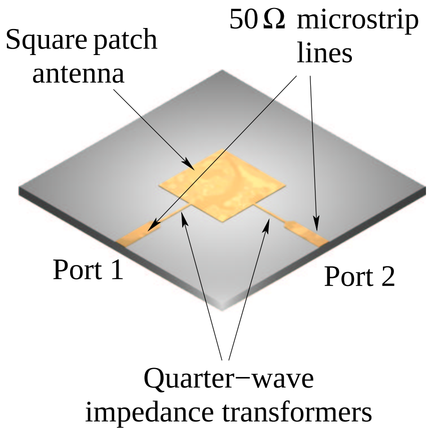

Figure 2.3: Dual-polarized square patch with microstrip edge feed and quarter-wave impedance transformers.

High impedance quarter-wave sections do not affect the cross-polarization level significantly due to their small width. That provides good polarization isolation which is required in systems with polarization diversity. Since the antenna is compact it can be efficiently used in an antenna array. An active array is also possible by insertion of MMIC amplifiers in the 50 Ω microstrip lines. This antenna configuration is selected as an element for the lens array.

The next step in the unit cell design was the selection of substrate. In this case both transmission lines and antenna are located at the same metalization level. That is beneficial in the antenna array design since everything can be printed at once, and only one layer is used. However, it has its drawbacks as well. Substrates which are optimal for the microwave circuit design are usually different from those that are preferred in the antenna design. Thin substrates with high dielectric constants are used with the transmission lines and circuitry. They minimize radiation and coupling and result in a smaller circuit size. Thick substrates with low dielectric constants used in the antenna design allow for higher directivity and larger bandwidth. This comes at the expense of the larger element size, which is undesirable in the antenna array design. If the unit cell is bigger than $\lambda_0/2$ it gives rise to grating lobes. Excitation of surface waves which propagate along the dielectric substrate is a problem that has to be addressed in antenna as well as circuit design since their effects are unwanted in most cases. Surface waves take up part of the energy, and reduce the antenna efficiency. They are especially detrimental in the antenna array design. They can diffract from substrate edges, which increases the side-lobe levels and degrades the polarization purity. The space wave efficiency which takes into account power lost in the surface waves can be defined as [30]

$$\eta = \frac{P_{sp}}{P_{sp} + P_{sw}} \tag{2.1}$$

where P_{sp} is the space wave power and P_{sw} is the surface wave power. In Figure 2.4 efficiency is calculated as a function of the normalized substrate thickness h/λ_0 for two different dielectric permittivities. Closed form expressions for the surface wave power and the space wave power presented in [30] are used in calculations. One can see that more power is lost to surface

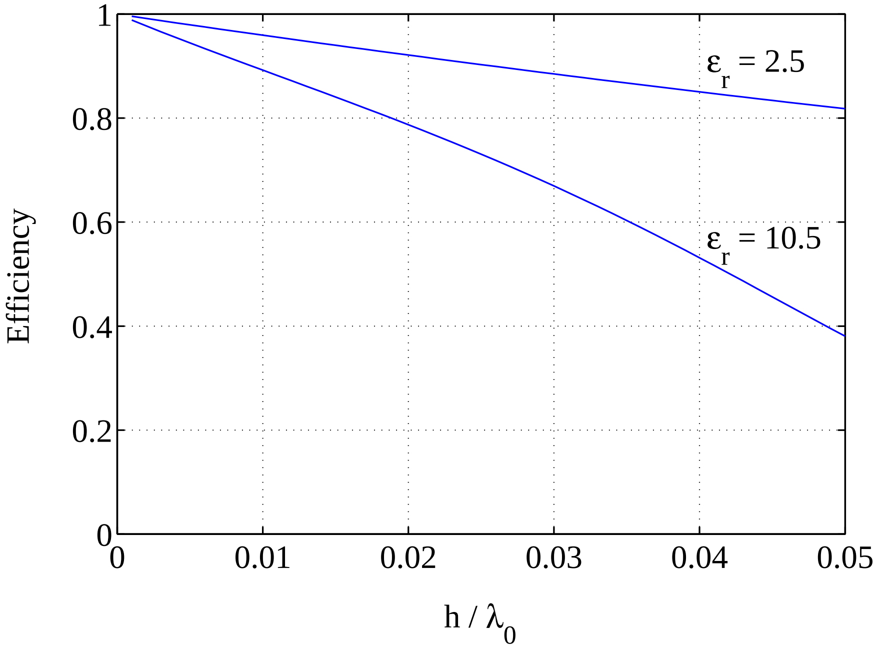

Figure 2.4: Efficiency as a function of substrate thickness, with dielectric permittivity as a parameter.

waves as the substrate thickness increases and as the permittivity increases.

The characteristic impedance of the quarter-wave sections used for the impedance matching in Figure 2.3 is given as

$$Z_{\lambda/4} = \sqrt{Z_A \, Z_0} \tag{2.2}$$

where Z_A is the input impedance at the edge of the patch antenna and Z_0 is the characteristic impedance of the new transmission line, in this case $50\,\Omega$.

The quarter-wave line is potentially a line with relatively high characteristic impedance. The width of the line as a function of the permittivity and the characteristic impedance as a parameter is given in Figure 2.5. High

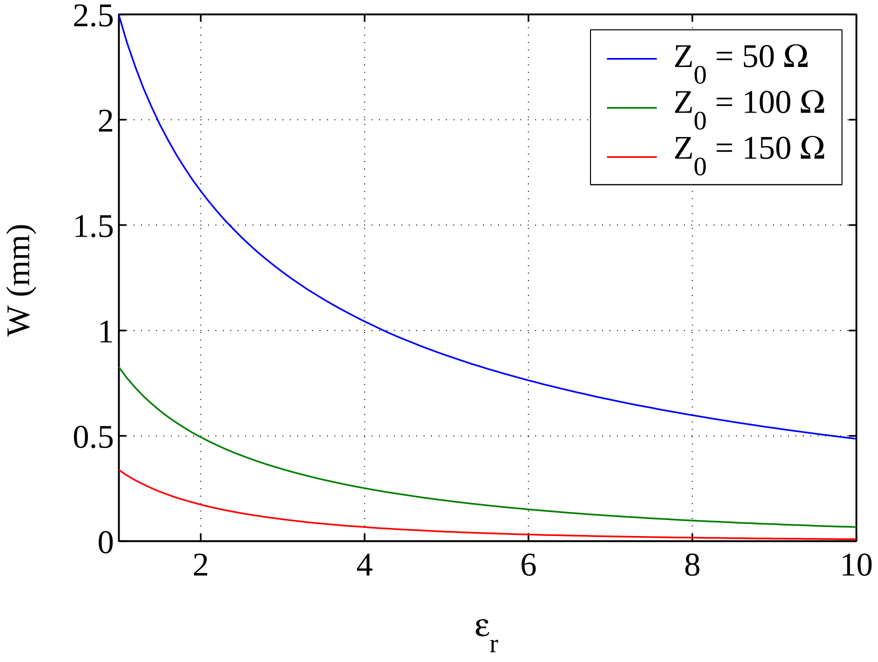

Figure 2.5: Width of the microstrip line as a function of dielectric permittivity, with the characteristic impedance as a parameter.

impedance lines on high permittivity dielectric materials could become too narrow and might be impossible to manufacture if they are smaller than 100 μm. That is another factor that determines the substrate which can be used.

Depending on the application, thermal, mechanical and other characteristics of the material, as well as the cost, can put additional constrains on the substrate choice. It should be obvious now that the selection of the material is one of the crucial steps in the antenna design. It is a trade-off between the many different parameters mentioned above. For this particular design ULTRALAM 2000 was selected. This substrate has a permittivity of 2.5, the thickness is 0.508 mm, and the loss tangent is 0.0019. ULTRALAM 2000 is a woven glass reinforced PTFE microwave laminate. Glass reinforcing fibers are oriented in the X/Y (horizontal) plane of the laminate, which maximizes dimensional stability and minimizes etch shrinkage. Another benefit in using this material is its relatively low cost.

The schematic of a dual-polarized patch antenna designed to be resonant at 10 GHz is presented in Figure 2.6. It is a square patch 9.1 mm on a side. The feed points are matched to 50 Ω feed lines with quarter wave 112 Ω matching sections. The width of the 50 Ω transmission line is 1.4 mm and the width of the 112 Ω transmission line is 0.26 mm.

2.3 Lens Array Design

The lens array designed for this study is a cylindrical 45-element array with three 15-element rows, which serve to provide a fan-shaped beam in the vertical direction. The photograph of one side of the lens, Figure 2.7(a), shows the patch antenna elements with dual-polarization feed lines and the microstrip delay lines connected with via holes to orthogonally polarized patches on the other side of the two-layer lens array. Orthogonal polarization between the

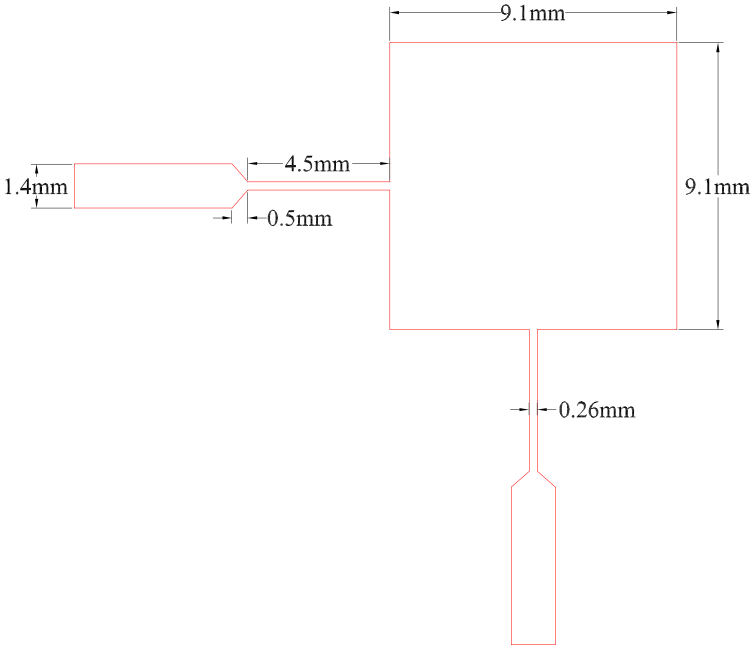

Figure 2.6: Schematic of a dual-polarized square patch with microstrip edge feed and quarter-wave impedance transformers. The antenna is a 9.1 mm square, and the feed points are matched to 50 Ω feed lines with quarter wave 112 Ω matching sections. The substrate has a relative permittivity of 2.5 and is 0.508 mm thick.

non-feed and feed sides of the lens improves the isolation between the two sides of the lens. Figure 2.7(b) shows the antennas and the transmission lines at the the non-feed side (red) and the feed side (green) of the lens array. One should notice the offset between the corresponding antenna elements, which increases as the unit cell distance from the center of the lens increases.

A single element of the lens is schematically shown in Figure 2.8. It consists of a pair of dual-polarized patch antennas printed on two microstrip

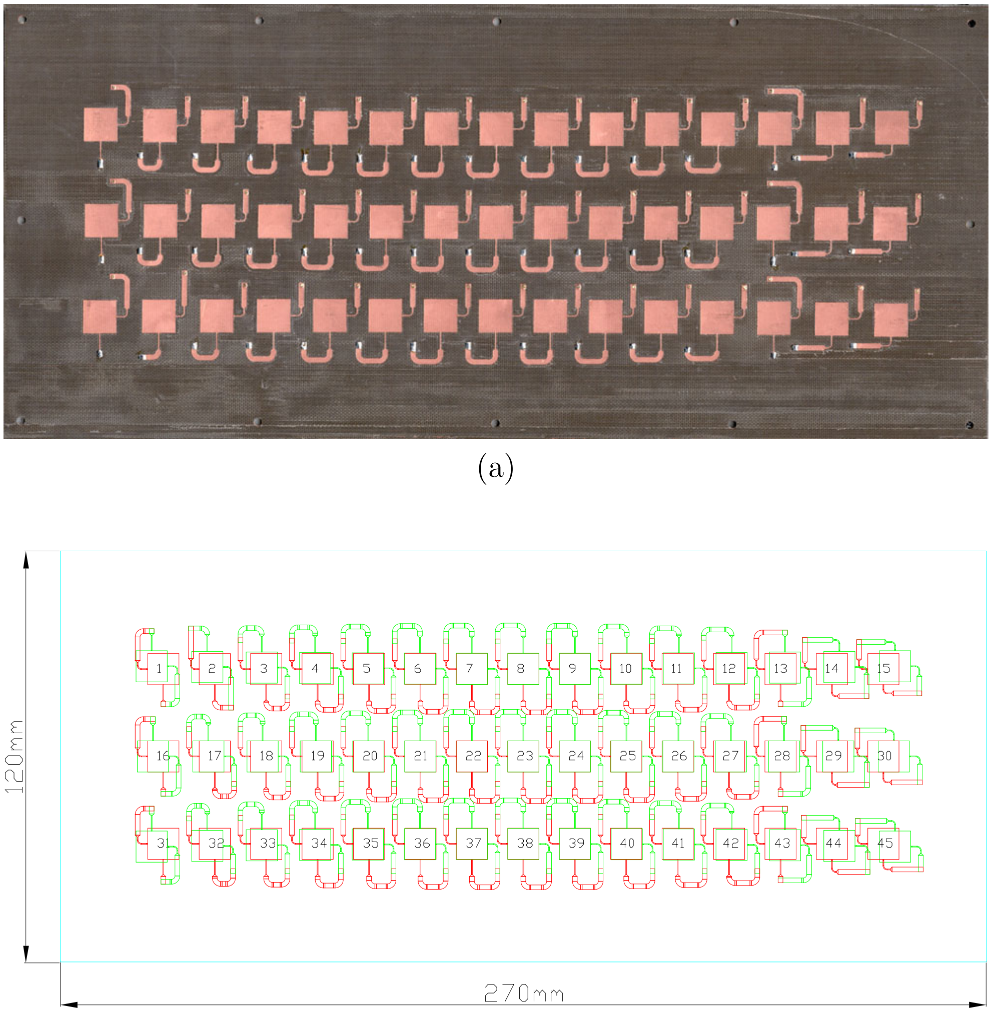

(a)

(b)

Figure 2.7: Photograph of one side of a 45-element, 10-GHz cylindrical lens antenna array (a) and the outline showing the dual-polarized patch antennas on the feed side (green lines) connected with via holes to orthogonally polarized patches on the non-feed side (red lines) (b).

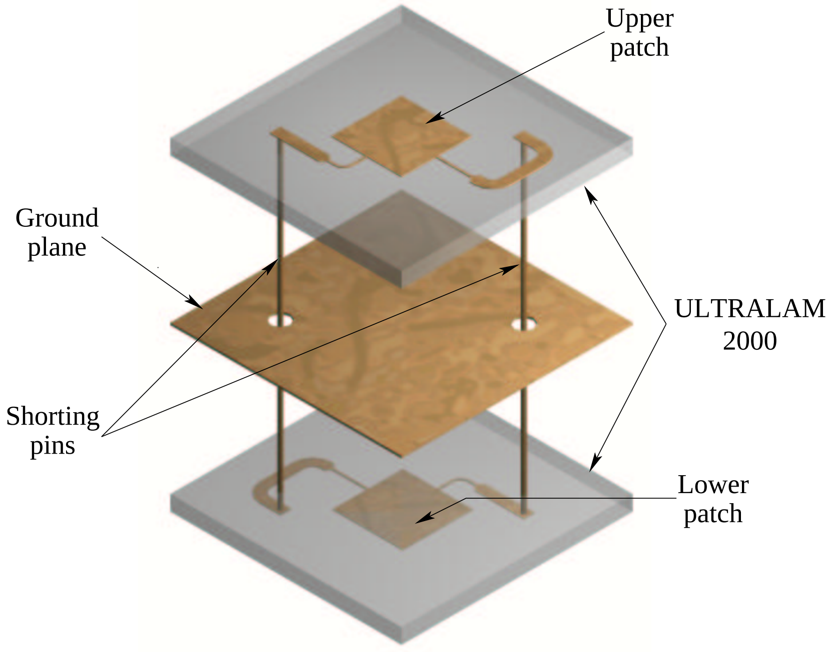

Figure 2.8: A single element of the lens consists of a pair of dual-polarized patch antennas printed on two microstrip substrates with a common ground plane. The substrates have a relative permittivity of 2.5 and are 0.508 mm thick. Each feed line is connected with a via to the corresponding orthogonally polarized feed line of the patch on the other side of the ground plane.

substrates with a common ground plane. Each feed line is connected with a via to the corresponding orthogonally polarized feed line of the patch on the other side of the ground plane. The vias are metal posts 0.8 mm in diameter. The element spacing in the array from Figure 2.7 is half of a free space wavelength in the horizontal plane and $0.85\,\lambda$ in the vertical plane. The delay lines and the positions of the antenna elements at the feed side with respect to the ones at the non-feed side are used as the design variables.

They are calculated to give two perfect focal points located at the angles $\theta_0 = \pm 45^\circ$.

The right-angle bends were used in the true time delay lines to allow for routing in the limited space determined by the unit cell size. Every effort was taken to keep the same number of discontinuities per antenna pair. That would, in turn, minimize the effect of the discontinuities on the relative phase difference between the unit cells. However, it was not possible to accomplish this for the unit cells very far from the center of the lens. In order to compensate for the effects of the transmission line bends, they were simulated using Zeland's IE3D Method of Moments software [31], and their electrical length was obtained. The results were incorporated in the final delay line design.

Since perfect focusing exists only for plane waves incident at $+45^\circ$ and -45°, other angles of incidence have path-length errors, which lead to degradation of the radiation pattern. As described in Chapter 1, these errors can be significantly reduced by refocusing. Therefore, the feeds are not positioned at the focal arc with a constant radius equal to the focal distance, but rather at the optimum focal arc which minimizes the path length errors. The difference in length between the longest and shortest delay lines is $0.35\,\lambda_0$, the focal distance-to-diameter ratio is F/D=1.5, with F=324 mm.

The lens array was built using an LPKF Protomat 93s milling machine. The resolution is $5\,\mu$m, the minimum track and gap size is 0.1 mm, and the minimum hole size is 0.2 mm. The lens array was built in three steps. In the first step, the two antenna arrays (the non-feed side and the feed side array) were milled out. On the ground planes, circular clearances for the vias were also milled out to avoid contact between the vias and the ground plane. In the second step the two arrays were connected back-to-back and glued with silver epoxy adhesive. Finally, the metal cylindrical posts were inserted and soldered to the transmission lines, connecting the antenna elements on two sides of the lens array.

Chapter 3

Dual-Polarized Lens Array Measurement and Analysis

3.1 Unit Cell Measurement and Analysis

In this section the full characterization of the isolated unit cell used in the dual-polarized lens array design is presented. Section 3.1.1 presents measured and simulated scattering parameters. Radiation patterns are given in Section 3.1.2, and the polarization characteristics in Section 3.1.3.

3.1.1 Scattering Parameters

The 2-port S-parameters of the single element of the array are measured using an HP8510 Network Analyzer with a 3.5 mm coaxial calibration and are compared to simulations obtained using Zeland's IE3D Method of Moments software, as shown in Figure 3.1(a) and Figure 3.1(b)

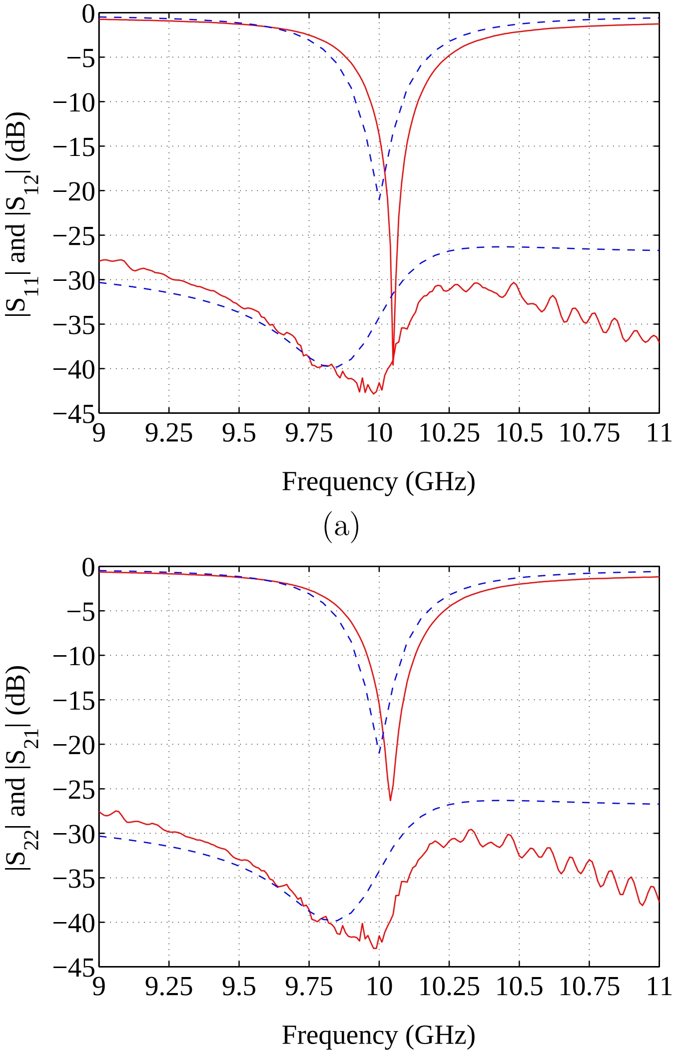

(a)

(b)

Figure 3.1: Measured (red solid lines) and simulated (blue dashed lines) two-port unit cell *s*-parameters, where the ports correspond to orthogonally polarized feeds.

From these measurements it can be seen that the isolation between the two ports of the patch is about 35 dB at resonance. Depending on the mesh size used in the simulations the results can vary. That is one of the reasons for the difference between the simulated and measured results. Another reason is the limited accuracy in the manufacturing process.

3.1.2 Radiation Patterns

The measured E- and H-plane radiation patterns of the single element in both polarizations are shown in Figure 3.2(a) and Figure 3.2(b).

The asymmetry in the radiation patterns is clearly seen to be due to the feed lines, as the patterns from one feed are almost the same as those for the other, but flipped by 180°.

3.1.3 Polarization Characterization

A standard gain horn antenna used as a transmitter was rotated around the horizontal axis from 0° to 360° and the power of the signals received at both ports of the antenna element were monitored simultaneously. The cross-pol at the two ports is about 30 dB as shown in Figure 3.3, and the two feeds are seen to be in perfect quadrature, i.e. the peak of one polarization coincides with the null of the other.

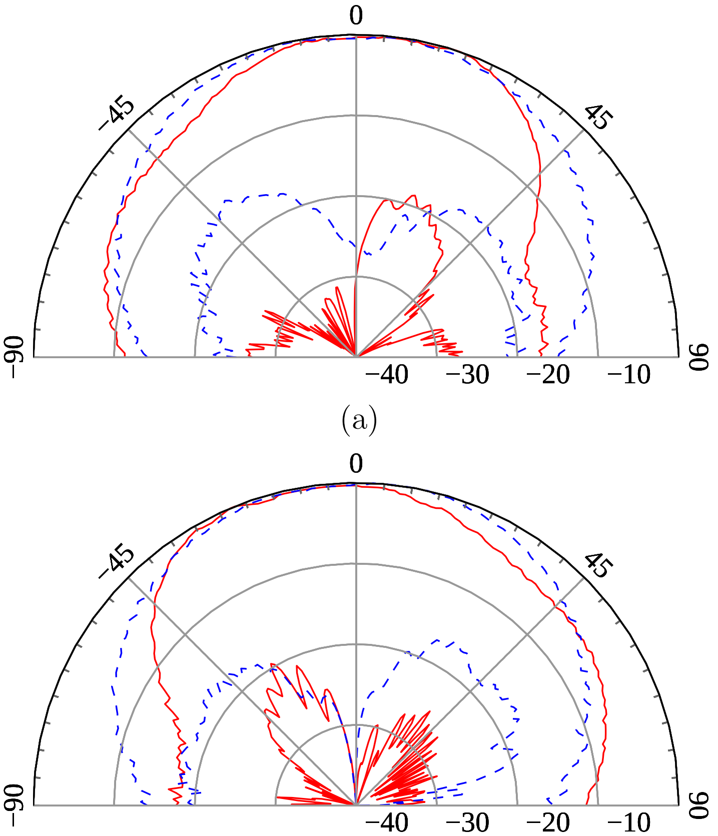

(a)

(b)

Figure 3.2: Measured element E-plane (red solid lines) and H-plane (blue dashed lines) co-polarized and cross-polarized radiation patterns for the two orthogonally polarized ports.

3.2 Lens Array Measurement and Simulation

The following work contains the detailed characterization of the dual-polarized lens array. Section 3.2.1 contains the radiation pattern measurements. Amplitude and phase excitations of the lens array antenna elements and the

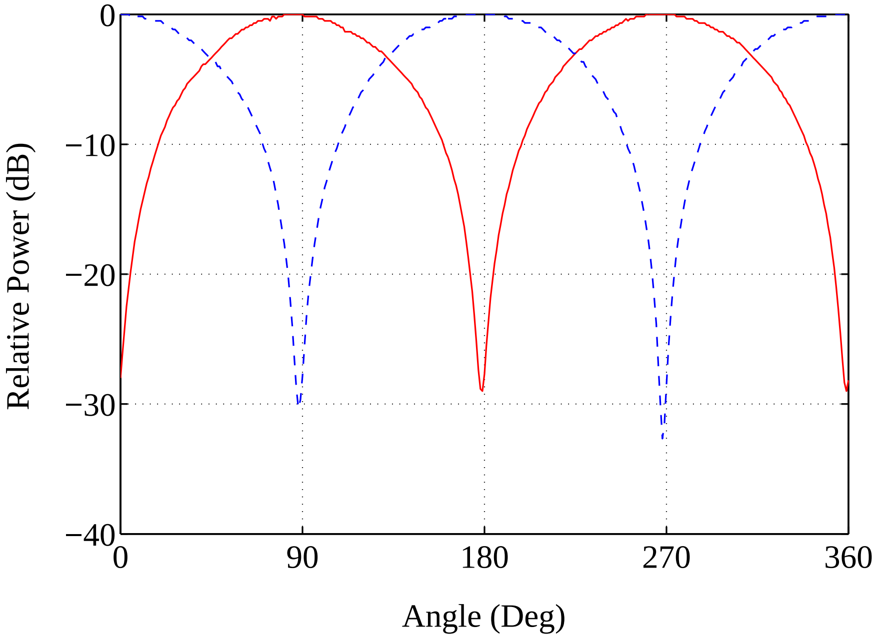

Figure 3.3: Measured axial ratio of array element for the two orthogonally polarized feeds. The solid and dashed lines are the measured relative powers at the two ports of the element as the transmitting horn polarization is rotated.

effects on the radiation pattern are discussed in Section 3.2.2. Section 3.2.3 contains a polarization characterization. The loss budget analysis is given in Section 3.2.5. Calculations of the images at the focal surface are presented in Section 3.2.6.

3.2.1 Radiation Pattern

The lens was characterized in an anechoic chamber using the setup shown in Figure 3.4. A standard gain horn antenna is co-polarized with the non-feed

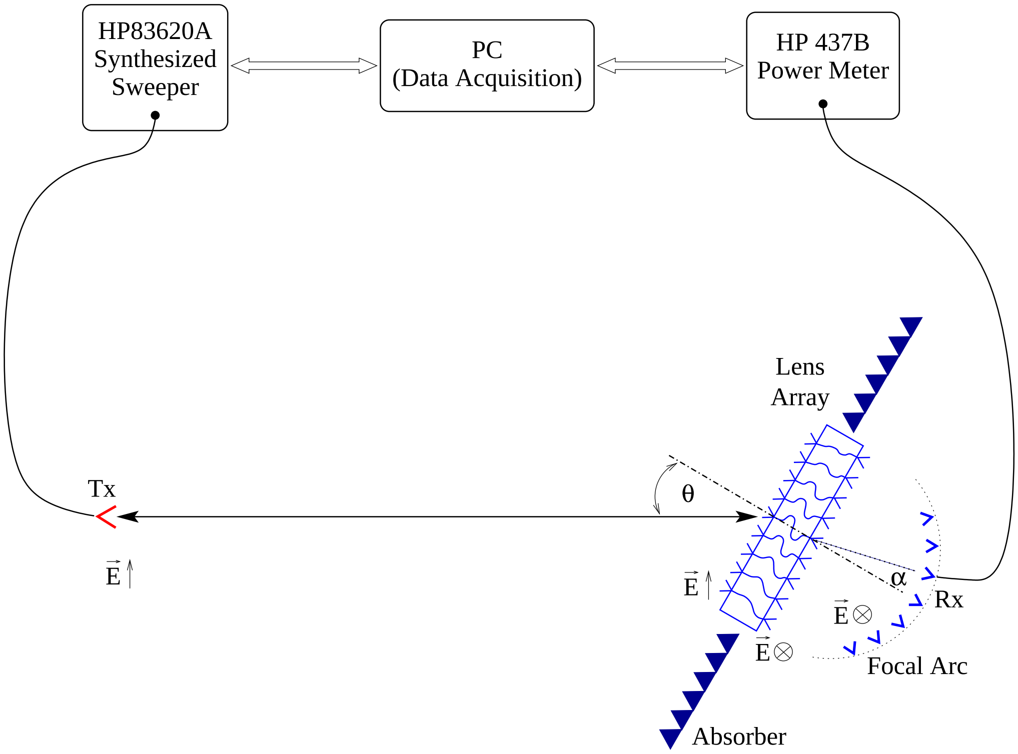

Figure 3.4: Sketch of measurement setup used to characterize the lens array. A standard-gain, linearly polarized far-field horn antenna is used as a transmitter and another horn antenna is used at the receive port.

side of the lens array and used as a transmitter in the measurements. For measuring radiation patterns corresponding to different beams of the multibeam lens, the lens is rotated and power detected at one receiver at a time. Linearly polarized horn antennas are used as the receiver antennas, but the same patches as the array elements can be used alternatively. The resulting normalized radiation patterns for receivers positioned between -45° and

+ 45° along the focal arc are shown in Figure 3.5. As the scan angle

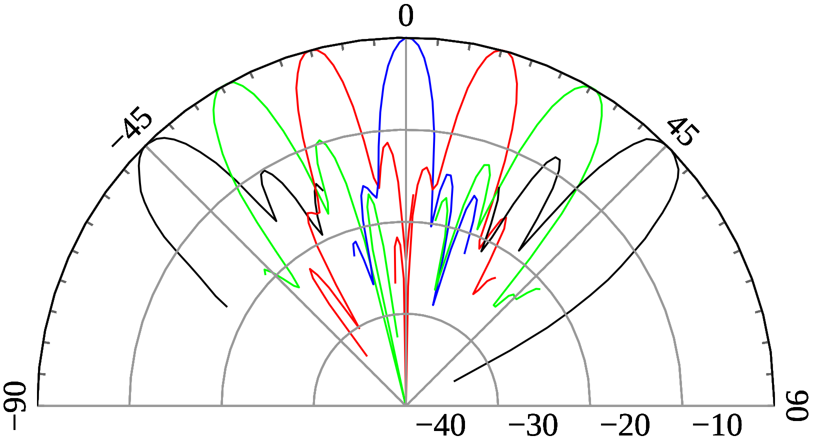

Figure 3.5: Measured normalized multibeam patterns for receivers (or transmitters) positioned at points along the optimal focal arc corresponding to beams at −45°, −30°, −15°, 0°, 15°, 30°, 45°.

increases, the beam widens and the first sidelobe increases. The measured (solid line) and simulated (dashed line) half-power beamwidths of the main lobes are presented in Figure 3.6. The maximum received power for each of the patterns in Figure 3.5 varies by about 1.5 dB in the range of scan angles and is plotted in Figure 3.7. The asymmetry in the maximum received power behavior is due to the asymmetry in the radiation pattern of the patch element as seen from Figure 3.2. In this range of scan angles, the first sidelobe level varies from -15 dB at 0° to -9 dB at 45° as shown in Figure 3.8. Simulated three-dimensional radiation pattern for the beam at boresite is given in Figure 3.9. The lens array has only three elements in the vertical plane resulting in a half-power beamwidth of around 21°.

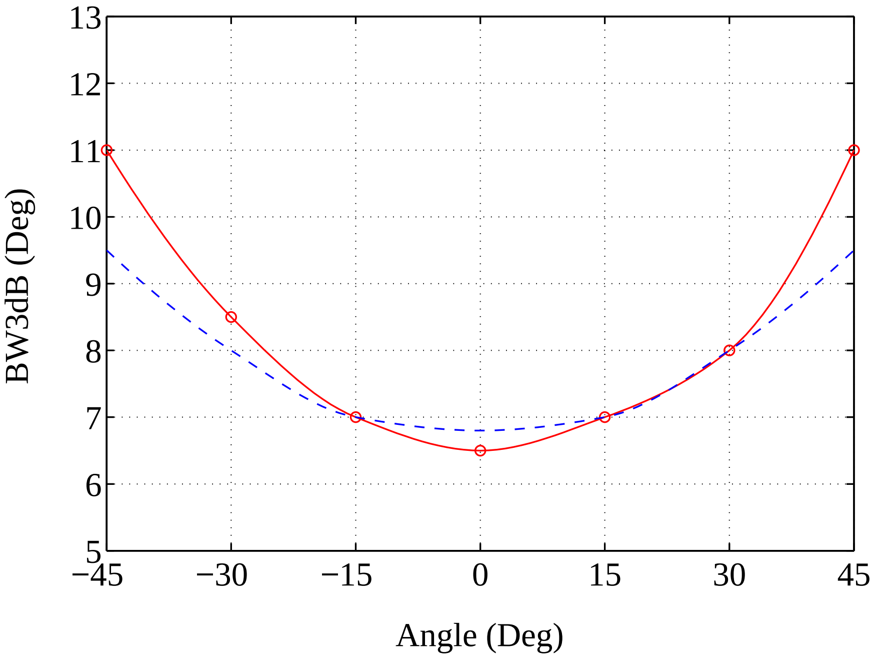

Figure 3.6: Measured (red solid line) and simulated (blue dashed line) half power beamwidth as the receiver is moved along the optimal focal arc.

3.2.2 Amplitude and Phase Excitation

Two parameters that affect the shape of the lens far-field pattern are the path-length error for feed positions that are not at the perfect focal points, and the amplitude distribution across the feed-side elements due to the spatial feed (this is easy to understand in transmission mode). Calculated lens array path length errors and amplitude distributions for a beam at boresite is presented in Figure 3.10(a) and Figure 3.10(b). The corresponding radiation pattern is presented in Figure 3.11.

Dashed lines present the case when the amplitude distribution is uniform

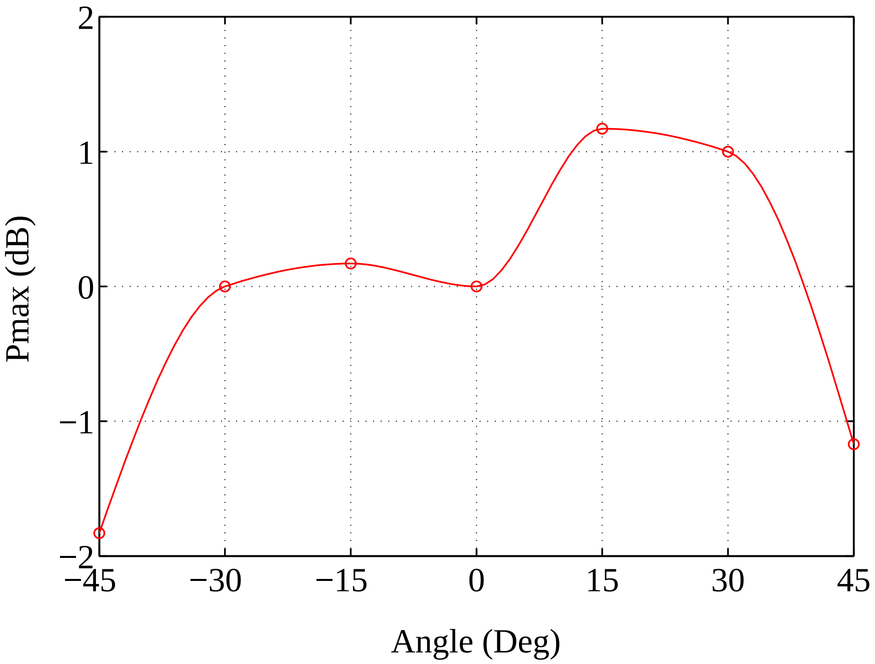

Figure 3.7: Measured maximum received power as the receiver is moved along the optimal focal arc.

and the receiving antennas are positioned at a distance F from the center of the lens array. Solid lines present the actual case with the nonuniform amplitude distribution and with the receiving antennas positioned along the optimal focal arc. The amplitude distributions and the path length errors are calculated for the 15 antenna elements in the middle row of the antenna array. The x-axis in these graphs is the position of the antenna elements along the row with the origin located at the center of the lens array. The same calculation is performed for the beam steered to -45° with the results given in Figure 3.12 and Figure 3.13, respectively.

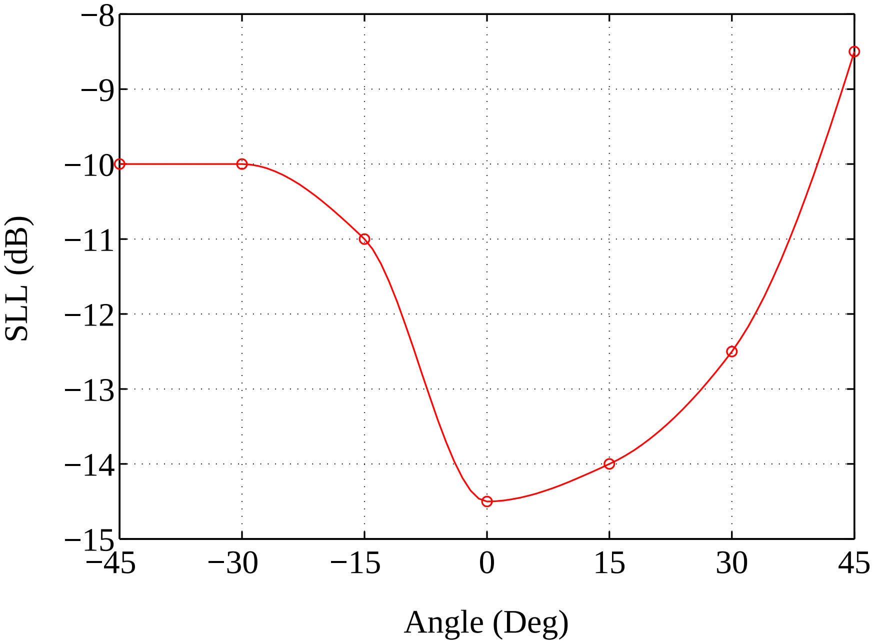

Figure 3.8: Measured side lobe level as the receiver is moved along the optimal focal arc.

An improvement of more then 5 dB in the first sidelobe level is achieved by refocusing for the beam at boresite, as shown in Figure 3.11. For the beam steered to −45 °, non-optimal amplitude distribution contributes to an increase in the first sidelobe level. The agreement between calculated and measured radiation patterns is shown in Figure 3.14 for a beam steered to −45 °. For other scan angles, the agreement between calculated and measured radiation patterns is either better or comparable to the case presented in Figure 3.14.

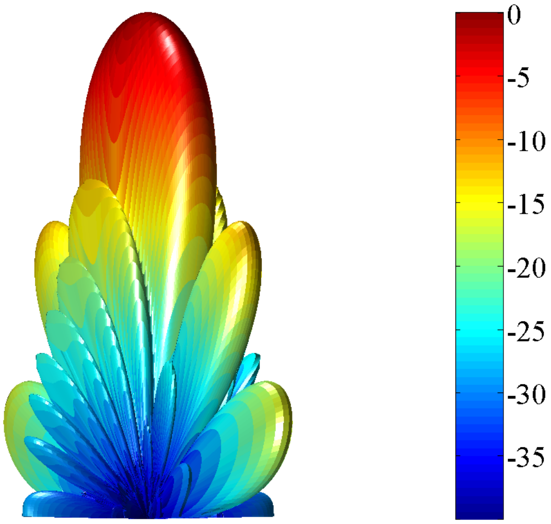

Figure 3.9: Simulated 3D radiation pattern for the lens array.

3.2.3 Polarization Characterization

The cross-pol measurement was done at 10 GHz as a function of scan angle, and the results are shown in Figure 3.15 for four different scan angles. In this measurement dual-polarized patch antennas, like the ones in Figure 2.6, are used at the receive port and both polarizations are measured simultaneously. The axial ratio degrades with increased scan angle and the two polarizations become more coupled, which can be noticed not only in the level of the cross polarized signal, but also in the relative position of the nulls and peaks for the two polarization states. As the scan angle is increased, the beamwidth broadens, the sidelobe level increases, and the polarization isolation degrades.

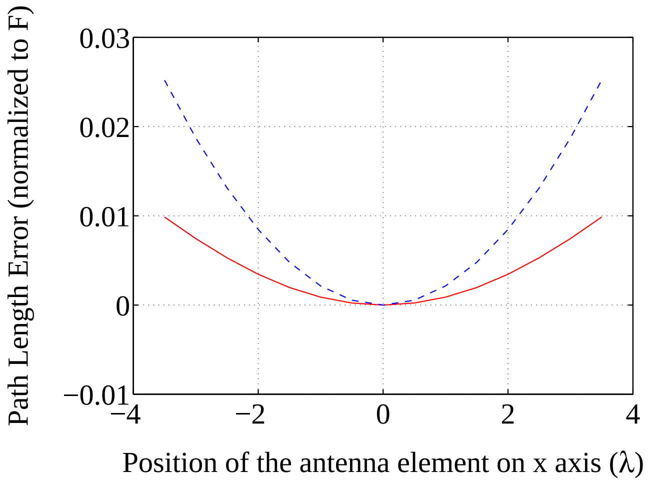

(a)

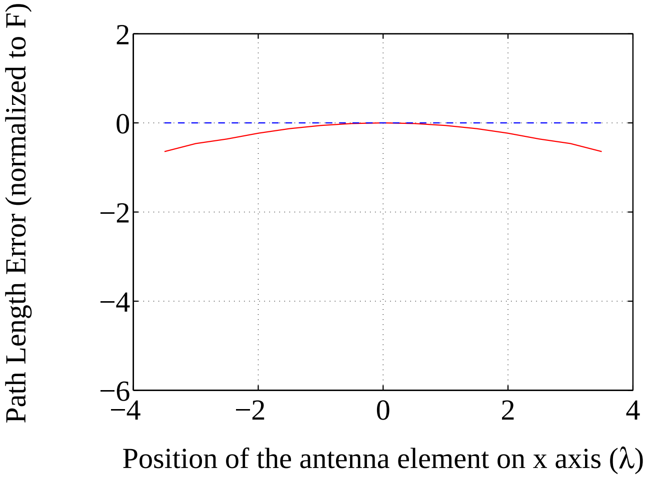

(b)

Figure 3.10: Calculated path length errors (a) and amplitude distribution (b) along the middle row of the lens array for a beam at boresite. Red solid lines represent the case with the actual amplitude distribution and the receiving antenna at the optimal focal arc. Blue dashed lines represent the case for uniform amplitude distribution and the receiving antenna at a distance F from the lens array.

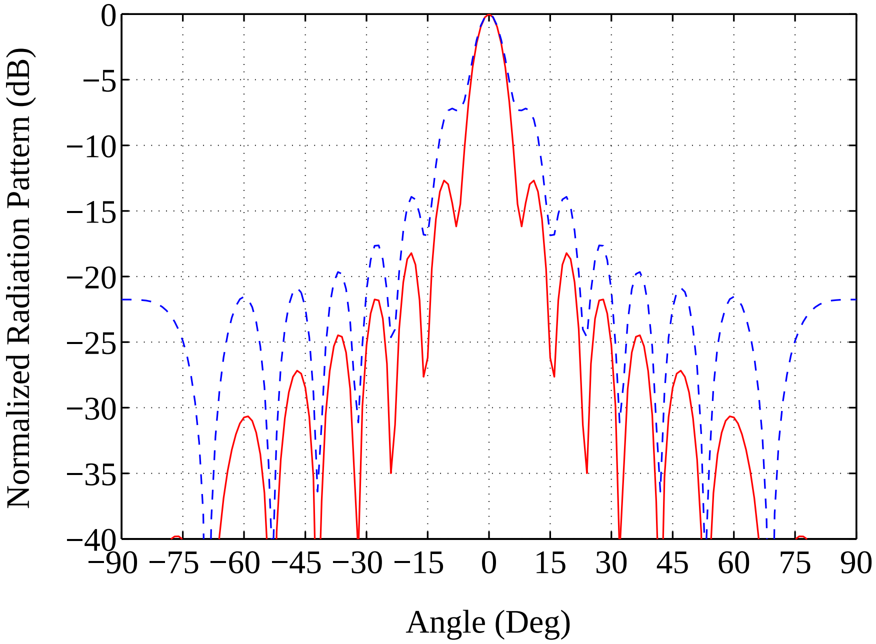

Figure 3.11: Calculated lens array radiation patterns for a beam at boresite. Red solid line shows the result for the feed at the optimal focal arc G and non-uniform amplitude distribution. Blue dashed line is for the feed at a distance F and uniform amplitude distribution.

Because of these trends for higher angles, the lens is optimized for the two beams at 45° and -45°, not the beam on boresite (0°).

3.2.4 *Thru* Measurement

Since the lens is intended to be the receiving antenna, it is important to minimize the loss in the antennas, feed lines, and spatial feed, as any loss before the LNAs has a detrimental effect on the noise figure. In order to obtain an indication of lens efficiency, *thru* measurements are performed in a 4-m

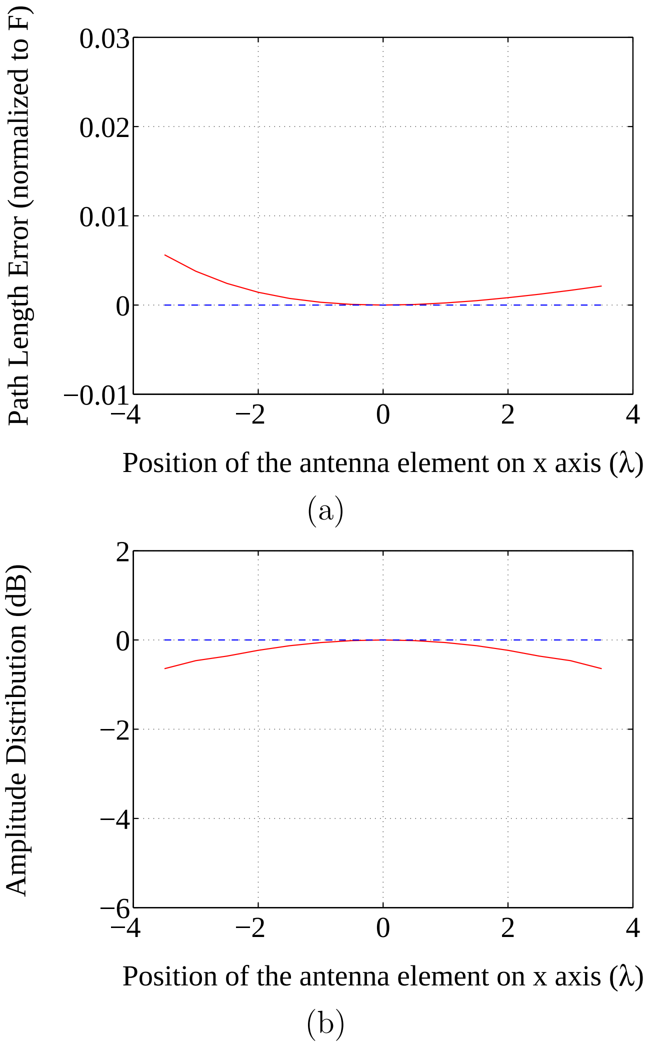

(a)

(b)

Figure 3.12: Calculated path length errors (a) and amplitude distribution (b) along the middle row of the lens array for a beam steered to -45°. Red solid lines represent the case with the actual amplitude distribution and the receiving antenna at the optimal focal arc. Blue dashed lines represent the case for uniform amplitude distribution and the receiving antenna at a distance F from the lens array.

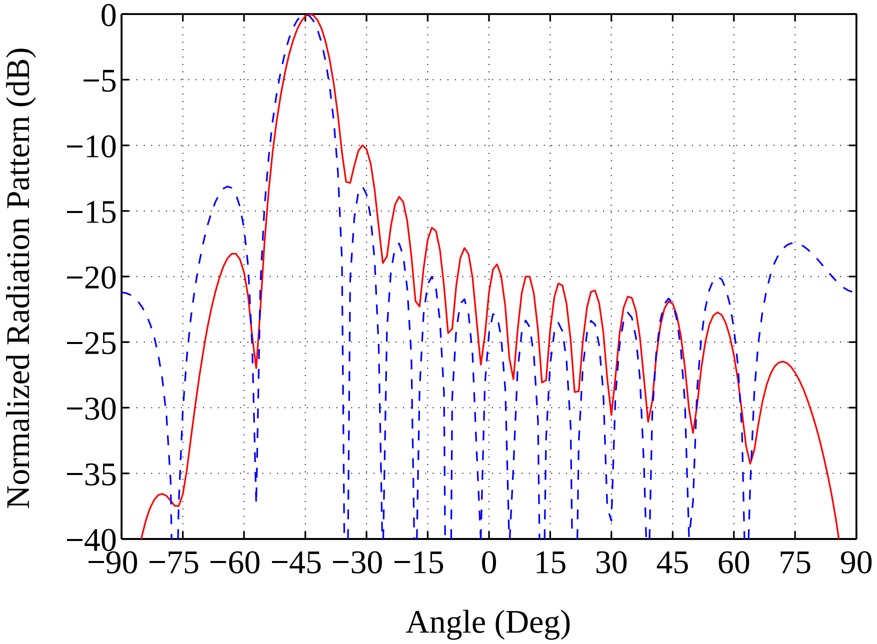

Figure 3.13: Calculated lens array radiation patterns for a beam steered to $-45°$. Red solid line shows the result for the feed at the optimal focal arc G and non-uniform amplitude distribution. Blue dashed line is for the feed at a distance F and uniform amplitude distribution.

long anechoic chamber. The transmitting and the receiving horn antennas are connected to a synthesized sweeper and power meter, respectively. The reference (0 dB) level is determined by copolarizing the antennas and measuring the line of sight received power level for a given transmitted power (Figure 3.16(a)).

The lens array is then inserted in front of the receiving horn antenna (Figure 3.16(b)). As mentioned before, the lens array has built-in polarization isolation and therefore the receiving horn antenna has to be rotated by 90°.

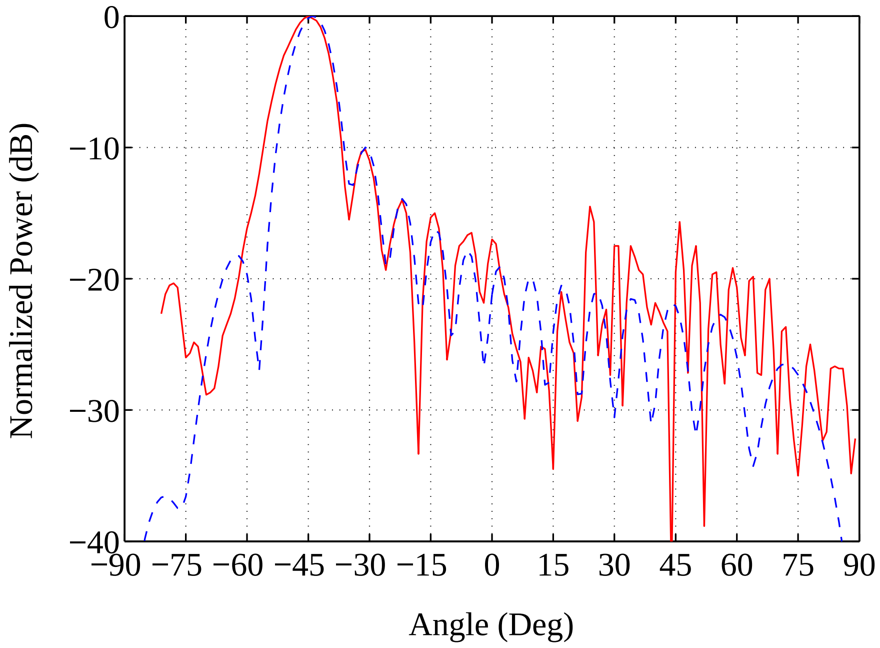

Figure 3.14: Measured (red solid line) and calculated (blue dashed line) lens array radiation patterns for a beam steered to $-45°$.

Two sets of *thru* measurements are discussed. In the first one, the receiving antenna is positioned at the focal distance, F=324 mm, and in the second, the feed is moved to the position which minimizes the path length error (at the optimum focal arc), which for a beam at boresite is equal to G=458 mm. The distance between the transmitter and the lens array is 3.6 m. The lens array is mounted in an absorber aperture of the same size as the lens. The total absorber size is 60 cm^2. The measurements were made for the system calibrated in two ways: without the absorber and through the aperture in the absorber. Table 3.1 summarizes these measurements for both polarization

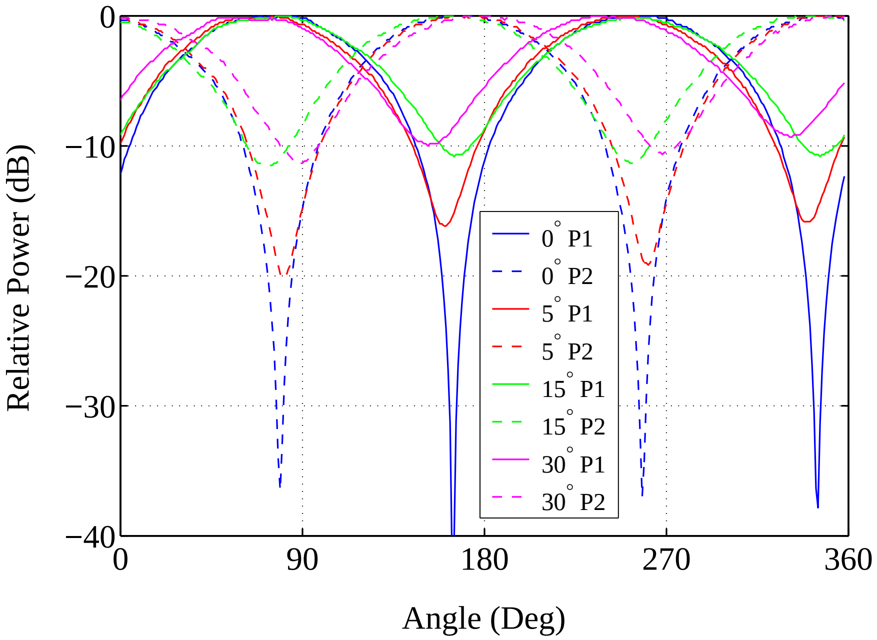

Figure 3.15: Measured polarization properties for the two polarization states of the lens array for four scan angles (0°, 5°, 15°, and 30°) as the transmitting horn polarization is rotated.

states of the lens.

This measurement tells us how efficient our system is in collecting the RF power relative to the system without the lens array. Since the effective area is increased in the presence of the lens array we would expect to be able to collect more power. However, the results in Table 3.1 show us that the total received power is in most cases below the level that we would receive using the receiver antenna alone. This is due to the loss in the system where the main contributor is the spill-over loss. This loss can be significantly reduced if we design the lens array and the receiving antenna as a system. In the

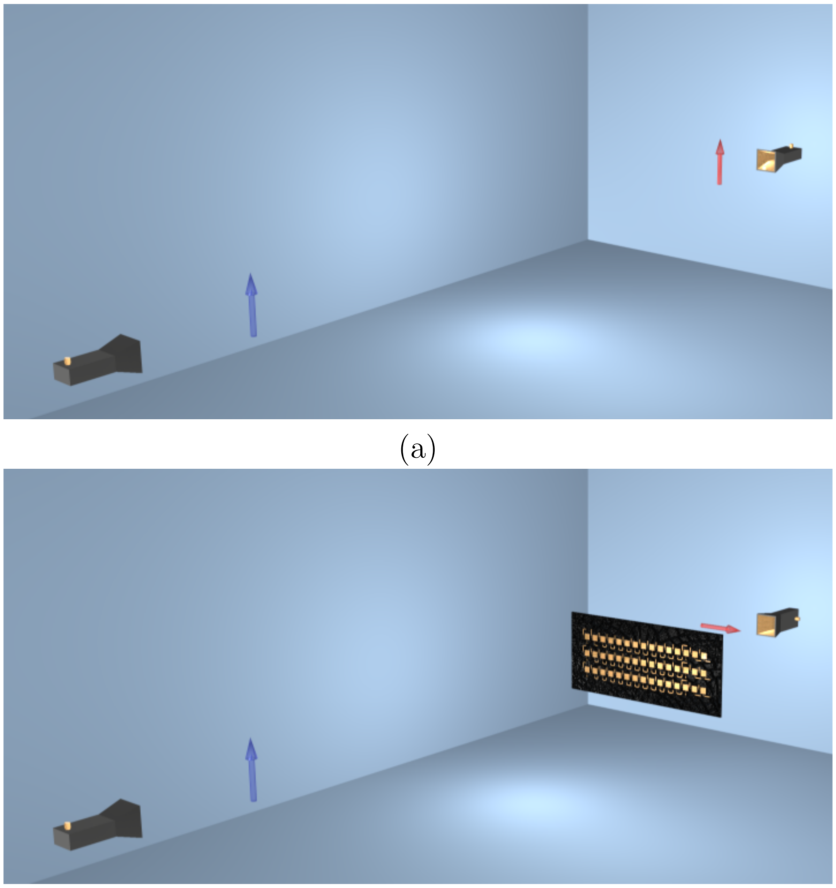
(a)

(b)

Figure 3.16: *Thru* measurement calibration (a) and measurement setup (b). Distance between the transmitting horn antenna and the lens array is 358 cm. Blue and red arrows show the polarization of the transmitting and the receiving horn antennas, respectively. Measurements are taken for the receiving horn antenna positioned at a distance F from the lens array and at the optimal focal arc G.

case of the cylindrical lens, which we are considering here, this would lead us to a receiver in the form of an antenna array with several antenna elements

Table 3.1: *Thru* measurements of the lens array for a feed located at the focal distance and at the optimum focal arc for the two polarizations. The measurements were done using two different calibrations (with and without the aperture).

Polarization of Tx/Rx	Feed distance (mm)	Relative received power(w/o aperture)	Relative received power(with aperture)
Tx-V, Rx-H	F=324	-2.2 (dB)	-0.7 (dB)
Tx-V, Rx-H	G=458	-4 (dB)	-3.9 (dB)
Tx-H, Rx-V	F=324	-1.5 (dB)	0.9 (dB)
Tx-H, Rx-V	G=458	-3.5 (dB)	-2.9 (dB)

positioned in the vertical plane where most of the power gets focused. If the received power level is critical we should, instead of a cylindrical design, use a square or circular lens array.

The same measurement was also performed using an HP8510 Network Analyzer with the *thru* calibration (which is the reason why the name, *thru* , is used for this type of measurement) and time gating to avoid the multipath effects. The measurement is taken in the frequency range from 9 GHz to 11 GHz and the resuls are presented in Figure 3.17.

The central frequency of the lens array is 10 GHz, which is exactly the frequency for which the lens was designed.

3.2.5 Loss Budget

The approach used for calculating the loss in the lens array system, presented in Chapter 1, is applied here in the case of the cylindrical 45-element lens array with a patch antenna used as a feed. The losses were calculated and

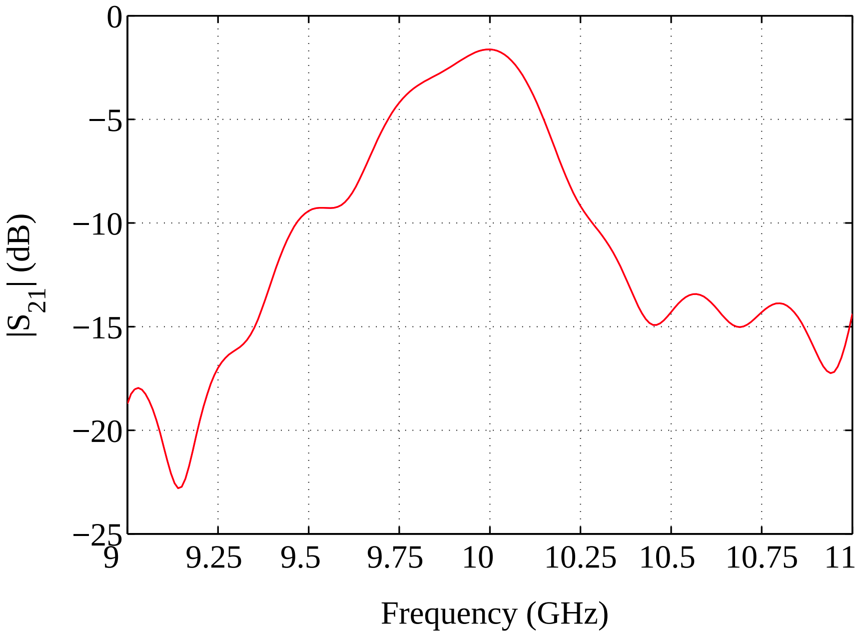

Figure 3.17: *Thru* measurement results for the frequency range from 9 GHz to 11 GHz.

are presented in Table 3.2

It was mentioned in the previous chapter that the dominant loss mechanism is the spill-over loss. In this case it is as high as 14 dB. Since the feed antenna has a low gain and the F/D number is relatively high $(F/D = 1.5)$ the amplitude distribution at the lens array is almost uniform. This is the reason why the taper loss is very small (fraction of a dB). The scan loss is equal to zero since the feed is located at the optical axis $(\theta = 0°)$. All the antennas in the system are assumed to be 80 % efficient, which relates to the loss of 0.97 dB. The loss in the via connection and the transmission line section is estimated to be 0.5 dB each. Figure 3.18 presents the losses as

Table 3.2: Losses in the lens array (Lens1).

Losses independent of the scan angle	Losses dependent of the scan angle
$\varepsilon_d = 0.97\,\text{dB}$	$\varepsilon_{sc} = 0\,\text{dB}$
$\varepsilon_{fs} = 0.97\,\text{dB}$	$\varepsilon_{so} = 14\,\text{dB}$
$\varepsilon_{nfs} = 0.97\,\text{dB}$	$\varepsilon_{tl} = 0\,\text{dB}$
$\varepsilon_v = 0.5\,\text{dB}$	$\varepsilon_a = 0\,\text{dB}$
$\varepsilon_t = 0.5\,\text{dB}$	
$\varepsilon_l = 3.9\,\text{dB}$	

functions of the scan angle.

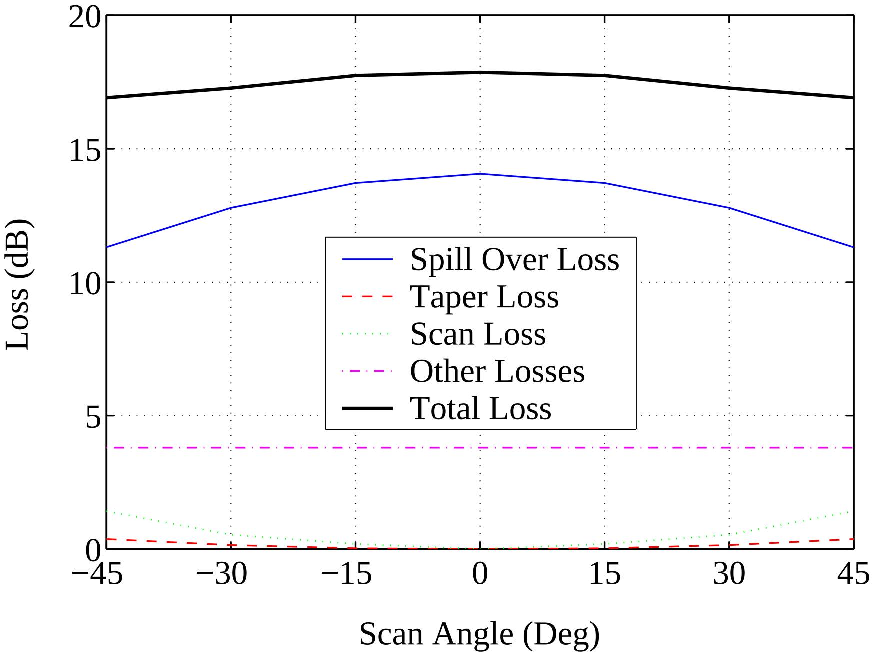

Figure 3.18: Losses in the lens array vs. the scan angle.

Most of the losses, as expected, are either constant or increase as we scan off the optical axis. However, the spill-over loss decreases as we scan off axis. This result could seem counterintuitive. If the detectors is moved along the focal arc with the fixed radius the angles subtended from the positions of the detectors looking at the lens will decrease as the detector is moved along the focal arc and away from the optical axis. However, the detectors are positioned at the optimal focal arc and not on the fixed distance, F. Therefore, they get closer to the center of the lens as we scan off axis resulting in the decrease of spill-over loss. This result is beneficial in the lens array design and allows for relatively uniform main beams for different angles of scan.

The directivity of the lens array is found to be 23.4 dB. The gain can then be calculated as

$$\begin{aligned} G_{max}(\theta = 0) &= -\varepsilon_l - \varepsilon_{so} - \varepsilon_{tl} - \varepsilon_a + D_{umax}(\theta = 0) \\ &= -3.9\,\mathrm{dB} - 14\,\mathrm{dB} - 0\,\mathrm{dB} - 0\,\mathrm{dB} + 23.4\,\mathrm{dB} \\ &= 5.5\,\mathrm{dB} \end{aligned} \tag{3.1}$$

3.2.6 Image on the Focal Surface

If the lens array is used in receiving mode, the plane waves coming from different angles with respect to the lens will form different images on the focal surface. The maximum power density will correspond to the direction of arrival of the plane wave, as expected. However, the lens array design will determine the *spot-size*, to use the terminology from optics, as well as the shape of the spot. This information will help us design the optimal feed for the particular lens array. For the lens array that has cylindrical shape, like the one discussed in this chapter (3 rows by 15 columns), one can expect an image that has an elliptical shape with the major axis perpendicular to the longer dimension of the lens array. Figures 3.19(a) and Figure 3.19(b) represent the images calculated for the plane waves coming form $\theta = 0^\circ$ and $\theta = 30^\circ$, respectively. The black squares at these figures show an approximate effective array of the feed antenna. One can see that only small portion of the total power will be collected by the feed antenna resulting in a significant spill-over loss. In order to minimize the loss different feed antenna should be used as described in Section 3.2.4.

3.3 Conclusions

A cylindrical dual-polarized discrete lens array is presented. The unit cell and the lens array are fully characterized and the measured results are compared with the simulations. The lens is designed to work in X-band with the center frequency at 10 GHz, and the measured results show that the frequency requirement is satisfied. The radiation patterns for the lens array are taken for seven different feed positions within the scan region (-45° to 45°). The results show that the lens could be used for wide scan angles with moderate degradation of its performance in terms of side lobe levels, half-power beamwidth, axial ratio, etc. A *thru* measurement was used before as

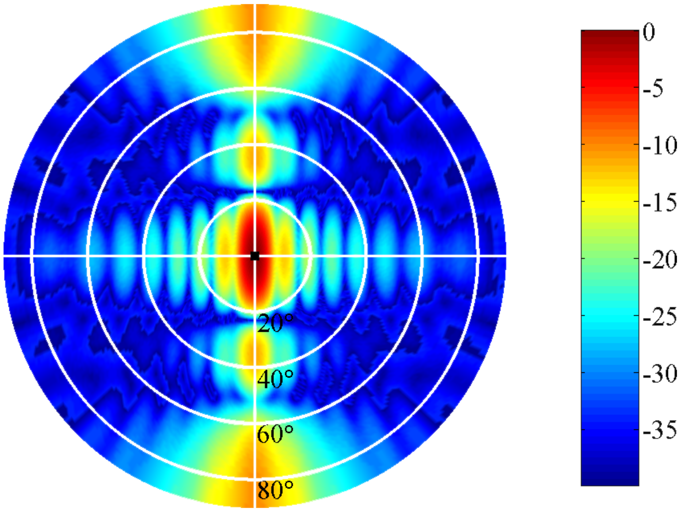

(a)

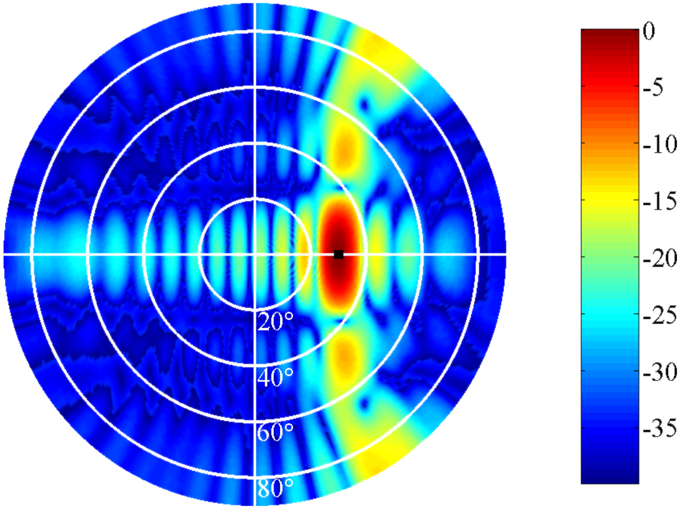

(b)

Figure 3.19: Image at the focal surface for the plane wave coming from $\theta = 0^\circ$ (a) and $\theta = 30^\circ$ (b).

one way of characterizing these type of systems [32, 33]. In this chapter a physical explanation of the results that this measurement provides is given, which contributes to a better understanding of lens array systems. The loss budget calculation was performed isolating different loss mechanisms. The uniformity of the main beam power levels in the wide range of the angles of scan are explained in light of the loss calculations. Finally, the power density at the focal surface of the lens array is calculated for plane waves incident at two different angles in order to investigate how feed antenna affect efficiency.

Chapter 4

Dual-Polarized Broad-Band Lens Array

4.1 Motivation

In order to make the lens array more efficient and applicable in different communication systems a new design is investigated. The following specifications and improvements are desired.

- Dual polarization is still one of the requirements.
- Instead of the scanning in only one plane, full three-dimensional scanning is of interest in this design.
- The spill-over loss was the major loss mechanism in the first design. The feed and the lens array have to be designed as a system to provide

lower spill-over loss.

- The side-lobe levels that ranged from -15 dB to -10 dB in the first lens array design should be minimized.
- The beam uniformity can be further improved.
- The lens array should also have higher bandwidth, to make it usable in broadband applications.

The unit cell design is presented in Section 4.2. Measured and simulated data for the isolated antenna element are given in Section 4.3. The lens array design and measurement is provided in Section 4.4 and Section 4.5.

4.2 Unit Cell Design

Selection of the antenna element for this project is influenced by several requirements.

- The antenna has to be dual-polarized.
- The bandwidth of the antenna has to be about 10 % of the central frequency.
- The design should also allow insertion of low noise amplifiers, power amplifiers or some other components (phase shifters, variable attenuators etc.).

- The antenna should be easy to manufacture and compact, in order to make it applicable for the low-cost CLA design.

Microstrip patch antennas have been extensively researched and used for more than twenty years. They are easy to manufacture, light weight, conformal and MMIC compatible. One of the main drawbacks in microstrip antennas was their limited bandwidth. Several methods are used to widen the frequency bandwidth [34, 35, 36] of a microstrip patch antenna. A technique that is used in resonant circuits, such as filters where several resonators are coupled with closely spaced resonances, is applied to microstrip patch antennas as well. That is either done by exciting several resonant modes of a single patch (16 % 2:1 VSWR bandwidth can be achieved using this method [37]) or by using several radiating structures closely coupled to each other with slightly different resonant frequencies. An example of a rectangular microstrip patch antenna with the parasitic elements placed at the same level is shown in Figure 4.1 [38]. Only the main radiator is directly driven by the feed line and the side elements, in this case dipoles, are excited by coupling from the driven patch. The parasitic elements are placed symmetrically on both sides of the central patch to provide maximum radiation normal to the antenna plane and to keep the cross-polarization level low. The length of the parasitic elements is used as a design variable. Patch antennas can also be used as parasitic elements. They can be either gap coupled or directly coupled to the central patch and positioned either along its radiating edges or along its non-radiating edges [39, 40]. A bandwidth of up to five times that

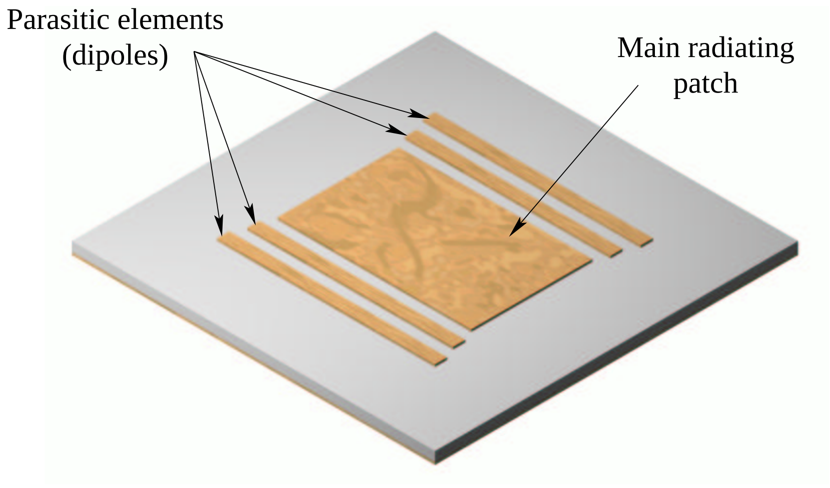

Figure 4.1: Patch antenna with coplanar parasitic elements [38].

of a single rectangular patch antenna is reported in [41] where two patches are gap coupled to the main patch along the radiating edges.

Another design uses parasitic element (or elements) stacked on top of the main radiator. This is known as a *stacked* patch antenna [42, 43]. Unlike the coplanar parasitic elements, the stacked elements do not increase the surface area compared to that of a single patch antenna. That is very important in the antenna array design where the unit cell size has to be small for grating lobes to be avoided. An exploded view of a stacked patch antenna with aperture coupling is presented in Figure 4.2 The upper patch is proximity coupled to the excited bottom patch. The design variables that can be used in the stacked patch configuration are dielectric constants and thicknesses of the substrates, patch sizes, feed locations and offsets between the patch centers. They can be optimized for broad-band applications as

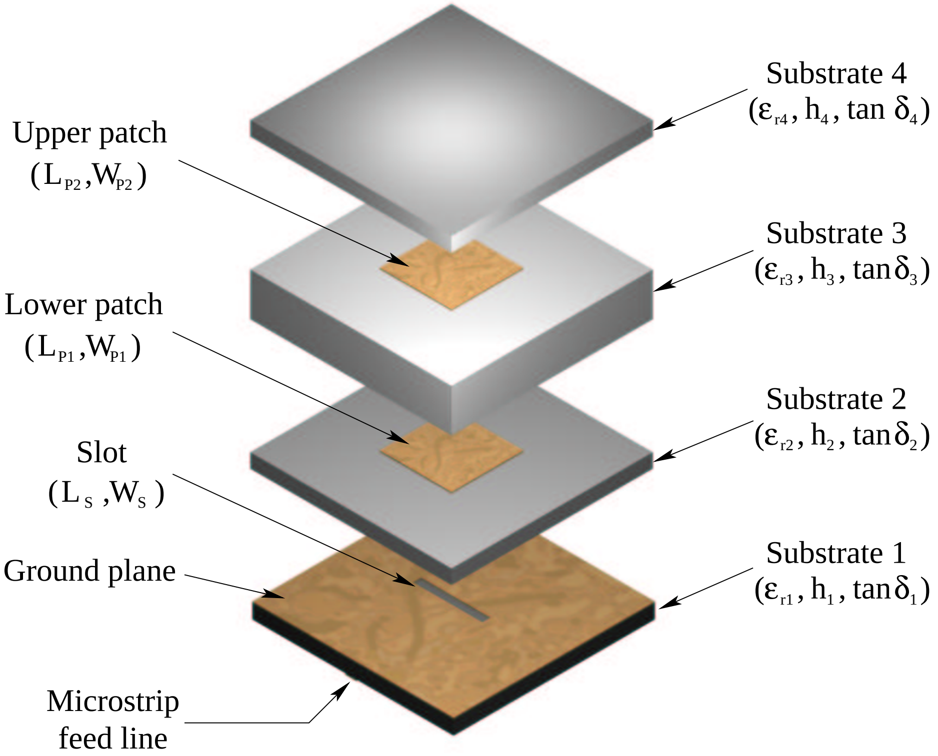

Figure 4.2: Exploded view of a stacked patch antenna with aperture coupling

well as for dual-frequency applications. In the case presented in Figure 4.2 there are three resonators: two patches and the aperture. These resonators experience mutual couplings which are controlled by changing the resonant frequencies and the parameters of the substrates between them. The results are the loops in the impedance locus when plotted on a Smith chart. In the approach presented in [42] two tight loops around the center of the Smith chart are obtained. This results in a 1.5:1 VSWR (voltage standing wave ratio) bandwidth of 44 %. One of the loops is produced by the interaction of the two patches and the other one by the interaction of the aperture with the lower patch. A disadvantage of this is relatively high back radiation, - 10 dB in this case.

Instead of aperture coupling shown in Figure 4.2 the bottom patch can be fed by a coaxial probe [44] or by a microstrip line. The latter is used in the design presented here. It has only two resonators and the bandwidth will, therefore, be lower compared to that where three resonators are used. However, this approach is simpler to fabricate since it has three metal layers instead of four. The dual polarization is easily achieved by adding another microstrip feed line, keeping the same number of layers (Figure 4.3). If aperture coupling were used a total of five [45] layers would be required. Simplicity of the unit cell is an important factor in the CLA design where the number of elements is large (hundreds) and the number of layers is doubled since two arrays are connected back to back. The ground plane minimizes the back radiation, which is another advantage of the design applied here, as will be shown in Section 4.3.2.

An exploded view of the antenna is given in Figure 4.3. It consists of two square patches built on ULTRALAM 2000 dielectric material separated by the Rohm Rohacell 31 HF foam. The same dielectric material is used as in the first design, since it proved efficient in manufacturing of relatively big boards, where the uniformity and flatness is important. The foam is 3 mm thick with a permittivity of 1.07 and the loss tangent of 0.004. The upper patch is an inverted patch, which means that the dielectric material

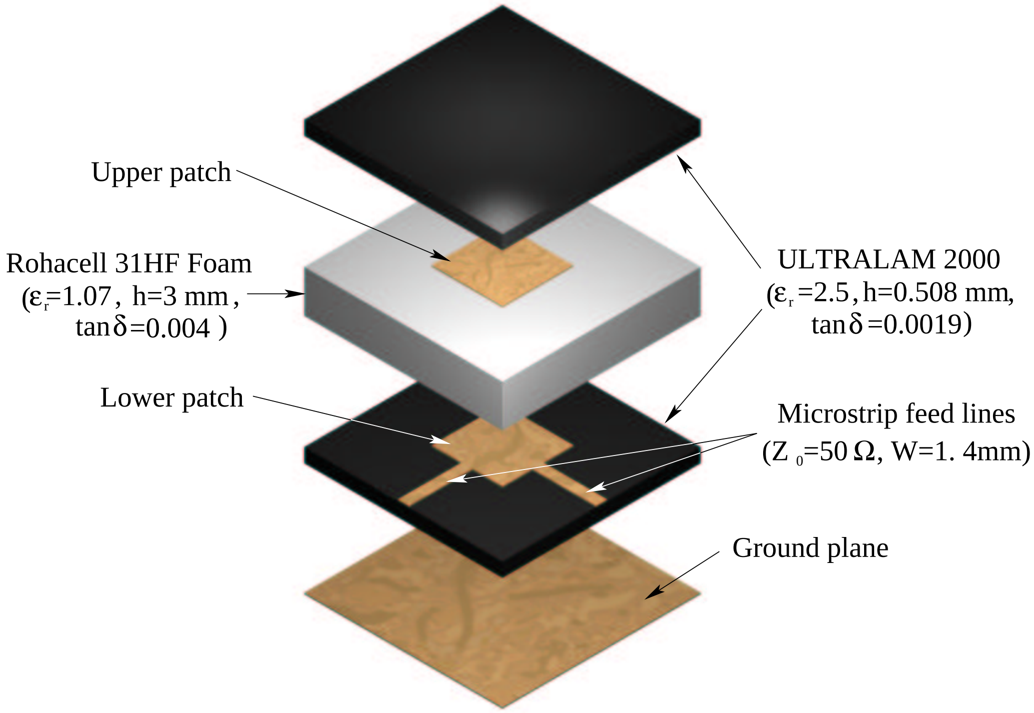

Figure 4.3: Dual-polarized stacked patch antenna with $50\,\Omega$ microstrip feed lines.

can be used as a radome. The microstrip feeds are located on the same level as the lower patch. The upper patch dimensions and the distance from the lower patch are used as design variables. They are optimized using Zeland's IE3D Method of Moments software. There are two optimization goals. The first one is the frequency bandwidth requirement and the second one is the antenna's input impedance. By lowering the input impedance of the stacked patch antenna to $50\,\Omega$, the $\lambda/4$ matching sections are eliminated. As a result, the feed becomes more compact which is beneficial in the antenna array design. The foam that separates lower and upper patch can be replaced with air. That allows for the insertion of active components and an efficient power dissipation handling. Most MMIC amplifiers are matched to $50\,\Omega$ and can directly be used on the microstrip feed lines designed with the characteristic impedance of $Z_o = 50\,\Omega$. Both optimization goals are satisfied with a final antenna which consists of two square patches with the same dimensions of $9.1\,\text{mm}^2$, spaced 3 mm apart. The width of the $50\,\Omega$ transmission line is 1.4 mm.

4.3 Unit Cell Measurement and Analysis

Several antennas were built and tested. When air is used between the two patches instead of foam the antenna characteristics do not change. In these cases the spacings between the lower and the upper patch is set to 3 mm using nylon spacers.

4.3.1 Scattering Parameters

The 2-port S-parameters of the stacked patch antenna element were measured using an HP8510 Network Analyzer with a 3.5 mm coaxial calibration and are compared to simulations obtained using Zeland's IE3D Method of Moments software, as shown in Figure 4.4(a) and Figure 4.4(b). From the reflection coefficients at ports 1 and 2 one can see that the 2:1 VSWR bandwidth is 900 MHz around the central frequency of 10.3 GHz, a 9 % fractional

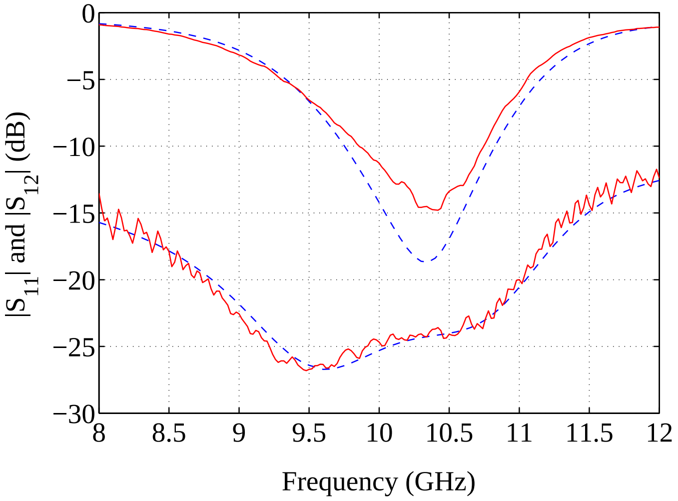

(a)

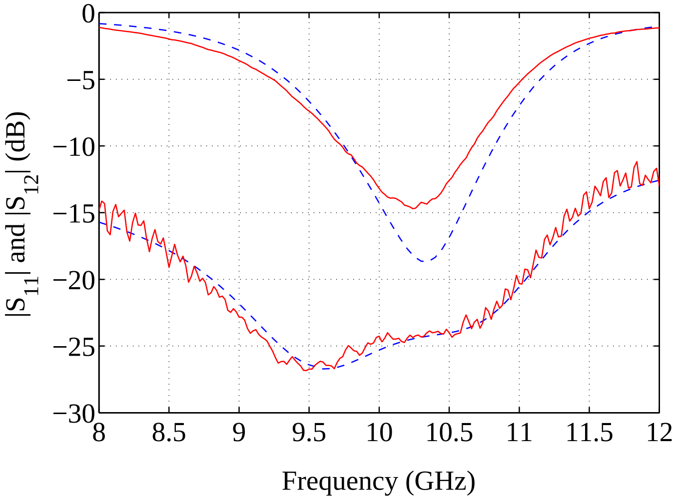

(b)

Figure 4.4: Measured (red solid lines) and simulated (blue dashed lines) two-port unit cell *s*-parameters, where the ports correspond to orthogonally polarized feeds. The ripple in the measured s_{12} and s_{21} parameters is the result of a 3.5 mm coaxial calibration which is used instead of a TRL calibration.

bandwidth. The s_{21} parameter shows -24 dB of isolation between the ports.

4.3.2 Radiation Patterns

The measured co-polarized and cross-polarized (E- and H-plane) radiation patterns of the antenna element are given in Figure 4.5. The patterns are measured for the entire 360° angular scan. The signals received at two ports are measured simultaneously: H-plane radiation patterns are measured at the port with the vertical orientation, and the port with the horizontal orientation receives signals in the E-plane. The asymmetry that exists in

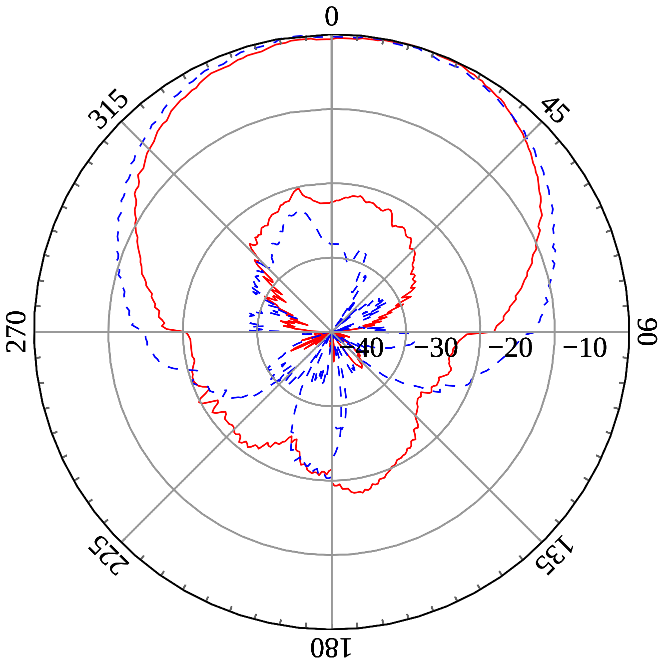

Figure 4.5: Measured element E-plane (red solid lines) and H-plane (blue dashed lines) co-polarized and cross-polarized radiation patterns.

the previous lens is eliminated in this design. The cross-polarized signal is more than 20 dB below the co-polarized, and the back radiation is at a level of -20 dB or lower.

4.4 Lens Array Design

The lens array discussed in this chapter is based on the symmetrical approach. As described in Chapter 1, a symmetrical design does not have perfect focal points (unless $\theta_0 = 0^\circ$), but instead has a cone of best focus. The design is based on the antenna element described in Section 4.2 and Section 4.3. The lens array has 165 antenna elements in a rectangular configuration. The design started with 15×15 elements, with the unit cell size of $(0.6 \times 0.6)\,\lambda^2$. Fifteen elements at each corner of the array are eliminated resulting in a lens with an octagonal shape. There are two reasons for elimination of the elements at the corners. The offsets between the antenna elements at the non-feed side and the feed side of the lens array become too big, making the design impossible. The second reason is in the fact that an octagonal shape gives lower side-lobe levels in two principal planes. An exploded view of the lens array is presented in Figure 4.6 The lens consists of two antenna arrays that share the same ground plane. Each array has three metal layers: the ground plane and the two microstrip patch arrays. The elements at the non-feed side and the feed side are connected with the metal-plated vias (not shown in figure). The dielectric material is transparent in Figure 4.6 to

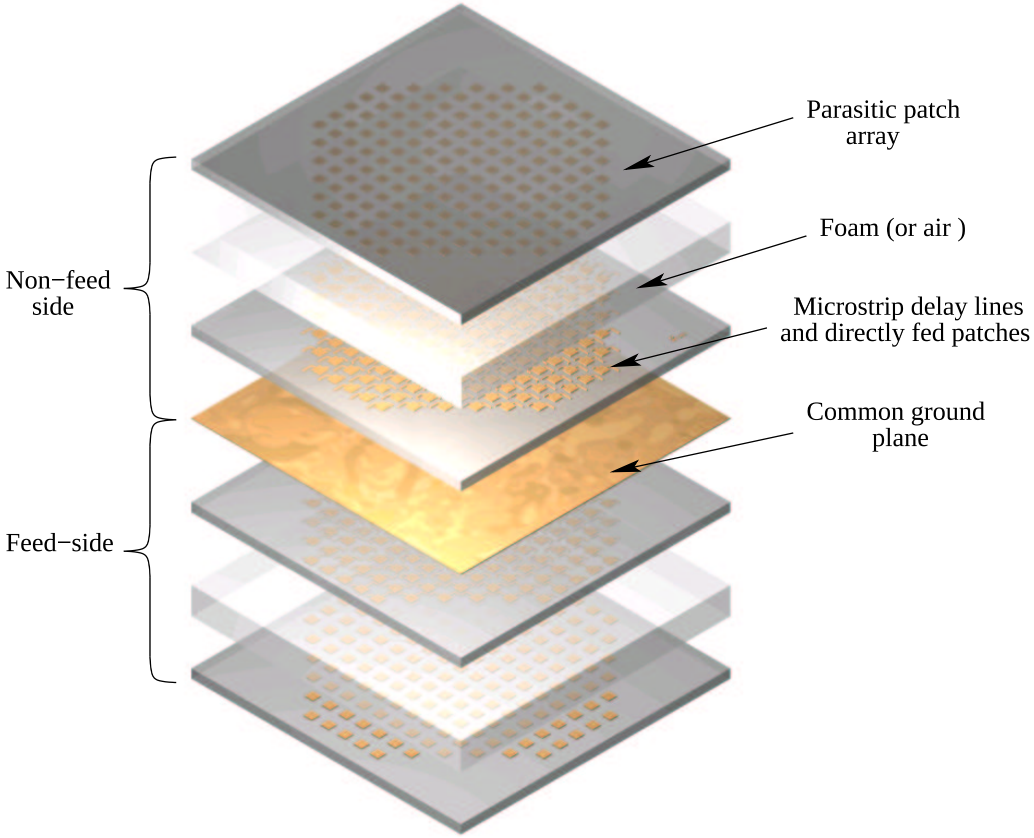

Figure 4.6: Exploded view of the 165-element lens array. Corresponding feed side and non-feed side antenna elements are separated by a common ground plane and connected with metal-plated vias (not shown in figure). Arrays with parasitic patches are separated by a 3 mm thick foam (or air) layer from the arrays with the directly fed patch antennas.

show the patch antennas on all the layers. The parasitic patches are used in an inverted configuration, providing a protective dielectric radome. Rohm Rohacell 31 HF foam is used between the patch antennas. Figure 4.7 shows the lower patches and the transmission lines at the non-feed side (red) and the feed side (green) of the lens array.

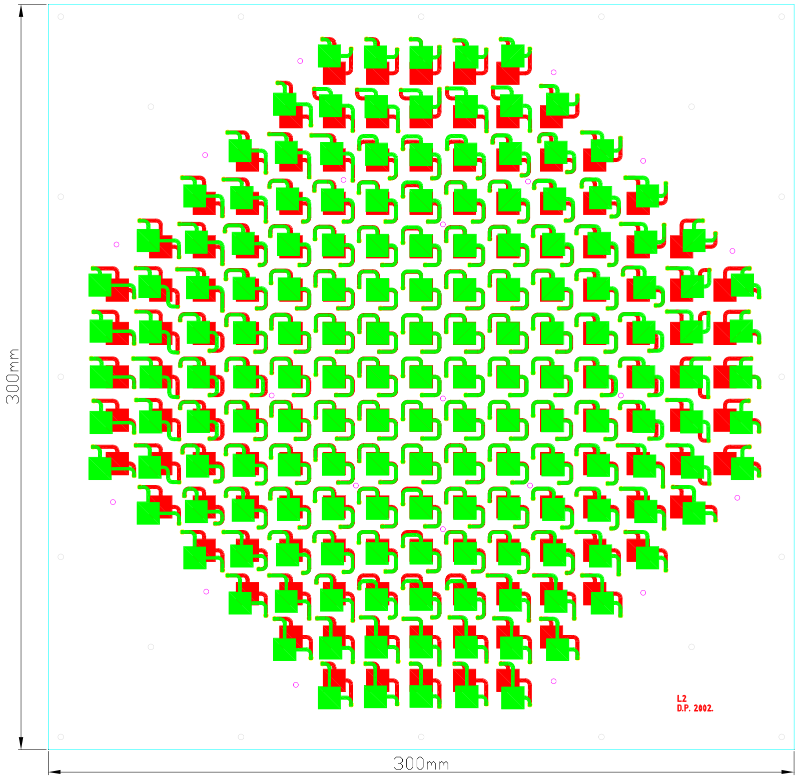

Figure 4.7: Outline of the antenna arrays on the feed side (green) and the non-feed (red) side of the 165-element lens array.

4.5 Lens Array Measurement and Analysis

In this section a full characterization of the lens array is presented. Radiation pattern measurements are presented and discussed in Section 4.5.1. Polarization characterization is given in Section 4.5.2. The results of the *thru* measurement are shown in Section 4.5.3. The loss budget and the image calculation is presented in Section 4.5.5 and Section 4.5.6, respectively.

4.5.1 Radiation Pattern

The radiation pattern of the lens array is measured in the anechoic chamber for five different angles within the scan range (-30°, -15°, 0°, 15°, 30°). Measured data is presented in Figure 4.8. A standard horn antenna is used as a transmitter. A dual-polarized stacked patch antenna presented in Section 4.2 is used as a feed. The feed antenna is moved along the focal arc and the radiation patterns are measured one at the time. The two ports are connected to two HP437B power meters and measured simultaneously. The variation of the maximum beam power as a function of scan angle is given in Figure 4.9. One can see that the peak varies by only 1 dB (red solid line) in the E-plane and not more than 2 dB in the H-plane (blue dashed line). The half-power beamwidth of 7° for a beam on boresite changes less than 1.5 % in both principal planes over the 60° scan range (Figure 4.10). The measured radiation patterns (red solid lines) for five different angles are compared with the calculated data (blue dashed lines) and presented in Figure 4.11, Figure 4.12 and Figure 4.13. One can see from these graphs that the side-lobe levels range from -22 dB for the beam at 0° to -17 dB for a beam steered to $\pm 30^\circ$.

The lens array was surrounded with the absorber during the measurements to isolate the feed side and tho non-feed side of the lens. However,

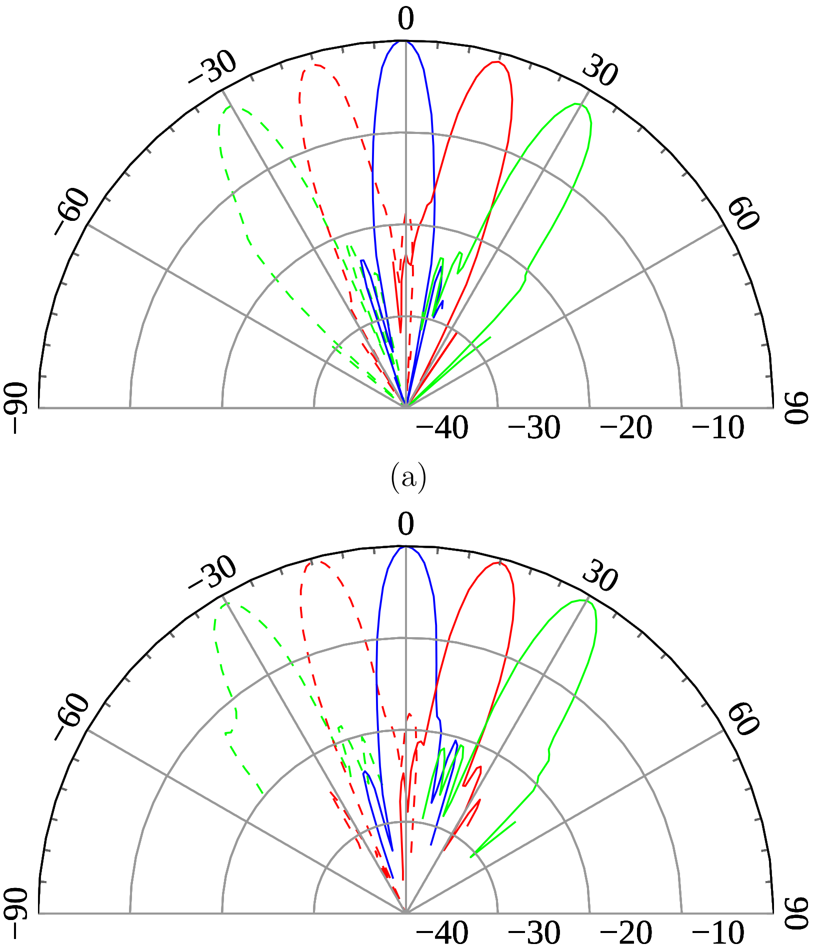

(a)

(b)

Figure 4.8: Measured E-plane (a) and H-plane (b) radiation patterns of the lens array for the feeds positioned at: −30°, −15°, 0°, 15°, 30°

for large angles of scan the feed antenna is not in the shade of the absorber and a direct line of sight from the feed antenna to the transmitting antenna exists, resulting in an increase in the sidelobe levels. Absorbers placed on

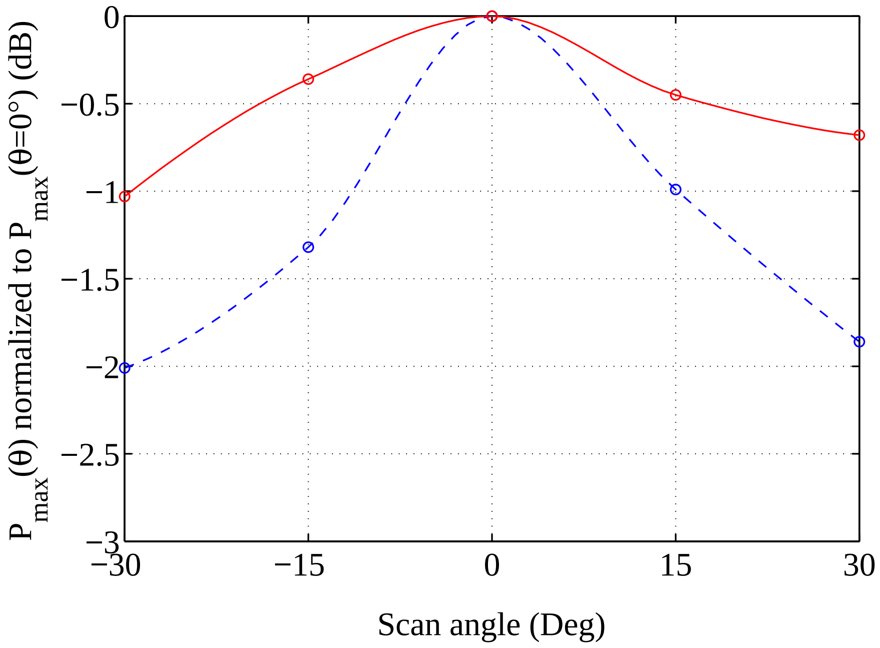

Figure 4.9: Measured maximum received power as the receiver is moved along the optimal focal arc. The peak varies by only 1 dB (red solid line) in the *E*-plane and not more than 2 dB in the *H*-plane (blue dashed line)

the sides are used for better isolation but certain amount of direct signal is still received as shown in Figure 4.12 and Figure 4.13.

In order to check the system performance within the frequency bandwidth the radiation patterns were measured at five different frequencies within the bandwidth. Normalized data is presented in Figure 4.14. The half-power beamwidth decreases from 7.5° at 9.4 GHz to 5.7° at 10.6 GHz.

Simulated three-dimensional radiation pattern for the beam at boresite is given in Figure 4.15. One can see a pencil beam with the sidelobes that are positioned in the diagonal planes due to the shape of the lens array. That is

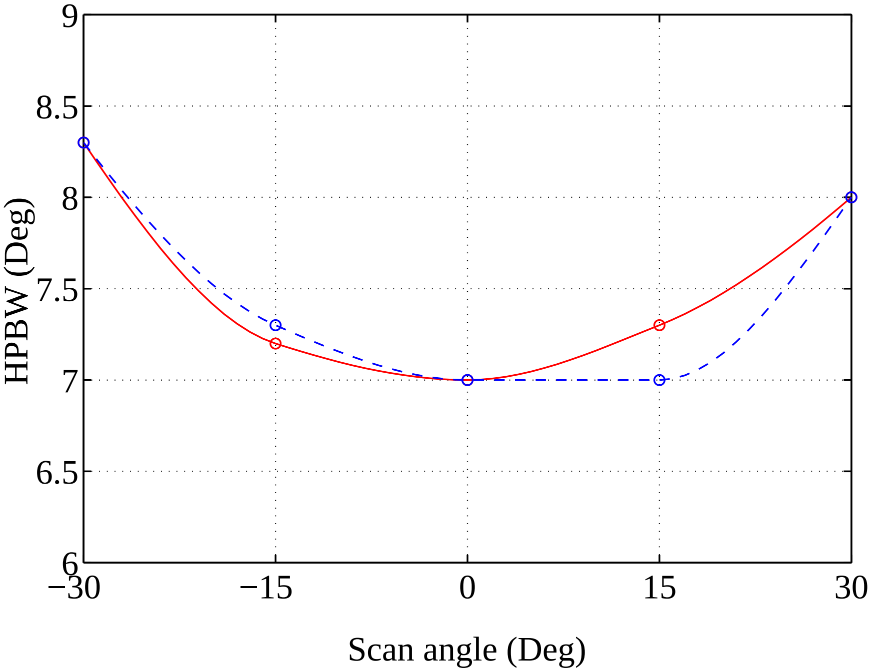

Figure 4.10: Measured half power beamwidth (HPBW) as the receiver is moved along the optimal focal arc. The HPBW changes only 1.25° in the 60° scan range.

th reason for a relatively low sidelobe level in the E and H planes.

4.5.2 Polarization Characterization

The polarization characterization was performed with the transmitting antenna rotated from 0° to 360° and the dual-polarized stacked patch antenna used as a feed antenna. The power received at two ports which correspond to vertical and horizontal polarizations and for five positions of the feed antenna along the focal arc is presented in Figure 4.16. The cross-pol is -14 dB

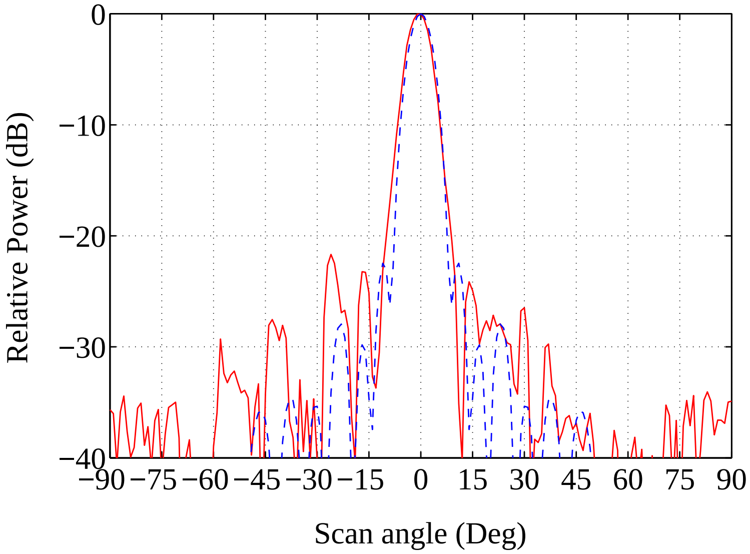

Figure 4.11: Measured (red solid line) and calculated (blue dashed line) lens array radiation patterns for a beam at 0°.

in average and it changes less than 1.5 dB as the beam is scanned from 0° to ± 30°.

4.5.3 *Thru* Measurement

A *Thru* measurement is done using the setup given in Figure 3.16. Since the lens array discussed in this chapter does not rotate the polarization, the transmitting horn antenna is kept in the same polarization state during the measurement as it is during the calibration. The result obtained using the calibration without the aperture and the feed antenna positioned at the optimal focal arc on the optical axis gives $|s_{21}|$ =8.6 dB. If we compare that result to $|s_{21}|$ =- 4 dB obtained in the equivalent measurement of the first

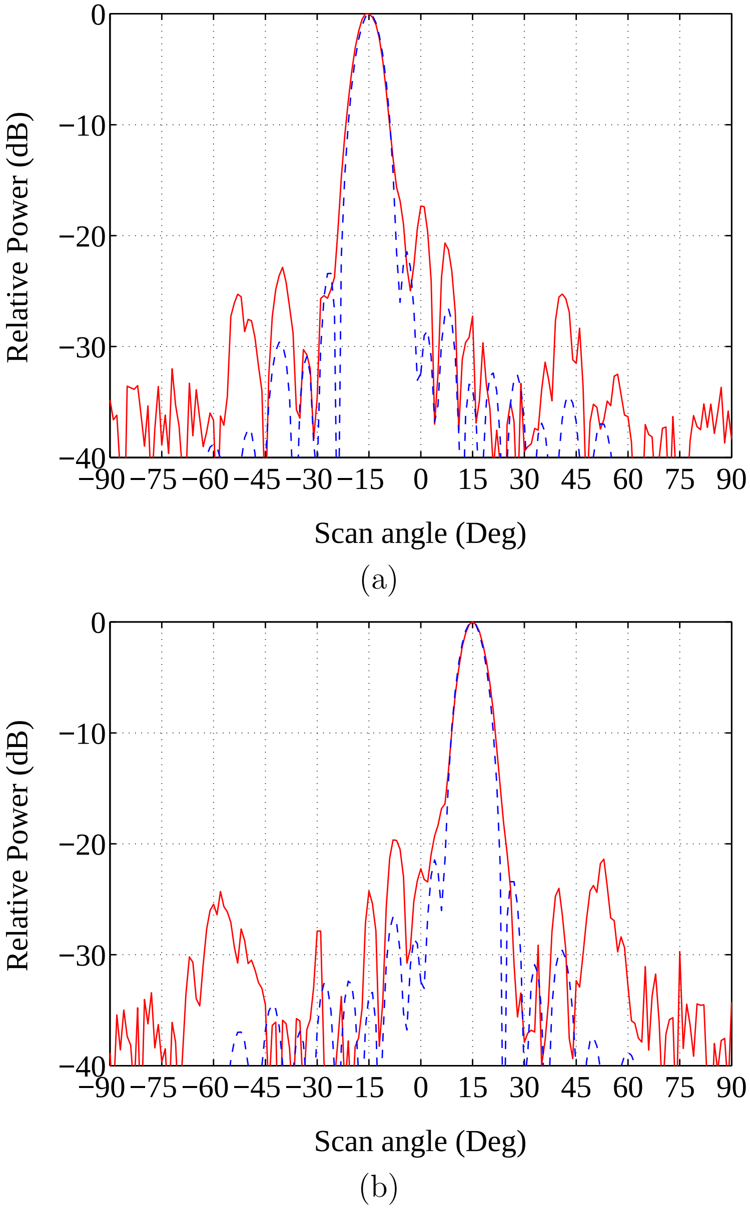

Figure 4.12: Measured (red solid line) and calculated (blue dashed line) lens array radiation patterns for a beam at ±15°.

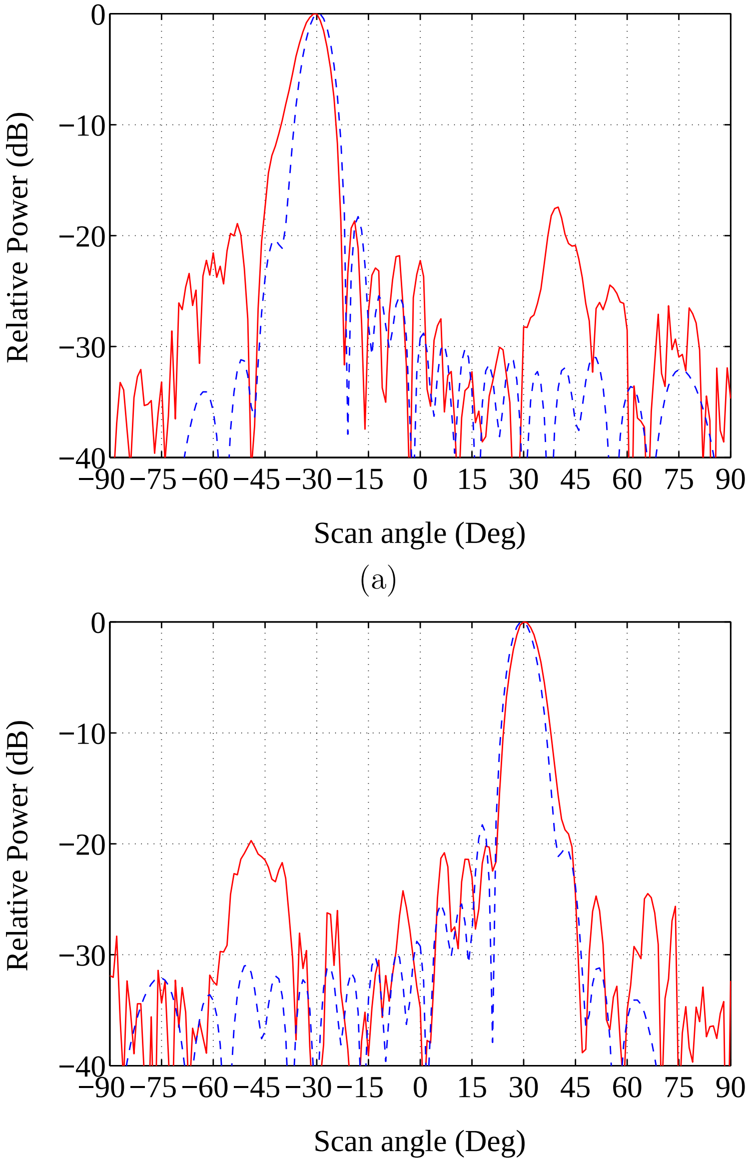

(a)

(b)

Figure 4.13: Measured (red solid line) and calculated (blue dashed line) lens array radiation patterns for a beam at ±30°.

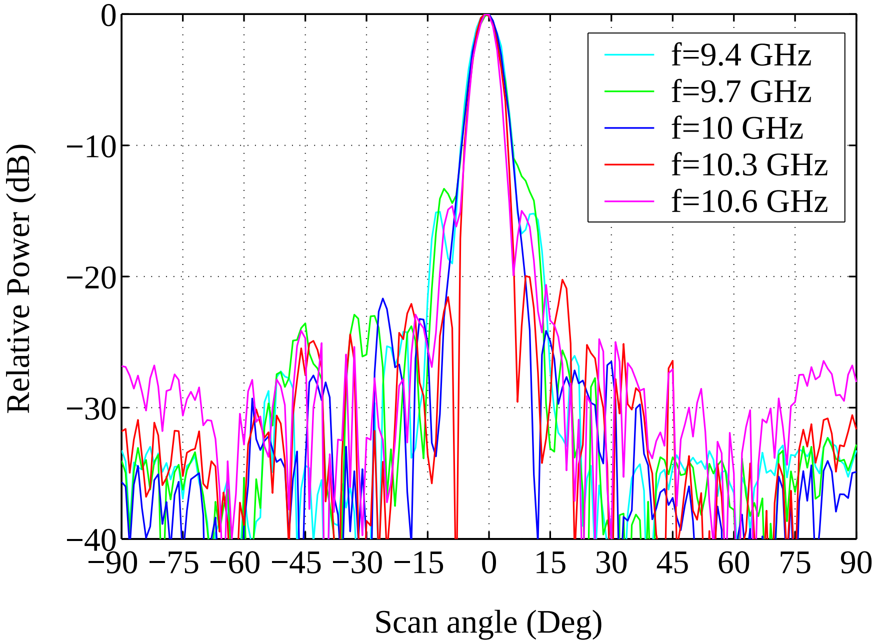

Figure 4.14: Measured lens array radiation patterns for a beam at 0° for five different frequencies.

lens array, an improvement of 12.6 dB is achieved. The *thru* measurement is repeated in the frequency range from 8 to 12 GHz with 0.1 GHz resolution, and the normalized results are presented in Figure 4.17. The maximum corresponds to f =10.3 GHz which is the designed central frequency of the lens.

4.5.4 Path Length Errors

The lens array discussed in this chapter is based on a symmetrical design. It was already mentioned that this design does not have the perfect focal points,

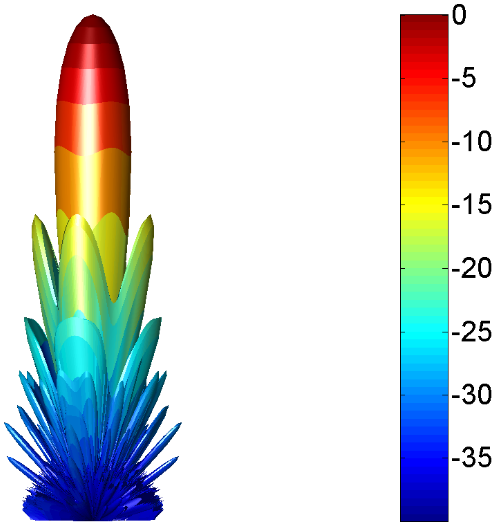

Figure 4.15: Simulated 3D radiation pattern for the lens array.

but rather a cone of best focus. The path length errors are greater than zero for all scan angles but are minimized in one region of the focal surface. Instead of calculating the path length errors from each antenna element in the lens array, a root-mean-square path length error can be calculated. That value takes into account the contributions of all the elements in the array The root-mean-square path length error is calculated as a function of the scan angle θ (elevation) and it is presented in Figure 4.18. The solid line shows the case with the fixed focal distance F and the dashed line shows the case when the optimal focal distance G is used. One can see from this graph the effect of optimizing the focal distance. The path length errors are smaller

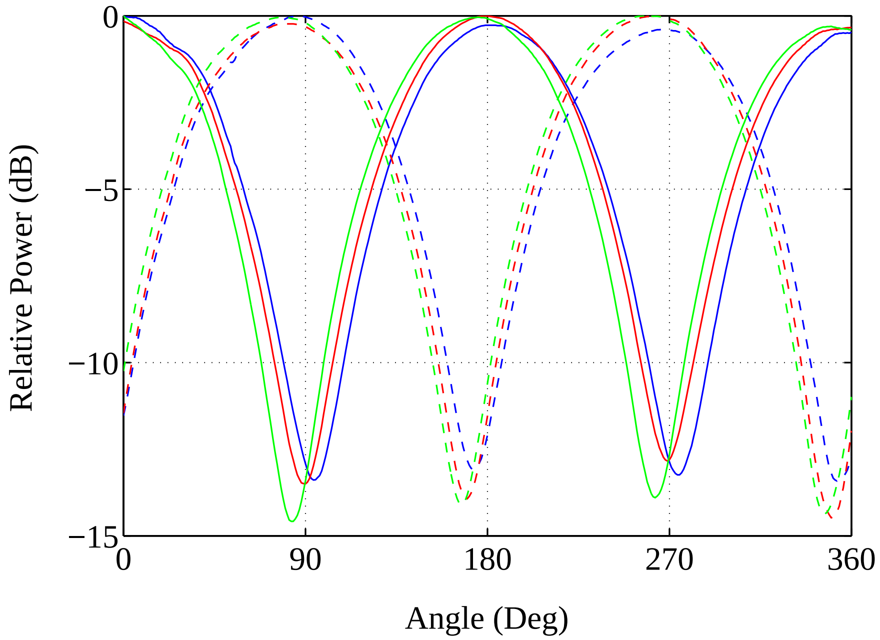

Figure 4.16: Measured polarization properties for the two polarization states of the lens array for three scan angles (0° blue lines, 15° red lines, 30° green lines) as the transmitting horn polarization is rotated.

and they are relatively constant in the scan range (−30° to 30°). The results shown in Figure 4.18 are calculated for 0° azimuthal plane. Since the design is symmetrical the graph will not change significantly for other angles.

4.5.5 Loss Budget

The losses in the system are calculated for a feed positioned at $\theta = 0°$ and presented in Table 4.1. The losses in the via transitions and transmission lines, and efficiencies of the antennas are assumed to be the same as those in the first design.

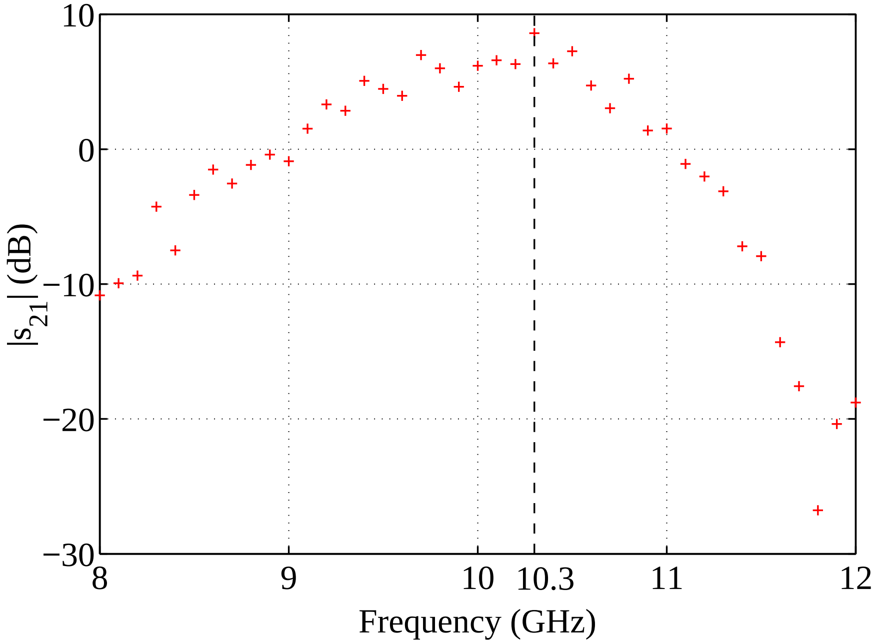

Figure 4.17: *Thru* measurement results for the frequency range from 8 GHz to 12 GHz. Note the maximum at 10.3 GHz, which is the designed central frequency for the lens array.

The directivity of the lens array is found to be 28.7 dB. The gain can then be calculated as:

$$
\begin{aligned}
G_{max}(\theta = 0) &= -\varepsilon_l - \varepsilon_{so} - \varepsilon_{tl} - \varepsilon_a + D_{umax}(\theta = 0) \\
&= -3.9\,\mathrm{dB} - 7.1\,\mathrm{dB} - 0\,\mathrm{dB} - 0\,\mathrm{dB} + 28.7\,\mathrm{dB} \\
&= 17.7\,\mathrm{dB} \qquad (4.1)
\end{aligned}
$$

This is an increase of 12.2 dB compared to 5.5 dB of gain calculated for the first lens design. An improvement observed in the *thru* measurement of

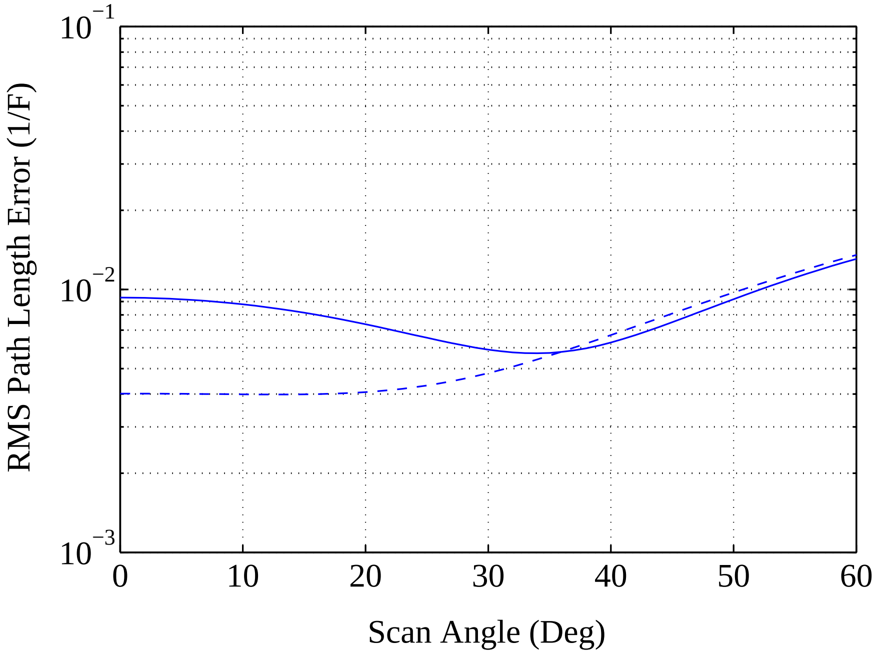

Figure 4.18: Root mean square path length error calculated at optimal focal arc G (solid line) and at fixed distance F (dashed line).

12.6 dB is very close to that value. The loss is calculated as a function of scan angle and presented in Figure 4.19. The total loss (black solid line) is relatively constant across the scan range which is the reason for the small variation in the maximal beam power.

4.5.6 Image on the Focal Surface

The image on the focal surface is calculated for two signals coming from 0° and 30° off axis. The results are presented in Figure 4.20(a) and Figure 4.20(b). If compared to the images calculated for the first lens array

Table 4.1: Losses in the lens array (Lens2).

Losses independent of the scan angle	Losses dependent of the scan angle
$\varepsilon_d = 0.97\,\mathrm{dB}$ $\varepsilon_{fs} = 0.97\,\mathrm{dB}$ $\varepsilon_{nfs} = 0.97\,\mathrm{dB}$ $\varepsilon_v = 0.5\,\mathrm{dB}$ $\varepsilon_t = 0.5\,\mathrm{dB}$	$\varepsilon_{sc} = 0\,\mathrm{dB}$ $\varepsilon_{so} = 7.1\,\mathrm{dB}$ $\varepsilon_{tl} = 0\,\mathrm{dB}$ $\varepsilon_a = 0\,\mathrm{dB}$
$\varepsilon_l = 3.9\,\mathrm{dB}$	

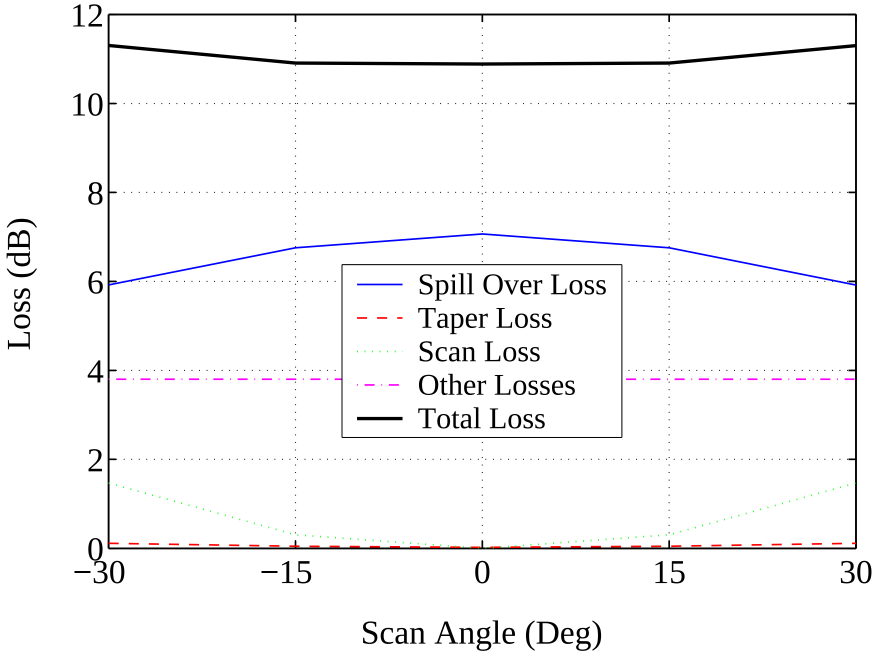

Figure 4.19: Losses in the lens array vs. the scan angle.

design, the new results show a change from elliptical to circular shape of the spot. The approximate effective area of the feed antenna is presented with the black squares positioned at 0° in Figure 4.20(a) and at 30° in Figure 4.20(b). The feed antenna can collect more of the focused power compared to the case

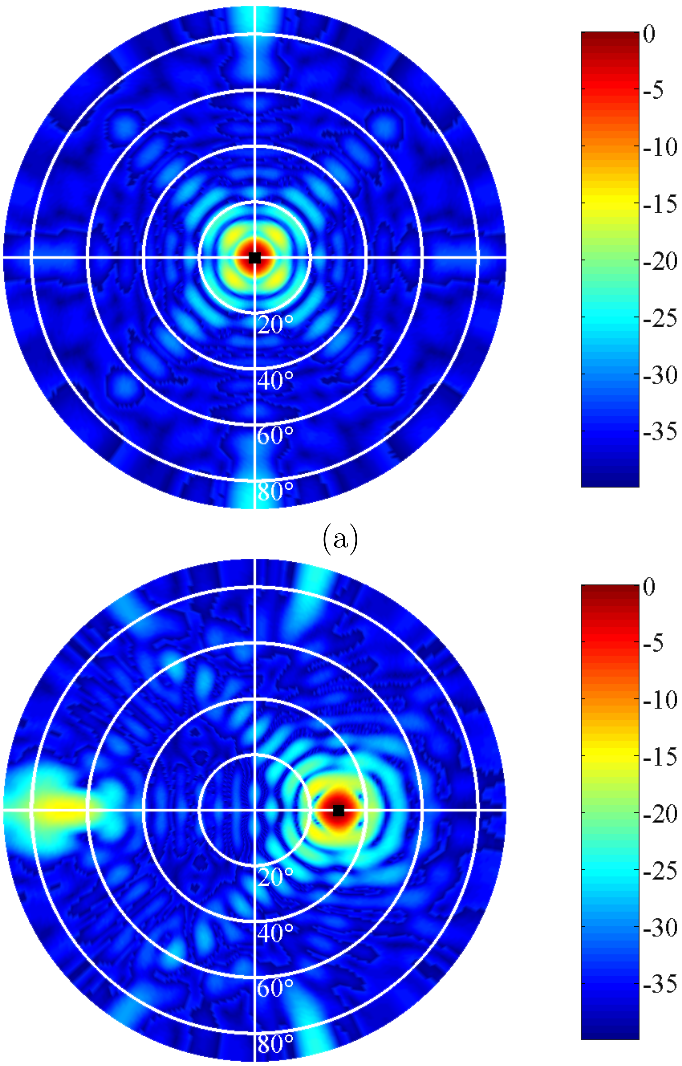

(a)

(b)

Figure 4.20: Image at the focal surface for the plane wave coming from $\theta = 0^\circ$ (a) and $\theta = 30^\circ$ (b).

presented in Section 3.2.6 resulting in almost 7 dB decrease in the spill-over loss.

4.6 Conclusions

The second lens has full three-dimensional scanning capabilities. The frequency bandwidth, which is still in the X-band, is significantly increased. This is achieved using the stacked patch antenna design for the unit cell, with a bandwidth of $9\,\%$ instead of $1.5\,\%$ bandwidth of a regular patch antenna. One of the main concerns in the new design was the loss in the spatial combining network. The total loss is predominantly attributed to the spill-over loss. The new lens array has $F/D = 1$, octagonal shape and 165 elements, compared to $F/D = 1.5$, cylindrical shape and 45 elements in the first design. That provides not only lower spill-over loss but a significant increase in the directivity as well, which combined result in more than 12 dB increase in the gain of the lens array. Side lobe levels and beam uniformity as functions of the scan angle are also improved.

Chapter 5

Comparison

5.1 Constrained Lens Array vs. Dielectric Lens

Like the dielectric lens, the CLA also has the ability to focus electromagnetic energy. At microwave frequencies, however, the free space wavelength is tens of thousands of times bigger compared to those in the optical region. As a result, lenses used at the millimeter-wave and especially at the microwave frequencies are small compared to optical lenses when measured in free space wavelengths. Their size and weight can also be a problem in some applications. Losses in dielectric lens materials have been lowered by use of some new materials. Reflection loss is also a problem in dielectric lenses. It can be controlled using anti-reflection coating and stepping, but at the expense of frequency bandwidth. Dielectric lenses are sensitive to environmental and mechanical stresses, which can also limit their applicability.

Unlike dielectric lenses, the CLAs discussed in this work have planar front and back faces, which make them simple to manufacture and cost effective. The active components can be incorporated at each element of the lens array. They can be used for wide scan angles and the polarization between the feed and the non-feed side of the array can be used as an additional design parameter. The polarization isolation between two sides of a CLA can be used as described in Chapter 3. The transmission lines that connect antenna elements are true time delay lines, which provide high frequency bandwidth.

In the analysis of the optical and millimeter-wave lenses, the Gaussian beam approach can be applied [46, 47]. Waves whose wavefront normals make small angles with the optical axis are called paraxial waves. The complex amplitude of a paraxial wave as a function of a position vector $\mathbf{r}$ is

$$U\left(\mathbf{r}\right) = A\left(\mathbf{r}\right) e^{(-jkz)} \tag{5.1}$$

where $A(\mathbf{r})$ is a complex envelope, $k = 2\pi/\lambda$ is the wave number, and z is the axial distance. The variation of the complex envelope $A(\mathbf{r})$ is assumed to be small over a distance comparable to λ. For the complex amplitude to satisfy the Helmholtz equation

$$\nabla^2 U + k^2 U = 0 \tag{5.2}$$

the complex envelope $A(\mathbf{r})$ has to satisfy the paraxial Helmholtz equation

$$\nabla_T^2 A - j2k\frac{\partial A}{\partial z} = 0 \tag{5.3}$$

where $\nabla_T^2 = \partial^2/\partial x^2 + \partial^2/\partial y^2$ is the transverse Laplacian operator. Solutions to the paraxial Helmnoltz equation are Gaussian beam modes. Only the main characteristics of the fundamental Gaussian beam mode and its propagation through a thin lens are given here. A Gaussian beam is expressed by its complex amplitude $U(\mathbf{r})$

$$U(\mathbf{r}) = A_0 \frac{W_0}{W(z)} e^{-\frac{\rho^2}{W^2(z)}} e^{-jkz - jk\frac{\rho^2}{2R(z)} + j\zeta(z)} \tag{5.4}$$

where z and $\rho^2 = (x^2 + y^2)$ are the axial and radial distances, A_0 is a constant, and $W(z)$ (the beam radius), $R(z)$ (the wavefront radius of curvature), $\zeta(z)$ (the phase retardation), and W_0 (the waist radius) are the beam parameters defined as:

$$W(z) = W_0 \left[1 + \left(\frac{z}{z_0}\right)^2\right]^{1/2} \tag{5.5}$$

$$R(z) = z\left[1 + \left(\frac{z_0}{z}\right)^2\right] \tag{5.6}$$

$$\zeta(z) = tan^{-1}\frac{z}{z_0} \tag{5.7}$$

$$W_0 = \left(\frac{\lambda z_0}{\pi}\right)^{1/2} \tag{5.8}$$

The intensity $I(r) = |U(z)|^2$ is a function of the axial and radial distances z and ρ

$$I(\rho, z) = I_0 \left[\frac{W_0}{W(z)}\right]^2 e^{-\frac{2\rho^2}{W^2(z)}} \tag{5.9}$$

where $I_0 = |A_0|^2$. At each value z the intensity is a Gaussian function of the radial distance ρ. This is why the wave is called a Gaussian beam.

On the beam axis ($\rho = 0$) the intensity becomes

$$I\left(0, z\right) = I_0 \left[\frac{W_0}{W\left(z\right)}\right]^2 = \frac{I_0}{1 + \left(z/z_0\right)^2} \tag{5.10}$$

It has its maximum value I_0 at $z = 0$ and drops gradually with increasing z. It reaches its half-peak value at $z = \pm z_0$ as shown in Figure 5.1(a). For a fixed transverse plane, the beam intensity has the maximum on the optical axis. It drops monotonically with increasing radial distance ρ. At $\rho = W(z)$ the intensity is $1/e^2$ of the maximal value. This distance is called the *beam radius* or the *beam width* (Figure 5.1(b)) and 86 % of the total power is carried within the circle defined by that radius. The minimum value W_0 is

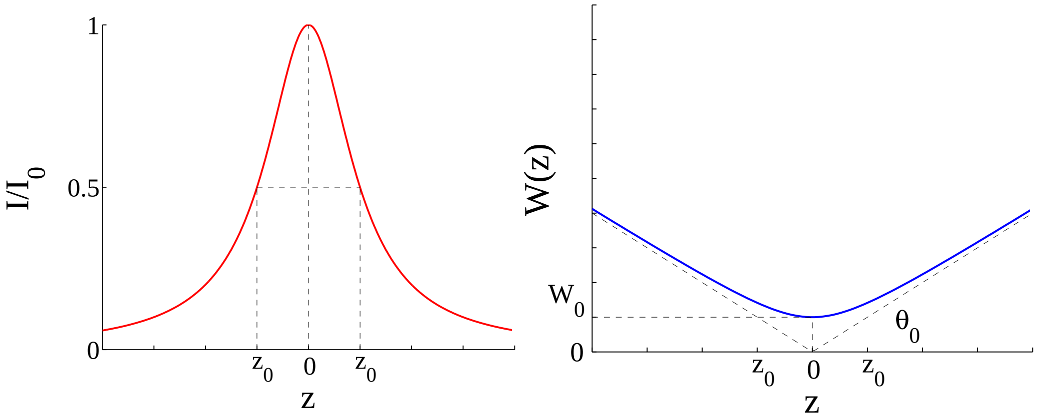

(a)

(b)

Figure 5.1: Relative intensity and beam radius of the Gaussian beam calculated at points on the optical axis as a function of the distance from the beam waist.

located in the plane $z = 0$. This plane is called the *beam waist* and the beam radius W_0 is called the *waist radius*. The diameter of the beam at the beam waist is the *spot size*. The angle θ_0 in Figure 5.1(b), called the *divergence angle* is defined as:

$$\theta_0 = \frac{\lambda}{\pi W_0} \tag{5.11}$$

At points in the beam waist and close to the optical axis the intensity is approximately constant, and the phase is approximately kz. The Gaussian beam at these points can be approximated as a plane wave. One of the very important characteristics of the Gaussian beam is that it remains a Gaussian beam after transmission through circularly symmetrical optical components aligned with the beam axis, as long as the paraxial nature of the wave is satisfied. Transmission of the Gaussian beam through a thin lens is presented in Figure 5.2

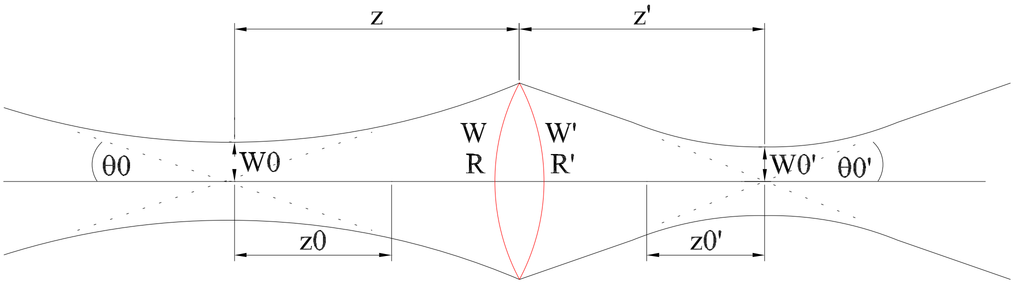

Figure 5.2: Transmission of a Gaussian beam through a thin lens.

The transmitted wave has the beam parameters which are given as:

$$W_0' = MW_0 \tag{5.12}$$

$$(z' - f) = M^2 (z - f) \tag{5.13}$$

$$2z_0' = M^2 (2z_0) \tag{5.14}$$

$$2\theta_0' = \frac{2\theta_0}{M} \tag{5.15}$$

where the the magnification factor$M$ is

$$M = \frac{M_r}{\left(1 + r^2\right)^{1/2}} \tag{5.16}$$

$$r = \frac{z_0}{z - f} \tag{5.17}$$

$$M_r = \left| \frac{f}{z - f} \right| \tag{5.18}$$

In order to compare the Gaussian beam system with the CLA a one-degree of freedom 99 × 99 element array with $\lambda/2 \times \lambda/2$ unit cell size and F/D=1 is simulated and compared with an equivalent thin lens. The lens is positioned very close to the waist of an incident Gaussian beam with a spot size that matches the size of the lens. This configuration results in a transmitted beam with the waist located at the focal distance F. The beam radius W as a function of the distance from the focal point and the relative intensity I/I_0

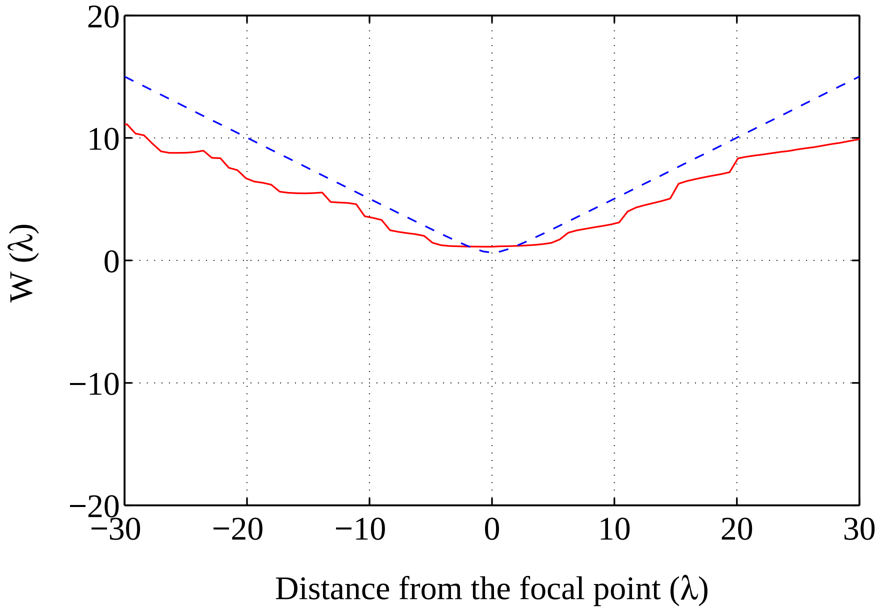

Figure 5.3: Calculated beam radius for a 99×99 element CLA with $\lambda/2 \times \lambda/2$ unit cell size and F/D=1 as a function of distance from the focal point (red solid line) compared with calculated beam radius of a transmitted Gaussian beam through an equivalent thin lens (blue dashed line).

as a function of the radial distance ρ at the beam waist and the distance from the focal point are calculated for the CLA. The results are compared with the Gaussian beam transmitted through an equivalent thin lens. The results are presented in Figure 5.3, Figure 5.4 and Figure 5.5. The calculated waist radius of the transmitted beam for the thin lens is W_0=0.64 λ (minimum of the blue dashed line in Figure 5.3) and for the CLA is W_0=1.125 λ (minimum of the red solid line line in (Figure 5.3) The Gaussian beam solutions can only be used for well-collimated beams, as discussed above. The criterion $W_0/\lambda \geq 0.9$ is accepted in several treatments of Gaussian beams to define the

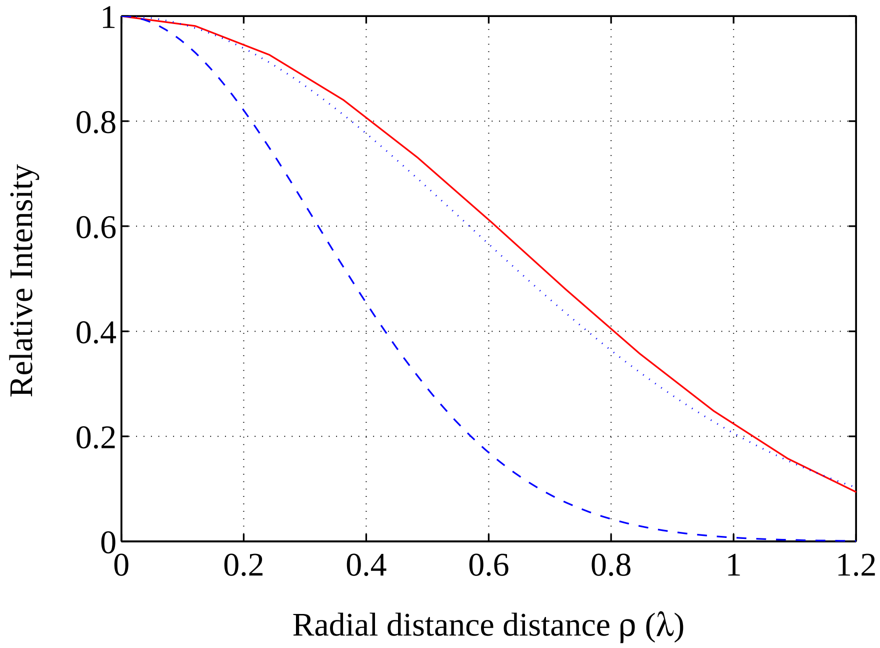

Figure 5.4: Calculated relative intensity for a 99 × 99 element CLA with $\lambda/2 \times \lambda/2$ unit cell size and F/D=1 for for the points in the beam waist as a function of the radial distance (red solid line) compared with calculated relative intensity of a transmitted Gaussian beam defined with the waist radius W_0=0.64 λ (blue dashed line) and W_0=1.125 λ (blue dotted line) beam through an equivalent thin lens.

range of applicability of the paraxial approximation [47]. For $0.5 \leq W_0/\lambda \leq 0.9$ the paraxial and exact solutions differ and certain corrections should be applied [48]). The relative intensity is calculated at the beam waist as a function of the radial distance ρ for the CLA and is presented with the red solid line in Figure 5.4. The result is compared with the transmitted Gaussian beam defined with the waist radius W_0=0.64 λ (blue dashed line) and W_0=1.125 λ (blue dotted line). The relative intensity is also calculated for the points

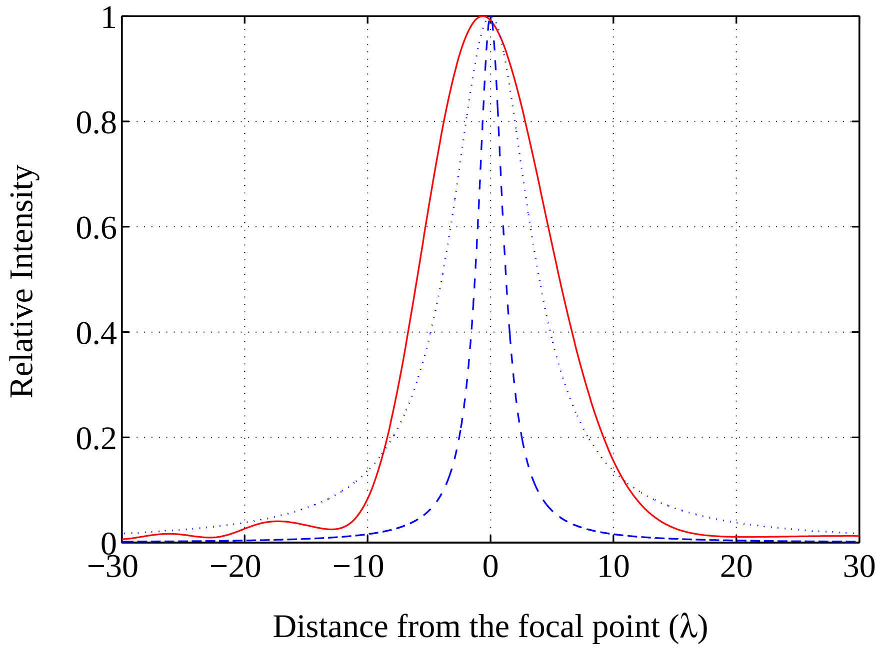

Figure 5.5: Calculated relative intensity for a 99×99 element CLA with $\lambda/2\times\lambda/2$ unit cell size and F/D=1 as a function of distance from the focal point (red solid line) compared with calculated relative intensity of a transmitted Gaussian beam defined with the waist radius W_0=0.64 λ (blue dashed line) and W_0=1.125 λ (blue dotted line)beam through an equivalent thin lens.

on the optical axis as a function of the distance from the focal point (Figure 5.5). The results for the CLA (red solid line) are again compared with the two Gaussian beams with the waist radii W_0=0.64 λ (blue dashed line) and W_0=1.125 λ (blue dotted line). The relative intensity calculated for the CLA in Figure 5.5 reaches its peak at a distance shorter than the focal distance F and is broader compared to the transmitted Gaussian beam calculated for both values of the waist radius. In order to explain this and to illustrate some other characteristics of the CLA, several examples follow. Three one-degree-of-freedom CLAs with F/D of 1, 1.5 and 2 are analyzed. All of them have 15×15 antenna elements and $\lambda/2 \times \lambda/2$ unit cell size. The antenna elements are assumed to be omni-directional. The plane wave is incident at 0° angle, and the power is calculated at the optical axis after the CLA at a distance l (from $l = 0.5\,D$ to $l = 5\,D$). The results are normalized to the maximum power received and presented in Figure 5.6(a). Since the size of the arrays is kept constant ($D = const$) and F/D is set to be 1, 1.5 and 2 the focal points and therefore the peak power in these three cases should be located at $F = D$, $F = 1.5\,D$ and $F = 2\,D$. Figure 5.6(a), however, shows that the peak power is shifted closer to the lens array in all three cases. This behavior is confirmed with the measured results. The reason for this is the path loss. The power density at a distance r from the radiating element is proportional to $1/r^2$. If the path loss is neglected in the calculations, the peak power would be located at the designed focal point as shown in Figure 5.6(b). The shape of the curves presented in Figure 5.6 is asymmetrical. In Figure 5.6(b) the path loss is excluded in the calculations and the antennas are assumed to be omnidirectional. The only effect that determines the shape of these curves is the path length error. At the focal points, signals from all the elements in the array will combine coherently. At any other point on the optical axis there will be some phase difference between the signals coming from different antenna elements. To get a measure of these errors the root-mean-square path length error (RMS-PLE) is calculated as a function of distance from

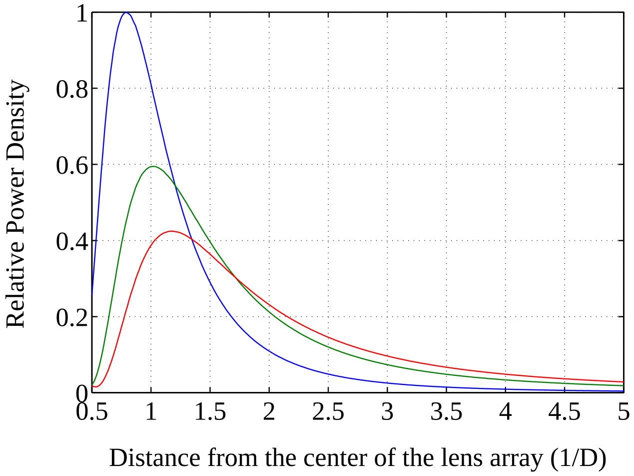

(a)

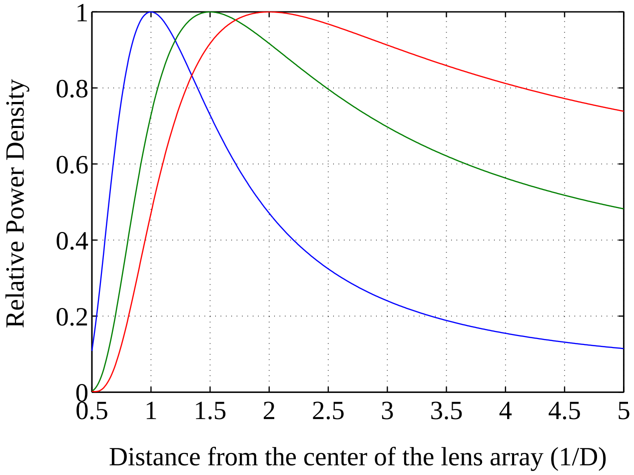

(b)

Figure 5.6: Calculated relative power density on the optical axis as a function of the distance (normalized to the lens diameter D) from the center of the lens for three one-degree-of-freedom lens arrays. The lenses have 15×15 antenna elements and $\lambda/2 \times \lambda/2$ unit cell size with F/D of 1, 1.5 and 2. Calculations are done taking into account the path loss (a) and without the path loss (b).

the center of the array. The result is given in Figure 5.7 for the three lens arrays. It can be seen that the RMS-PLE has zero values at the focal points.

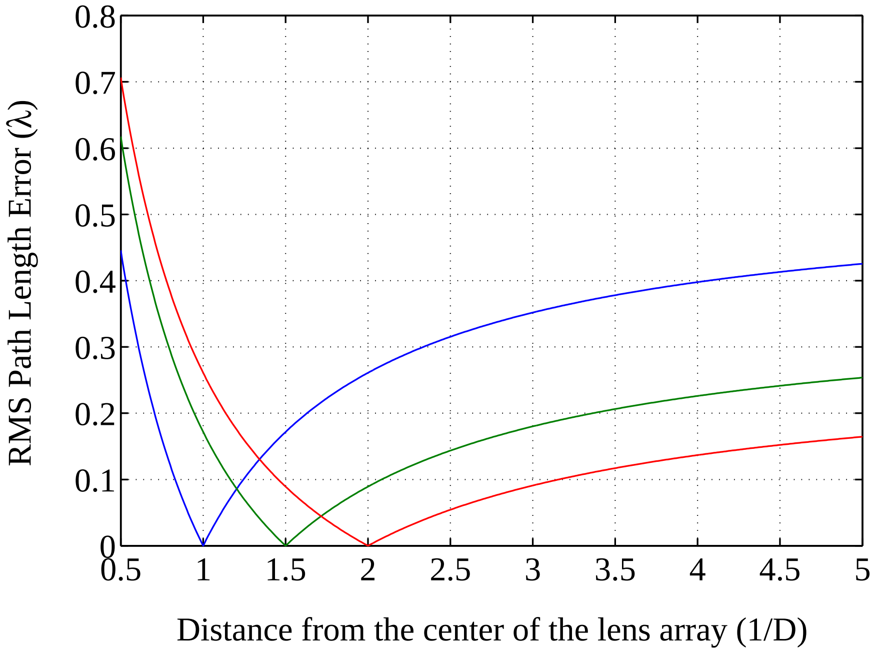

Figure 5.7: Calculated root-mean square path length error as a function of the distance (normalized to the lens diameter D) from the center of the lens for three one-degree of freedom lens arrays. The lenses have 15×15 antenna elements and $\lambda/2 \times \lambda/2$ unit cell size with F/D of 1, 1.5 and 2. Calculations are done taking into account the path loss (a) and without the path loss (b).

For distances closer to the lens array the phase errors increase much faster compared to the region away from the lens array and the focal point. The reason for this is geometrical.

5.2 Constrained Lens Array vs. Phased Array

Phased arrays use corporate combining networks instead of a spatial combining network (Figure: 5.8). The corporate combining networks consist of

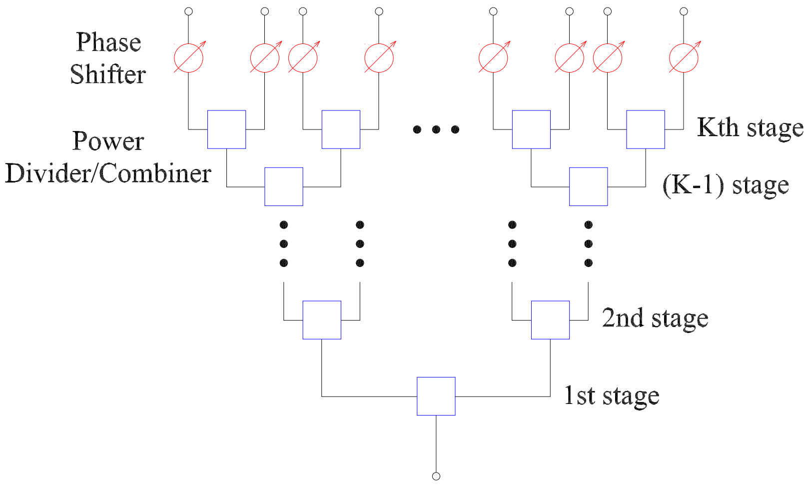

Figure 5.8: Block diagram of a corporate combining network for phased arrays.

transmission lines, phase shifters, and power dividers/combiners. The amplitude and phase excitations of antenna elements can be controlled with high accuracy in phased arrays. This can be used to minimize the side-lobe levels and to maintain the beam uniformity at different scan angles. The main disadvantage of the corporate combining networks is the complexity that increases with the number of elements N. The phase shifters at microwave and especially millimeter-wave frequencies are expensive and lossy. Their number is directly related to the the number of antenna elements, and for large arrays the cost of the system becomes extremely high. Another disadvantage in using the phase shifters is their limited frequency bandwidth.

Phase shifters are not used in the CLA. The true time delay lines are incorporated in the lens array and are not frequency limited. The complexity and cost of the system scales favorable with the size of the array. Spill-over loss, amplitude non-uniformity and path length errors are the problems associated with spatial combining networks. However, it is possible to minimize these problems as was discussed in Chapter 4.

The loss mechanisms are also different in constrained lens arrays and phased arrays. The main loss mechanism in CLAs is the spill-over loss. For fixed F/D the total loss in the system will stay constant with the increase in the number of elements. The loss in the corporate combining network on the other side increases when the number of elements increases as

$$L = \varepsilon_{div}^{K} + \varepsilon_{tl}^{K+1} + \varepsilon_{ph} \tag{5.19}$$

where $K = log_2(N)$ is the number of stages in the array with N elements, ε_{div} is the insertion loss in a power combiner/divider, ε_{tl} is the loss in the transmission line, and ε_{ph} is the loss in the phase shifter. The total loss in the corporate combining network is calculated as a function of the number of elements when the loss in the dividers and transmission lines ε_{div} and ε_{tl} is varied from 0.5 dB to 1 dB in 0.1 dB steps (Figure 5.9). The loss in the

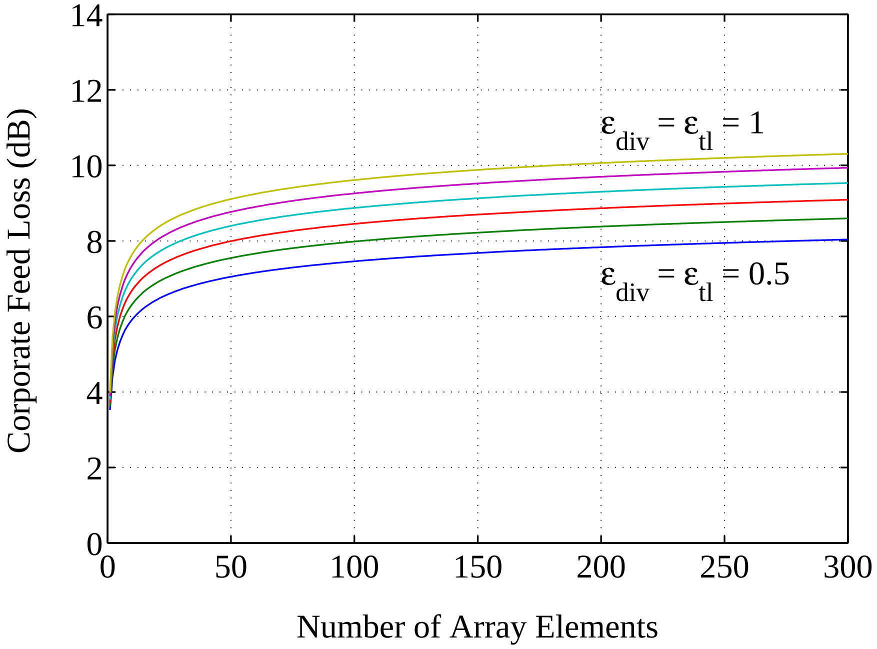

Figure 5.9: Loss in a corporate combining network as a function of the number of elements N and the loss in the power dividers/combiners ε_{div} and transmission lines ε_{tl} varied from 0.5 dB to 1 dB as a parameter.

phase shifters is set to be 2 dB. Insertion loss for guided wave structures is dependent on frequency and grows approximately with $\sqrt{f}$ [49]. The loss in phase shifters becomes extremely high at millimeter-wave frequencies. At Ka band (26.5-40) GHz for example a phase shifter alone can add up to 15 dB of loss.

In summary, phased arrays have advantages over CLAs for a small number of elements. However, in large arrays CLAs are better in terms of the complexity, cost, weight, and loss in the system.

Chapter 6

Applications

6.1 Introduction

Three different application of the CLAs are demonstrated:

- Characterization of CLA in a multipath environment for mobile communications.
- Design of CLA for fixed-formation satellite communications with a new feature of amplitude controlled continuous small-angle scanning.
- System integration with an adaptive optical processor for jammer/interference extraction.

6.2 Constrained Lens Array for Mobile Communication Systems

Constrained lens arrays have several important characteristics, which make them attractive for a wide range of applications in wireless communication systems. Beam forming capability is one of them. It is shown in this work that this type of system can be used for wide scan range ($\pm 45^\circ$) with moderate degradations in the radiation performance. The losses in the spatial combining network, as well as the side-lobe levels and the beam uniformity can be optimized if the lens array and the feed antennas are treated as a system. The lenses presented in this work are capable of full three-dimensional scanning. In wireless communication systems it is very important to be able to set the orientation of beams in the most suitable way for the given indoor or outdoor terrain configuration. In the CLAs, the number of beams and their orientation depend on the number of feed antennas and their positions at the focal surface, and can therefore easily be adjusted. This flexibility is an important factor in lowering the cost of the wireless communication system since the same lens array can be used in different applications. Another important parameter that determines the cost of the system is the manufacturing cost. Since lens arrays have flat surfaces they can be manufactured using the facilities and techniques for regular printed circuit boards. The mass production of these systems would obviously lower the cost even further.

Diversity techniques in wireless communications were a point of interest for a long time [1, 2, 3, 4]. Due to a constant increase in the number of users of the limited RF spectrum these techniques have become a necessity in modern communication systems. The dual-polarized lens arrays presented in this work exploit two diversity types, the first one being angular diversity.

Fading due to multipath can cause a severe degradation in the quality of service in a wireless communication system. Multipath is caused by reflections from objects like buildings, vehicles, ground etc. These reflections allow a signal that originates from one point to reach its destination not only through a direct path (which sometimes does not even exist) but through several different paths. At the point of reception signals can combine constructively or destructively depending on their relative phases.

Based on the characteristics of the CLA one can expect to see improvements in a link in a multipath fading environment when the lens is used at the front end. In order to test this, an experiment is performed with a CLA placed in a simple controllable multipath environment consisting of a single metal reflector in an anechoic chamber, as shown schematically in Figure 6.1. The CLA discussed in Chapter 3 is used in the experiment. The reflector is 15×15 free-space wavelengths large and is translated in the x direction over three free-space wavelengths. The reflector is positioned so that at x=0, the reflected wave from the transmitting horn falls into the second null of the lens antenna pattern for a receiver on the optical axis (receiver A in Figure 6.1), consistent with the radiation pattern of the CLA. In the first set of measure-

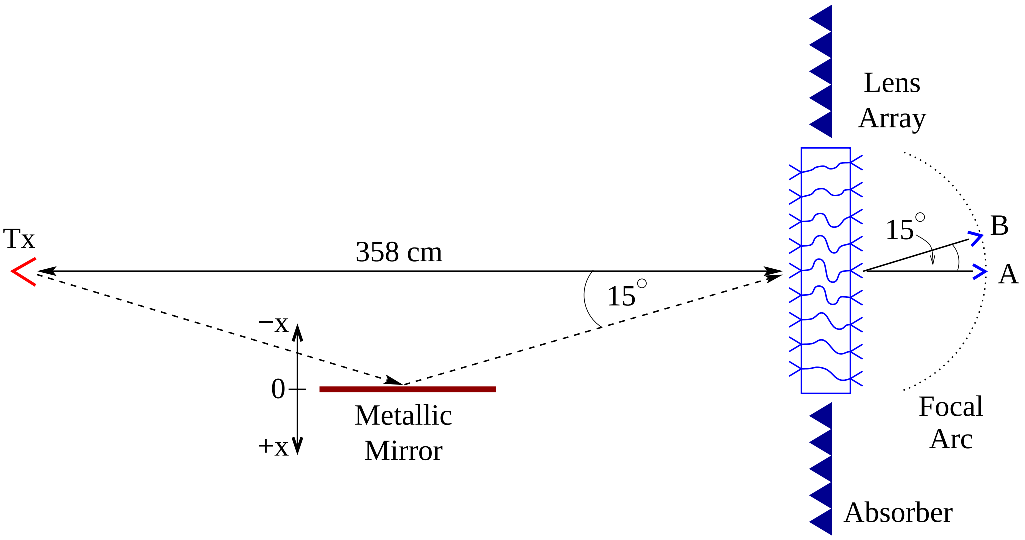

Figure 6.1: Multipath measurement setup with a single 15x15 wavelength reflector which is translated by 3 wavelengths in the x direction. The x=0 reference level corresponds to the second null in the lens radiation pattern

ments, Figure 6.2 and Figure 6.3, the received power in a line-of-sight link between the transmitting horn antenna and the receiving patch with no lens array present was measured without the presence of the mirror, and then as the mirror was translated in the x direction. Another set of measurements was performed with the CLA used instead of the patch antenna as a receiver (Figure 6.4 and Figure 6.5). The power at the input of the transmitting horn is 500 mW. The straight horizontal lines in Figures 6.2 to 6.5 show the measured power levels for the direct link only without the reflector present. When the reflector is added, there is a standing wave behavior typical of a multipath environment. When the lens array is placed in front of the receiv-

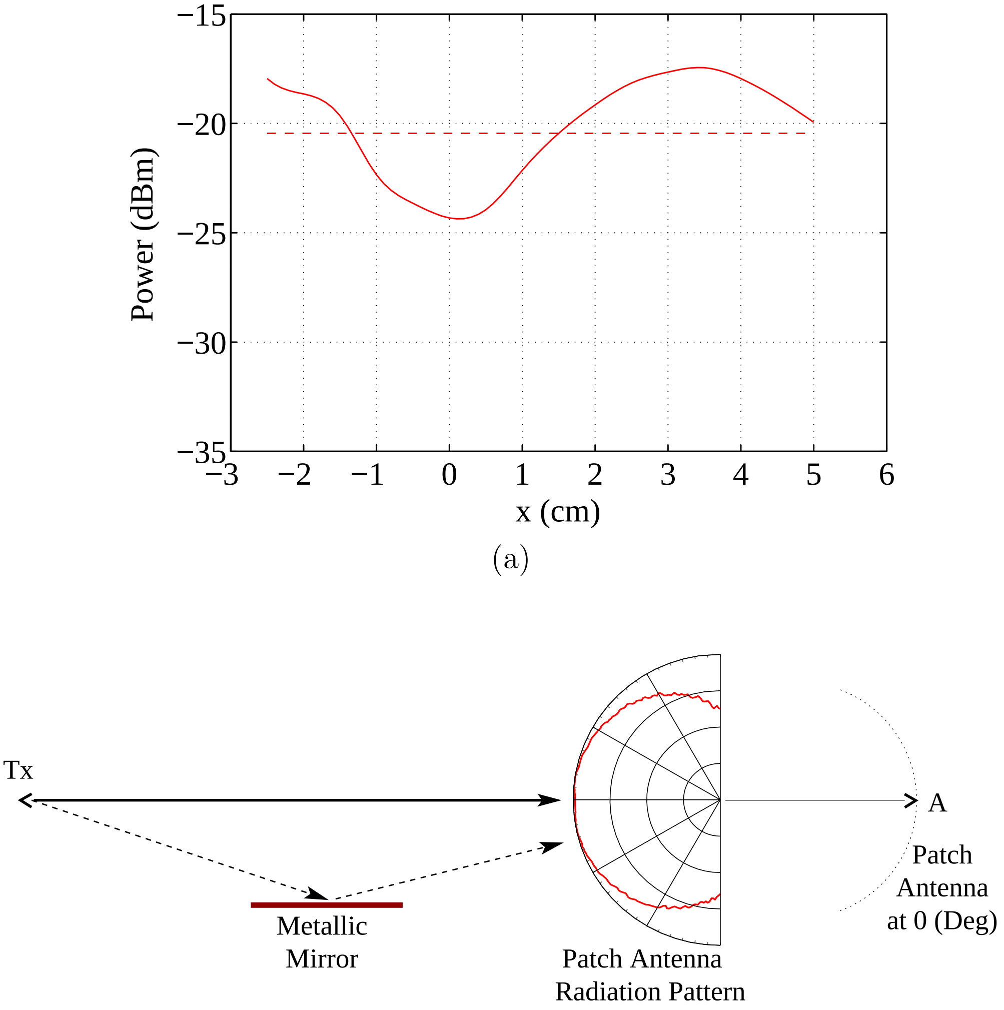

(a)

(b)

Figure 6.2: Measured received co-polarized power in the presence of a reflector without the lens in the link (a). The receiver is positioned for a beam at 0°. The straight dashed line shows the reference power level received with no reflector (no multipath) in the link. Measurement setup with the antenna radiation pattern (b).

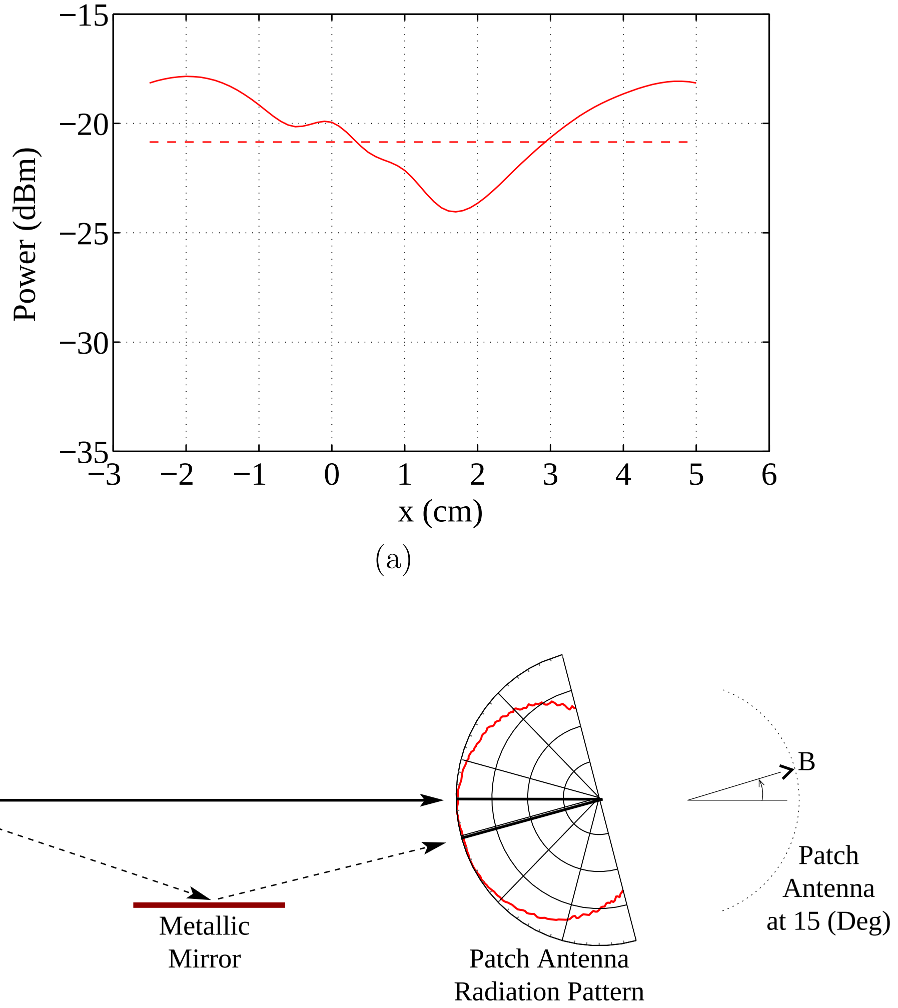

(a)

(b)

Figure 6.3: Measured received co-polarized power in the presence of a reflector without the lens in the link (a). The receiver is positioned for a beam at 15°. The straight dashed line shows the reference power level received with no reflector (no multipath) in the link. Measurement setup with the antenna radiation pattern (b).

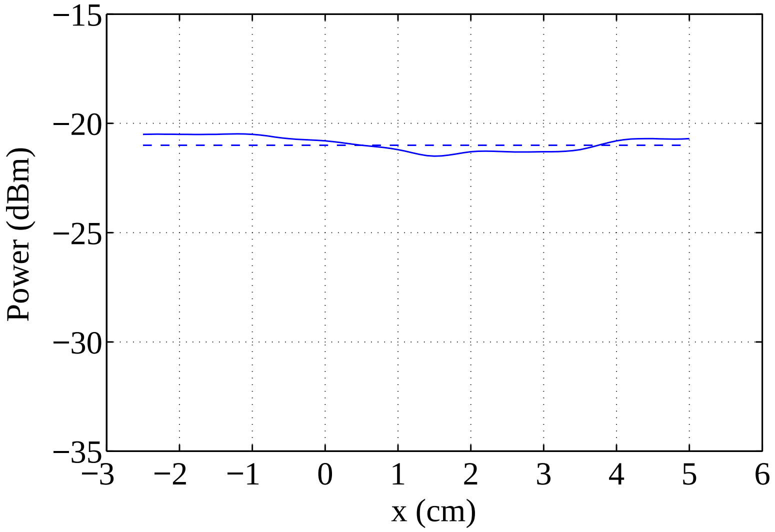

(a)

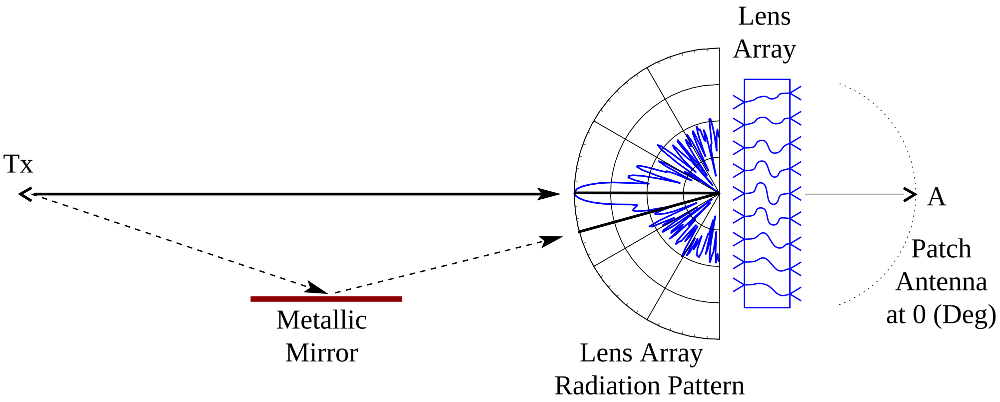

(b)

Figure 6.4: Measured received co-polarized power in the presence of a reflector with lens in link (a). The receiver is positioned for a beam at 0°. The straight dashed line shows the reference power level received with no reflector (no multipath) in the link. Measurement setup with the lens array radiation pattern (b).

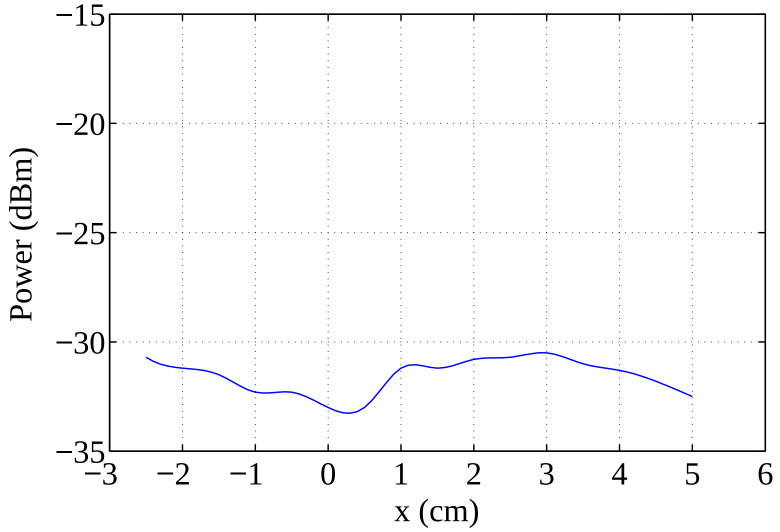

(a)

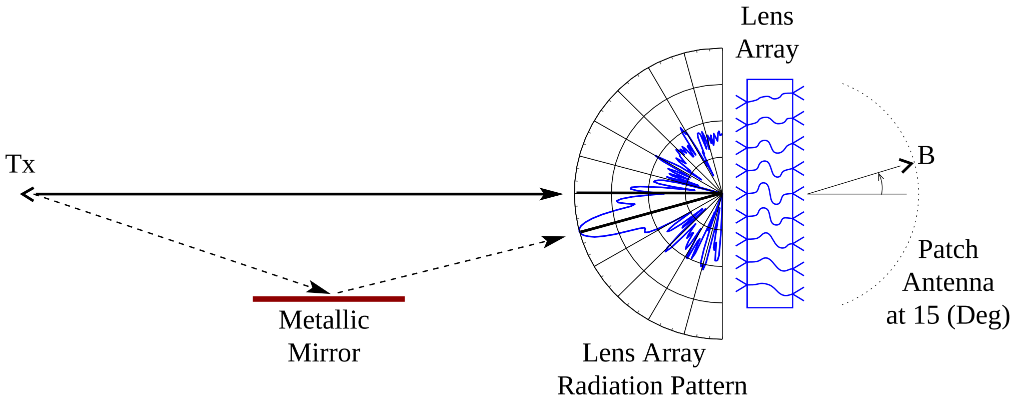

(b)

Figure 6.5: Measured received co-polarized power in the presence of a reflector with the lens in the link (a). The receiver is positioned for a beam at 15°. The reference power level received with no reflector (no multipath) in the link was at -53 dBm. Measurement setup with the lens array radiation pattern (b).

ing antenna, the multipath peak-to-null ratio is significantly reduced, partly due to the gain of the array and partly due to the built-in angle diversity. When the receiver is positioned at point B on the focal arc corresponding to a beam at $-15°$, the reference level of the received signal without the mirror is -53 dBm (not shown in Figure 6.5(a)), which is 32 dB below the -21 dBm reference level measured with the feed on the optical axis. This agrees well with the second null at 0° in the radiation pattern in Figure 6.5(b), which is about 30 dB below the main beam. When the metallic mirror is placed in the experiment, the level of the signal is on average raised by 20 dB (blue solid line in Figure 6.5(a)) compared to -53 dBm reference power level measured without the mirror . Therefore, the reflected multipath signal is spatially separated from the direct signal, and the two are received separately and can subsequently be combined to obtain an increased signal level.

The second diversity technique used in the systems that are discussed here is the polarization diversity. The power transmitted in one polarization will change its polarization state after it passes through an RF channel. If a vertically polarized signal is transmitted, some of the power will be transfered in the horizontal polarization by the time it reaches the receiver. A system that is able to receive both orthogonal polarizations can deal with the problems of polarization perturbations caused by the RF channel. The systems that do not use polarization diversity can in a worst-case scenario suffer from a total loss of signal.

Lens arrays that can receive and transmit two linear orthogonal polarizations can be used with arbitrarily polarized signals. The only element in the system that would have to be changed is the feed antenna. That is another characteristic that makes these lens arrays versatile.

6.3 Constrained Lens Array for Fixed-Formation Satellite Communications

Satellite communications is another area that requires multibeam arrays. A planar constrained millimeter-wave lens is proposed for use as a multibeam Ka-band array antenna for fixed-formation satellites [50]. The lens radiates two Ka-band frequencies with two orthogonal linear polarizations. The application requires several simultaneous beams at different angles, each carrying two frequencies with different polarizations. The angle of each beam can be fine-tuned with a small scanning angle around the fixed positions. This is achieved with an amplitude control (in place of phase control) of each of the two feed antenna elements providing a small scan angle of about $5°$. The schematic of the system is presented in Figure 6.6. Instead of only one antenna, a two-element antenna array with amplitude control is used as a feed. The spacing between the elements is λ_0. Small angle continuous scanning is achieved by changing the relative amplitude levels between the two elements. This is demonstrated for the case of a (15×15)-element CLA with $(\lambda_0/2 \times \lambda_0/2)$ unit cell size. Power delivered to (or received at) the two antenna elements is controlled by the amplitude coefficients A_1 and A_2.

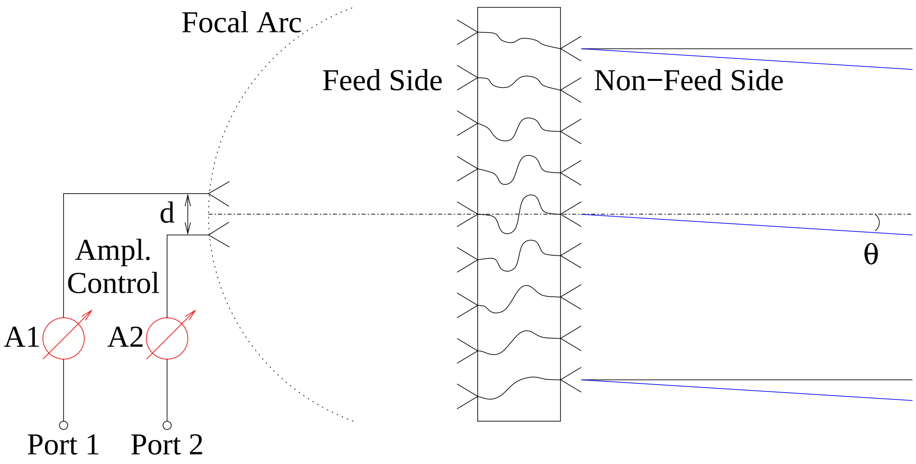

Figure 6.6: Schematic of a CLA with amplitude controlled small angle scanning.

Variable attenuators or amplifiers with gain control can be used to change the relative power between the antenna elements. In this example A_1 is set to 1 and A_2 is changed from 0 (max. attenuation) to 1 (no attenuation). The position of the main beam as a function of the ratio A_2/A_1 is calculated and presented in Figure 6.7. The beam is steered more than 2.5° off the fixed position, in one direction. When A_1 is changed instead of A_2 the beam is moved in the opposite direction. This gives a total steering of $\pm 2.5°$. Broadening of the main beam and an increase in side-lobe level are disadvantages of the steering technique presented here. This experiment with the feed antenna consisted of just two elements is a demonstration of the principle that

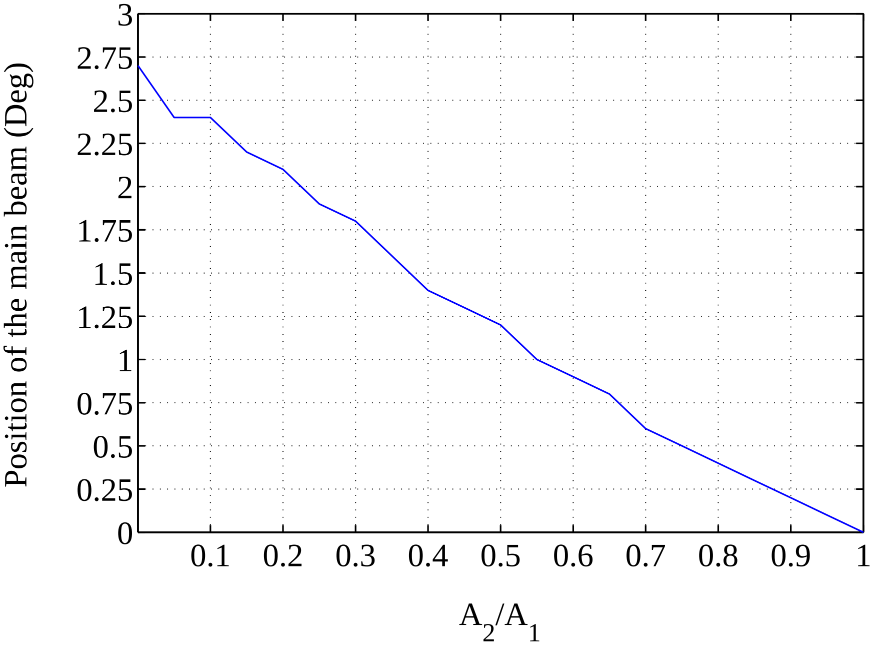

Figure 6.7: Calculated position of the main beam as a function of the ratio A_2/A_1, for a (15×15)-element CLA with $(\lambda_0/2 \times \lambda_0/2)$ unit cell size

can be used for small angle steering. A more elaborate design should be used to overcome the problems stated above.

6.4 Constrained Lens Array in adaptive processing system

A system that performs optical processing of the RF signals with a CLA used at the RF front end is presented [51]. The purpose of this system is to adaptively extract the principal component of the received signal space that is the strongest first-order independent temporal component of the ensemble of received signals. The main function of the CLA is to increase the dynamic range of the system. It does so using its beam forming capability. The signals received at the feed points along the focal arc are already partially separated. Some amount of cross-talk is still present, which depends on the radiation pattern of the CLA and the relative positions of the feed antennas. The optical processor is therefore used to further separate the signals. Principal component analysis is a limiting case of the more general independent com-

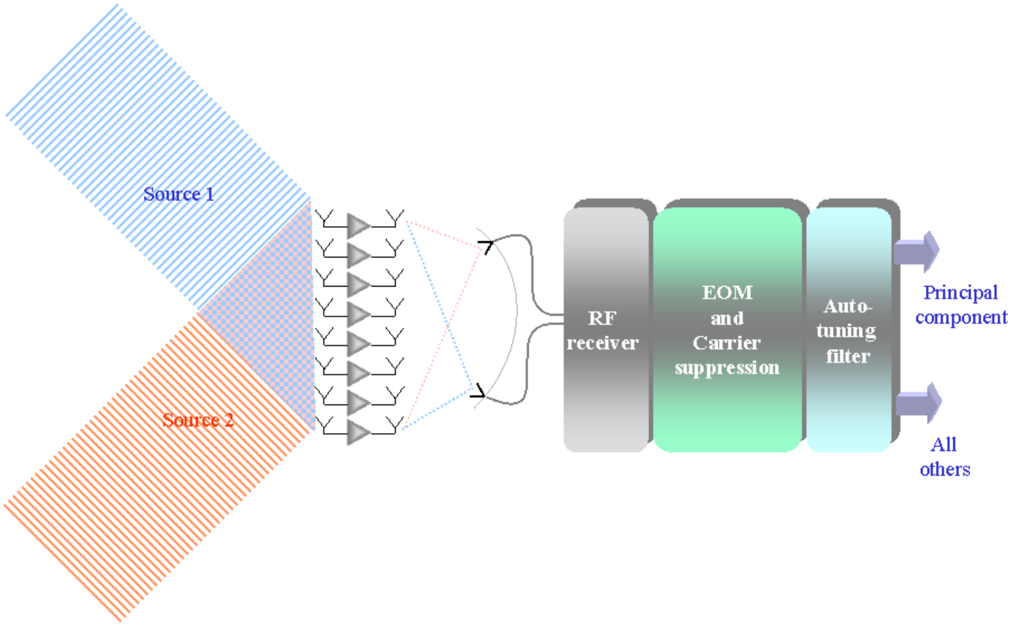

Figure 6.8: Block diagram of the optically smart antenna array with two sources in the far field. The active receivers are positioned on the focal arc of the discrete lens antenna. The IF signals are then imposed onto the optical beam and processed by the adaptive optical circuit.

ponent analysis (ICA) [52]. ICA techniques have been successfully used in low-bandwidth applications such as speech processing. In RF communications and other high-bandwidth real-time signal processing applications these techniques cannot be used with the digital signal processing available today. A system that will perform ICA on high-bandwidth RF signals using the optical circuitry is the subject of the current and future work at the University of Colorado [53]. The CLA presented in Chapter 4 can be efficiently used in such a case due to its high-bandwidth, good radiation properties, and wide scan range.

A block diagram of the system is given in Figure 6.8. There are three main parts in the system presented in Figure 6.8:

1) the microwave front end

2) the electrooptic modulation and carrier suppression stage

3) the optical processing (auto-tuning filter) stage.

6.4.1 Microwave Front End

The CLA used in this system has 30 antenna elements in a triangular lattice. The unit cell size is $0.65\,\lambda \times 0.65\,\lambda$ and $F/D = 0.6$ [33]. The antenna elements are rectangular patch antennas resonant at 10 GHz with 1.5 % frequency bandwidth. The system has two RF receivers. The block diagram of the receiver is presented in Figure 6.9. The signal received at a linearly polarized patch antenna positioned at the focal arc is amplified in a low-noise amplifier (LNA) for optimal noise figure. The United Monolithic Semicon-

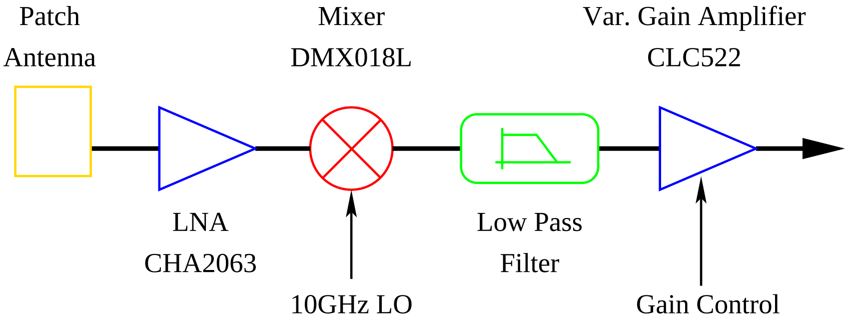

Figure 6.9: Block diagram of the receiver positioned on the focal surface of the lens array.

ductor CHA2063 LNA is used. It has a 7-13 GHz frequency bandwidth, 16 dB gain, and 2 dB noise figure. The 1-dB compression point of the amplifier is 10 dBm, with low dc power consumption (40 mA at 5 V). A Miteq DMX0418L mixer downconverter follows the LNA. The IF amplifiers are CLC522 National Semiconductors wideband variable gain amplifiers. They provide more than 40 dB gain control through a single high impedance voltage input. The ability to control the levels of the signals at the input of the optical processor is important for proper optical processing. The photograph of a two-channel receiver unit is presented in Figure 6.10. An integrated version of the receiver manufactured on an RT/Duroid substrate with a high relative permeability of ϵ_r=10.5 and 0.508 mm thickness is used in the final design of the system.

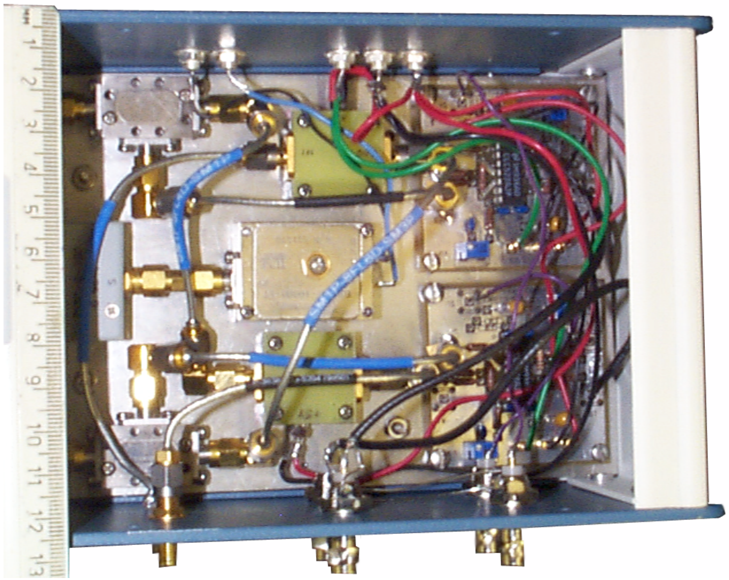

Figure 6.10: Photograph of the two-channel RF receiver.

6.4.2 Carrier Suppression

The IF signals obtained after downconversion modulate an optical carrier having a wavelength of 532 nm in an electrooptic phase modulator. The optical carrier is common to all the signal channels and therefore introduces an unwanted correlation. In order for the auto-tuning filter to operate properly this correlation has to be eliminated. This is performed in the carrier suppression unit. There are several methods that can be used for carrier suppression. Some of them are based on linear [54, 55] and some on nonlinear optical techniques [56, 57]. Technique used in this system is based on a two-beam coupling within a barium titanate photorefractive crystal [58, 59, 60]. A complete treatment of photorefractive carrier suppression principles is given in [61]. Only the fundamentals of operation and the results relevant to the system are presented here. The beam-coupling interaction takes place between two beams coming from the same laser, one of which has been modulated with the IF signals by the EOM as illustrated in Figure 6.11. As a result of the interaction the modulated beam is transmitted from the crystal with the optical carrier largely suppressed, while the other beam has increased carrier power and also a portion of the IF signal power. As suggested by Figure 6.11, carrier suppression comes at the cost of some signal power lost to the plus

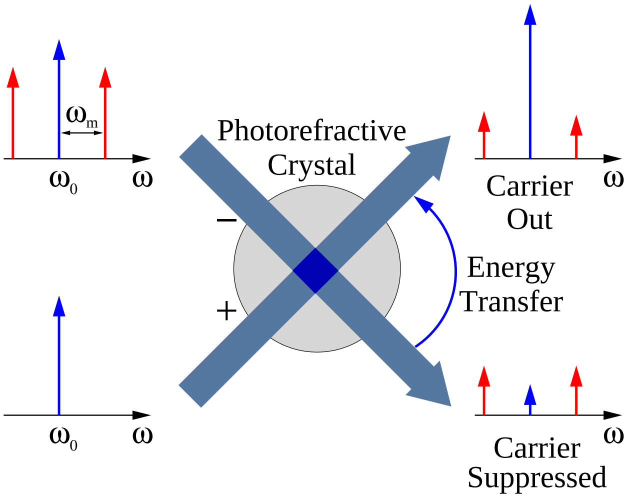

Figure 6.11: Schematic diagram of two-beam coupling carrier suppression. The input to the minus port is a modulated laser beam while the input to the plus port is an unmodulated beam from the same laser. Nonlinear coupling between the beams causes the energy in the carrier at the minus port to be transferred to the plus port at the output.

port of the photorefractive crystal. For modulation strengths less than unity, about 3 dB of signal power is lost from the signal-bearing beam. There is additional loss in the photorefractive crystal itself, which varies among crystals, and is in this case about 1.5 dB. The principal block diagram of the carrier suppression subsystem is shown in Figure 6.12. The part of the system inside of the dashed line border is a a heterodyne measurement system used to quantify suppression performance.

The input laser beam is split by a polarizing beamsplitter/half-waveplate combination to provide an adjustable power ratio. One of the beams enters the EOM, then continues to the photorefractive barium-titanate crystal (BaTiO3.) A small fraction of the other beam is used for measurements, as described below. The larger fraction interacts with the modulated beam for carrier suppression in the photorefractive medium. The optical powers at the input face of the crystal are adjusted to be approximately equal. A second half-waveplate is used to rotate the polarization of the unmodulated beam to that required for two-beam coupling. The performance of the carrier suppression system is determined using a heterodyne technique. The measurement beam is frequency shifted by 80 MHz from the carrier by an acoustooptic modulator. The measurement beam and the carrier-suppressed beam are then combined with a 50/50 beamsplitter, detected by a broadband detector, and the spectrum is measured using an RF spectrum analyzer. The heterodyne signal allows determination of the power of the optical carrier in the modulated beam, as well as the strength of the various sidebands. The

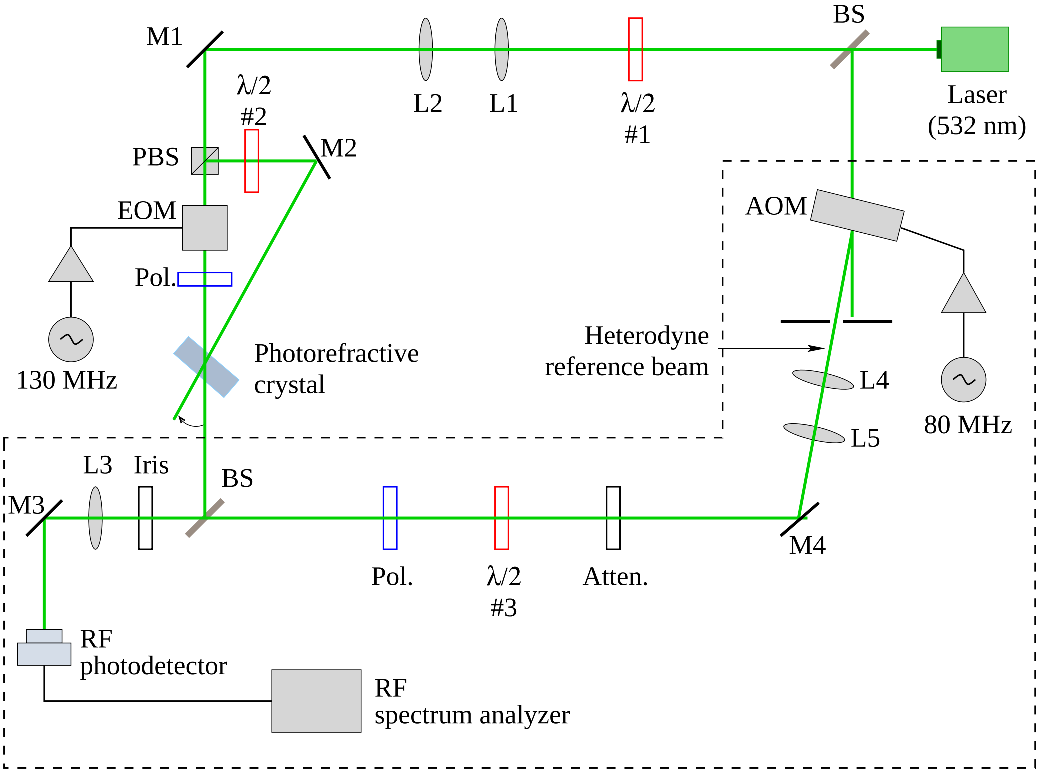

Figure 6.12: Block diagram of the optical carrier suppression system including the heterodyne measurement branch highlighted by a box. (Legend: L-lens, M-mirror, $\lambda/2$-half-waveplate, pol.-polarizer, BS-beam splitter, PBS-polarizing beam splitter, EOM-electrooptic modulator and AOM-acustooptic modulator.) All optics in the dashed box are part of the heterodyne measurement system used to quantify the carrier suppression.

electrooptic modulator is calibrated by finding the drive voltage for which the output carrier power vanishes, i.e., by finding the first zero of the zero-order Bessel function, corresponding to a modulation index $\alpha \cong 2.405$. Once calibrated, the modulator drive voltage is used to set the ratio of power in the sidebands to the total power of the modulated laser beam. The data in Figure 6.13 shows a typical performance for the carrier suppression as a function of modulation strength m. The right-hand minimum in the curve

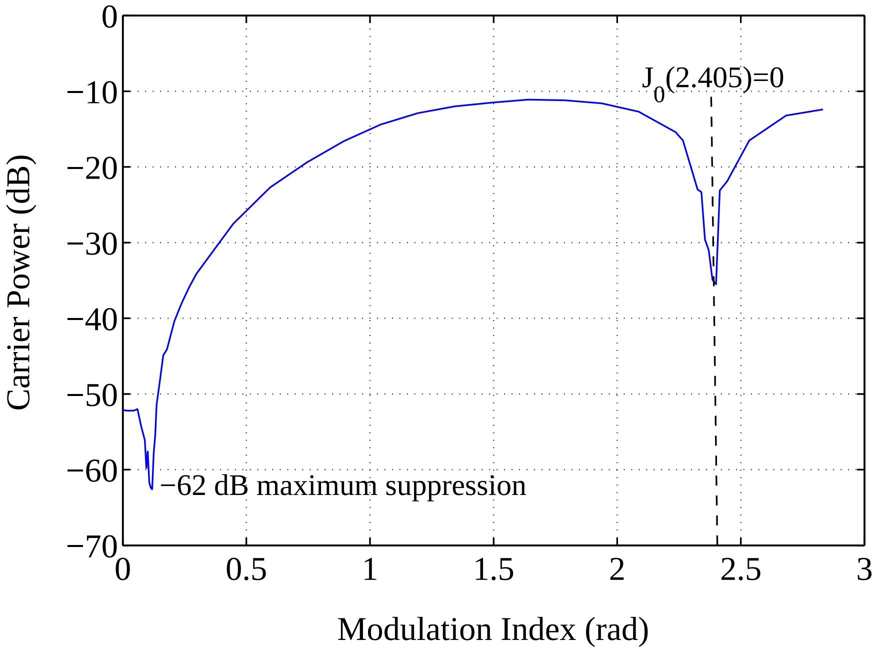

Figure 6.13: Measured performance of carrier suppression by two-beam coupling.

corresponds to the first zero of the zero-order Bessel function. The minimum of interest is the left-hand minimum, which corresponds to the theoretical perfect suppression. The graph presented in Figure 6.13 shows maximum suppression of -62 dB.

The carrier suppression subsystem is miniaturized and improved through several phases. In the final version, which is used in the system as much as -73 dB of suppression is observed. Although this value is more than sufficient to meet the current needs of the system it is important to note that this technique allows for perfect carrier suppression and the experimental results are only measurement limited. The measured limit arises from a combination of detector noise and carrier feedthrough in the acoustooptic modulator.

6.4.3 Auto-Tuning Filter

The modulated carrier-suppressed optical beams are coupled into an adaptive optical circuit, referred to as an *auto-tuning filter*, that separates the two principal components of the signal input space [62, 63]. This stage is fundamentally an optical oscillator where gain is supplied by photorefractive two-beam coupling. The auto-tuning filter has one input and two outputs. The input consists of multiple IF signals imposed on an optical beam as described above. One output provides the strongest IF principal signal component and the other provides all the other components. The output of interest depends on the application: for example, a weak signal and a strong interferer causes the desired signal to appear at output 2. For the case of a signal barely above noise level, output 1 delivers the signal with suppressed noise.

Chapter 7

Conclusions and Future Work

7.1 Thesis Summary

This thesis addresses the topic of a low-cost multibeam antenna array architecture with added functionality. Designs with theoretical and experimental characterization of two constrained lens arrays with polarization and angle diversity for wide scan range are presented.

The first design is a 45-element bifocal cylindrical lens array. It operates in X-band with a central frequency at 10 GHz and the scan range from -45° to $+45^\circ$. Extensive research was done in the selection of an antenna element for the lens array. A good candidate needs to be compact with good polarization characteristics and easy to manufacture. The antenna element used in the array is a dual-polarized square patch antenna. Measured isolation between the two ports at resonance is better than 35 dB and the cross-pol is about

30 dB. The antenna is matched to 50 Ω to make it compatible with the MMIC amplifiers if an active array design is of interest. A rectangular lattice with 15 rows and 3 columns is used for the lens array. The lens is manufactured using a milling machine and measured in an anechoic chamber. The gain variation in the entire scan range is about 1.5 dB. The half-power beamwidth increases from 6.5° at boresite to 11° at ± 45° off axis. The side-lobe level varies from -15 dB to -9 dB in the same scan range. The radiation patterns are calculated and a good match with the measurements is observed. The *thru* measurement is often used to characterize losses in CLAs [64, 33, 65]. A set of *thru* measurements with and without the aperture in the absorber are performed. The results obtained are better than those measured in the group so far. The received power is in some cases greater than the level measured in the *thru* measurement calibration. In order to explain the results, a physical meaning of this measurement is provided. The loss mechanisms in the system are identified and calculated. The power density at the focal surface is also calculated.

Analysis performed on the first lens array gives valuable guidelines which can be used in the future CLA designs. Those guidelines are already applied in the second design, which is a 165-element symmetrical lens array. That lens had to be dual-polarized, lightweight, low-cost and with wide scan range. Besides these specifications which were already achieved in the first design, some additional features and improvements were of interest. The lens had to be designed for three-dimensional scanning, with improved beam uniformity, wider bandwidth, and lower spill over loss. The unit cell is a dual-polarized stacked patch antenna. That configuration allows for a wider bandwidth keeping the same surface area required for a single-layer patch. In this case about 9 % fractional bandwidth with 10.3 GHz central frequency is achieved. The isolation between the ports is -24 dB, the cross-polarized signal is more than 20 dB below the co-polarized and the back radiation is below -20 dB. The asymmetry observed in the radiation pattern of the antenna element used in the first lens array does not appear here. The *thru* measurement gives 8.6 dB of the relative power. Such a good result is due to an increase in the directivity of more than 5 dB, and 7 dB decrease in the spill-over loss. The maximum gain varies by only 1 dB in the E-plane and not more than 2 dB in the H-plane. The half-power beamwidth of 7° for a beam on boresite changes less than 1.5 % in both principal planes over the 60° scan range. The side-lobe levels range from -22 dB for the beam at 0° to -17 dB for a beam steered to ± 30°. All the specifications are therefore satisfied.

Lens arrays are compared with other multibeam systems: dielectric lenses and phased arrays. Applications in which large arrays with hundreds of elements are required as well as wide scan range can benefit from the CLA design. Unlike the losses in the corporate combining networks used in the phased arrays, which increase with increase in the number of elements, losses in the spatial combining networks scale favorably with the size of the lens. The number of beams and their orientation can be reconfigured in the CLAs. They are easy to manufacture and therefore low-cost systems. All of these features make them attractive for a wide range of applications. The CLAs are also compared with the Gaussian systems showing some similarities in the case of large lens arrays.

A significant part of the research was dedicated to the applications of the CLAs in various communication systems. The CLA is first used in a controlled multipath environment. Significant reduction in fading is observed. Due to the angle diversity, multipath signals can be separated from the direct signal. A full duplex Ka-band lens with amplitude controlled small-angle scanning is used for fixed-formation satellites. Scanning of $\pm 2.5^\circ$ around the fixed beam position was of interest. A simple two-element array with controlled amplitudes is used as a feed. The steering of the beam is measured and the results are compared with the simulations. Finally the CLA is used as an RF front end of an adaptive optical processor. That research was sponsored by the OSEP (Optical Science and Engineering Program), which is a part of the NSF-IGERT Program (National Science Foundation - Integrative Graduate Education and Research Traineeship).

7.2 Original Contributions

The original contributions of this thesis are both theoretical and experimental. Theoretical contributions are:

- Application of a systematic analysis of CLAs including both amplitude taper and phase errors.

- Considerations of feed antenna design for optimal lens illumination.
- Development of a physical insight into the appropriate measurement procedure for specially fed arrays, which enables a determination of performance bounds.
- A comparison of discrete lenses with continuous dielectric lenses and standard phased arrays.
- A new method for continuous small-angle scanning using amplitude control, which results from the Fourier transform property of CLAs.

On the design and experimental implementation side, the following contributions can be singled out:

- Excellent wide scan-angle performance in one plane (with cylindrical lens) and in 3-D (with approximately spherical CLA).
- Multibeam implementation with low beam cross-talk.
- Dual polarized array with good cross-pol for multiple beams.
- Design of CLA for minimal loss, validated by experiment.
- Compact, broadband, stacked-patch, dual-polarized antenna element with 50 Ω microstrip feeds, measured 2:1 VSWR bandwidth of 9 % and a feed isolation of - 24 dB. This element was especially developed for large CLAs in order to reduce complexity and cost, by minimizing the

number of layers. Compact antenna element enables small unit cell size for antenna arrays with high aperture efficiency.

- Array design for straightforward integration with amplifiers in each element already matched to $50\,\Omega$ impedance.

An important contribution of this thesis is integration of the developed components into three types of real systems. This was one of the most challenging parts of the project, but rewarding as it proves the utility of CLAs.

7.3 Future Work

There are many possibilities for the future work in terms of applications and improvements of the CLAs. The theoretical model developed in [66, 67] can predict an increase in channel capacity when the CLA is used in a scatterer-rich environment. Verification of this theory with measurements is part of joint future work between the University of Colorado at Boulder and the University of Wisconsin-Madison, under the NSF-ITR (Information Technology Research) funded program. Amplifiers can be added to already $50\,\Omega$ matched antenna elements in an active array design. Amplitude excitation of the array aperture can be optimized for lower side-lobe levels. The concept of small angle steering can be further expanded.

The CLAs are also attractive for satellite communications where a multibeam system with continuous tracking is required. This is pursued in a new project funded by the NASA Glenn Research Center. Lower cost multibeam

SAR (Synthetic Aperture Radar) [68] and future GPS (Global Positioning System) [69] are other areas where CLAs can be applied.

Bibliography

[1] William C. Jakes, *Microwave Mobile Communications*, IEEE Press, New Jersey, 1974. 2, 99

[2] P. L. Perini and C. L. Holloway, “Angle and space diversity comparisons in different mobile radio environments,” *IEEE Transactions on Antennas and Propagation*, vol. 46, no. 6, pp. 764–775, June 1998. 2, 99

[3] W. L. Stutzman, J. H. Reed, C. B. Dietrich, B. K. Kim, and D. G. Sweeney, “Recent results from smart antenna experiments - base station and handheld terminals,” *IEEE Radio and Wireless Conference Digest*, pp. 139–142, Sept. 2000. 2, 99

[4] B. S. Collins, “Polarization diversity antennas for compact base stations,” *Microwave Journal*, vol. 43, no. 1, pp. 76–88, Jan. 2000. 2, 99

[5] Carlyle J. Sletten, “Constrained lenses,” in *Reflector and Lens Antennas*, Daniel T. McGrath, Ed., chapter 6. Artech House, Boston, 1988. 3

[6] Winston E. Kock, “Metal lens antennas,” *Proceedings IRE*, vol. 34, pp. 828–836, Nov. 1946. 3

[7] John Brown, *Microwave Lenses*, Methuen’s Monographs on Physical Subjects, London, 1953. 3

[8] H. Gent, “The bootlace aerial,” *Royal Radar Establishment Journal*, pp. 47–57, Oct. 1957. 5

[9] S. S. D. Jones, H. Gent, and A. A. L. Browne, “Improvements in or relating to electromagnetic-wave lens and mirror systems,” *British Provisional Patent Specification*, , no. 25926/56, Aug. 1956. 6

[10] Robert A. York, “Quasi-optical antenna-array amplifiers,” in *Active and quasi-optical arrays for solid-state power combining*, Zoya B. Popović, Robert A. York, Emilio A. Sovero, and Jon Schoenberg, Eds., chapter 5. John Wiley & Sons, Inc., New York, 1997. 7

[11] Jon S. H. Schoenberg, Scott C. Bundy, and Zoya Popović, “Two-level power combining using a lens amplifier,” *IEEE Transactions on Microwave Theory and Techniques*, vol. 42, no. 12, pp. 2480–2485, Dec. 1994. 7

[12] J. Hubert, J. Schoenberg, and Z. Popović, “High-power hybrid quasi-optical Ka-band amplifier design,” *IEEE MTT-S International Microwave Symposium Digest*, pp. 585–588, May 1995. 7

[13] S. Ortiz, T. Ivanov, and A. Mortazawi, “A transmit-receive spatial

amplifier array," *IEEE MTT-S International Microwave Symposium Digest*, vol. 2, pp. 679–682, Jun. 1997. 7

[14] M. A. Forman, T. S. Marshall, and Z. Popović, "Two Ka-band quasi-optical amplifier arrays," *IEEE Transactions on Microwave Theory and Techniques*, June 1999. 7

[15] Stein Hollung, Amanda E. Cox, and Zoya Popović, "A quasi-optical bi-directional lens amplifier," *IEEE Transactions on Microwave Theory and Techniques*, vol. 47, pp. 2352–2357, Dec. 1997. 7

[16] Zoya Popović and Amir Mortazawi, "Quasi-optical transmit/receive front ends," *IEEE Transactions on Microwave Theory and Techniques*, vol. 46, no. 11, pp. 1964–1975, Nov. 1998. 7

[17] J. Vian and Z. Popović, "A transmit/receive active antenna with fast low-power optical switching," *IEEE Transactions on Microwave Theory and Techniques*, vol. 2, pp. 847–852, June 2000. 7

[18] W. Rotman and R. Turner, "Wide angle microwave lens for line source applications," *IEEE Trans. Ant. and Prop.*, vol. AP-11, pp. 623–632, Nov. 1963. 7

[19] Jaganmohan B. L. Rao, "Multifocal three-dimensional bootlace lenses," *IEEE Transactions on Antennas and Propagation*, vol. AP-30, no. 6, pp. 1050–1056, Nov. 1982. 7

[20] Carey M. Rappaport and Amir I. Zaghloul, "Optimized three-dimensional lenses for wide-angle scanning," *IEEE Transactions on*

Antennas and Propagation, vol. AP-33, no. 11, pp. 1227–1236, Nov. 1985. 7

[21] S. Cornbleet, *Microwave and geometrical optics*, chapter 3, Academic Press, New York, 1994. 7

[22] D. T. McGrath, “Planar three-dimensional constrained lenses,” *IEEE Trans. Ant. and Prop.*, vol. 34, pp. 46–50, Jan. 1986. 9, 11

[23] D. T. McGrath, “Slot-coupled microstrip constrained lens,” *Proceedings of the Antenna Applications Symposium*, Sept. 1987. 9

[24] D. T. McGrath, P. M. Proudfood, and M. A. Mehalic, “The microstrip constrained lens,” *Microwave Journal*, pp. 24–37, Jan. 1995. 9

[25] W. L. Stutzman and G. A. Thiele, *Antenna Theory and Design*, John Wiley & Sons, Inc., New York, NY, 1998. 14

[26] Darko Popović and Zoya Popović, “Multibeam antennas with polarization and angle diversity,” *IEEE Transactions on Antennas and Propagation*, vol. 50, no. 5, pp. 651–657, May 2002. 16

[27] W. L. Stutzman and G. A. Thiele, *Antenna Theory and Design*, pp. 210–218, John Wiley & Sons, Inc., New York, NY, 1998. 17

[28] Brian Montrose, Darko Popović, Branko Popović, and Zoya Popović,

"Dual-polarization star microstrip antenna," *European Microwave Conference*, 2001. 18

[29] B. Notaroš, B. Popović, J. P. Weem, R. Brown, and Z. Popović, "Efficient large-domain MoM solutions to electrically large practical EM problems," *IEEE Transactions on Microwave Theory and Techniques*, vol. 49, no. 1, pp. 151–159, Jan. 2001. 18

[30] D. M. Pozar, "Rigorous closed-form expressions for the surface wave loss of printed antennas," *Electronics Letters*, vol. 26, no. 13, pp. 954–956, June 1990. 20, 21

[31] Zeland Software Inc., 39120 Argonaut WY STE 499, Fremont, CA 94538 USA, *IE3D Version 7.01.* 27

[32] James E. Vian, *An Optically-Switched Transmit/Receive Lens Array for Beam-Space Adaptive Communication Systems*, Ph.D. thesis, Univ. of Colorado, Boulder, CO, 2000. 52

[33] Stein Hollung, *Quasi-Optical Transmit/Receive Lens Amplifier Arrays*, Ph.D. thesis, Univ. of Colorado, Boulder, CO, 1998. 52, 110, 119

[34] Ramesh Garg, Prakash Bhartia, Inder Bahl, and Apisak Ittipiboon, "Broadbanding of microstrip antennas," in *Microstrip Antenna Design Handbook*, chapter 9. Artech House, Boston, 2001. 56

[35] David M. Pozar and Daniel H. Schaubert, "Techniques for improving element bandwidth," in *Microstrip Antennas*, chapter 4. IEEE Press, New York, 1995. 56

[36] Jean-Francois Zurcher and Fred E. Gardiol, *Broadband Patch Antennas*, Artech House, Boston, 1995. 56

[37] G. Dubost, *Flat Radiating Dipoles and their Application to Arrays*, John Wiley & Sons, Inc., New York, 1981. 56

[38] C. K. Aanandan and K. G. Nair, “Compact bradband microstrip antenna,” *Electronics Letters*, vol. 22, pp. 1064–1065, 1986. 56, 57

[39] G Kumar and K. C. Gupta, “Directly coupled multiple resonator wideband microstrip antennas,” *IEEE Transactions on Antennas and Propagation*, vol. AP-33, pp. 588–593, 1985. 56

[40] G Kumar and K. C. Gupta, “Nonradiating edges and four edges gap coupled multiple resonator broadband microstrip antennas,” *IEEE Transactions on Antennas and Propagation*, vol. AP-33, pp. 173–178, 1985. 56

[41] G Kumar and K. C. Gupta, “Broadband microstrip antennas using additional resonators gap coupled to the radiating edges,” *IEEE Transactions on Antennas and Propagation*, vol. AP-32, pp. 1375–1379, 1984. 57

[42] S. D. Targonski, R. B. Waterhouse, and D. M. Pozar, “Design of wideband aperture-stacked patch microstrip antenna,” *IEEE Transactions on Antennas and Propagation*, vol. AP-46, pp. 1245–1251, 1998. 57, 58

[43] F. Klefenz and A. Dreher, “Aperture-coupled stacked microstrip antenna with dual polarization and low back-radiation for X-band SAR

applications," *IEEE Radio and Wireless Conference Digest*, pp. 179–182, Sept. 2000. 57

[44] R. Q. Lee, K. F. Lee, and J. Bobinchak, "Characteristics of a two-layer electromagnetically coupled rectangular patch antenna," *Electronics Letters*, vol. 23, no. 20, pp. 1070–1072, Sept. 1987. 59

[45] M. Edimo, P. Rigolant, and C. Terret, "Wideband dual polarized aperture-coupled stacked patch antenna array operating in C-band," *Electronics Letters*, vol. 30, pp. 1196–1198, 1994. 59

[46] E. A. Bahaa and Malvin Carl Teich, *Fundamentals of Photonics*, chapter 3, John Wiley & Sons, Inc., New York, 1991. 83

[47] Paul F. Goldsmith, *Quasioptical Systems*, IEEE Press, New York, 1998. 83, 89

[48] S. Nemoto, "Nonparaxial Gaussian beams," *Appl. Opt.*, vol. 29, pp. 1940–1946, May 1990. 89

[49] J. C. Rautio, "An investigation of microstrip conductor loss," *IEEE Microwave Magazine*, pp. 60–67, Dec. 2000. 96

[50] S. Römisch, N. Shino, D. Popović, P. Bell, and Z. Popović, "Multibeam planar discrete millimeter-wave lens for fixed-formation satellites," *URSI General Assembly Digest*, Aug. 2002. 106

[51] Dana Z. Anderson, Valeria Damião, Edeline Fotheringham, Darko Popović, Stefania Römisch, Amy Sullivan, and Zoya Popović, "Optically smart active antenna arrays," *IEEE Transactions on Antennas and Propagation*, vol. 50, no. 5, pp. 607–617, May 2002. 108

[52] P. Comon, "Independent component analysis. A new concept?," *Signal Processing*, vol. 36, pp. 287–314, Apr. 1994. 110

[53] Paul C. Smith, *Personal Communication*, University of Colorado, Boulder, CO USA. 110

[54] R. D. Esman and K. J. Williams, "Wideband efficiency improvement of fiber optic systems by carrier subtraction," *IEEE Photonics Technology Letters*, vol. 7, no. 2, pp. 218–220, Feb. 1995. 112

[55] A. C. Lindsay, "An analysis of coherent carrier suppression techniques for photonic microwave links," *IEEE Transactions on Microwave Theory and Techniques*, vol. 47, no. 7, pp. 1194–1200, 1999. 112

[56] A. Loayssa, D Benito, and M. J. Garde, "Optical carrier-suppression technique with a Brillouin erbium fiber laser," *Optics Letters*, vol. 25, no. 4, pp. 197–199, Feb. 2000. 112

[57] S. Tonda-Goldstein, D. Dolfi, J. P. Huignard, G. Charlet, and J. Chazelas, "Stimulated Brillouin scattering for microwave signal modulation depth increase in optical links," *Electronics Letters*, vol. 36, no. 11, pp. 944–946, May 2000. 112

[58] P. Yeh, *Introduction to Photorefractive Nonlinear Optics*, chapter 3, John Wiley & Sons, Inc., New York, 1993. 113

[59] D. Z. Anderson and J. Feinberg, "Optical novelty filters," *IEEE Journal of Quantum Electronics*, vol. 25, pp. 635–647, Mar. 1989. 113

[60] Valeria B. Damião, *Developments in photorefractive two-beam coupling systems*, Ph.D. thesis, Univ. of Colorado, Boulder, CO, 2000. 113

[61] Dana Z. Anderson, Valeria Damião, Darko Popović, Zoya Popović, Stefania Römisch, and Amy Sullivan, "-70 dB optical carrier suppression by two-beam coupling in photorefractive media," *Applied Physics*, pp. 743–748, 2001. 113

[62] M. Saffman, C. Benkert, and D. Z. Anderson, "Self-organizing photorefractive frequency demultiplexer," *Opt. Lett.*, vol. 16, no. 24, pp. 1993–1995, Dec. 1991. 117

[63] Edeline Fotheringham and Dana Z. Anderson, "A miniature photorefractive circuit for principal component extraction," *submitted to Applied Optics*, 2002. 117

[64] Jon S. H. Schoenberg, *Quasi-Optical Constrained Lens Amplifiers*, Ph.D. thesis, Univ. of Colorado, Boulder, CO, 1995. 119

[65] Michael Forman, *Active Antenna Arrays for Power Combining and Communications*, Ph.D. thesis, Univ. of Colorado, Boulder, CO, 2001. 119

[66] A. M. Sayeed, "On modeling multi-antenna multipath channels," *38th Allerton Conference on Communication, Control and Computing*, Oct. 2000. 123

[67] T. A. Kadous and A. M. Sayeed, "Decentralized multiuser detection for time-varying multipath channels," *IEEE Transactions on Communications*, vol. 48, no. 11, pp. 1840–1852, Nov. 2000. 123

[68] Gary Rait, *Quasi-Optical Discrete Lens Arrays for Synthetic Aperture Radar*, Ph.D. thesis, Univ. of Colorado, Boulder, CO, 2002. 124

[69] Marc A. Weiss, *Personal Communication*, National Institute of Standards and Technology, Boulder, CO USA. 124